ივანე ჯავახიშვილის სახელობის თბილისის სახელმწიფო უნივერსიტეტი

ზუსტ და საბუნებისმეტყველო მეცნიერებათა ფაკულტეტი

სადოქტორო პროგრამა: ფიზიკა

გიორგი ხაზარაძე

მაგნიტური და მაგნიტოელექტრული თვისებების შესწავლა Y-ტიპის ჰექსაფერიტის მონოკრისტალებში

ფიზიკის დოქტორის აკადემიური ხარისხის მოსაპოვებლად წარმოდგენილი დისერტაცია

სამეცნიერო ხელმძღვანელი: ალექსანდრე შენგელაია

ფიზიკა-მათემატიკის

მეცნიერებათა დოქტორი, პროფესორი

თბილისი

2020 წელი

Ivane Javakhishvili Tbilisi State University
Faculty of Exact and Natural Sciences

Doctoral Program: Physics

Giorgi Khazaradze

Magnetic and Magnetoelectric Properties of Y-type Hexaferrite Single Crystals

The thesis work is performed to obtain a PhD academic degree in Physics

Scientific Supervisor: Alexander Shengelaya
Doctor of Phys-Math Sciences, Professor

Tbilisi
2020 Year

აბსტრაქტი

თანამედროვე ტექნოლოგიებში ფართოდ გამოიყენება ელექტრული და მაგნიტური თვისებების მქონე ნივთიერებები. მაგალითად, ფეროელექტრული თვისებების მქონე ნივთიერებები გამოიყენება კომპიუტერის ოპერატიული მეხსიერების მოწყობილობებში, ხოლო ფერომაგნიტური ნივთიერებები კომპიუტერის მყარი დისკის შესაქმნელად. თანდათანობით ძლიერდება ინტერესი ელექტრული და მაგნიტური თვისებების კომბინირების, მრავალფუნქციურ მოწყობილობებში. ისეთ ნივთიერებებს, რომლებსაც ერთდროულად როგორც ფეროელექტრული, ასევე ფერომაგნიტური მოწესრიგებები გააჩნიათ, მულტიფეროიკებს ეწოდებათ. არსებობს ისეთი მულტიფეროიკული ნივთიერებები რომლებშიც ფეროელექტრულ და ფერომაგნიტურ მოწესრიგებებს შორის არსებობს კავშირი. ასეთ კავშირს მაგნიტოელექტრულ კავშირს (მეკ) უწოდებენ. ნივთიერებებში მაგნიტოელექტრული ეფექტის   არსებობის შემთხვევაში, მაგნიტური ველით შესაძლებელია ნივთიერების ელექტრული თვისებების შეცვლა და პირიქით, ელექტრული ველით მაგნიტურის. სამწუხაროდ, ასეთი ტიპის ნივთიერებები ძალიან იშვიათია, რადგან ფეროელექტრობის კლასიკური მექანიზმი შეუსაბამოა ფერომაგნიტურ მოწესრიგებასთან. ამიტომ, ისეთი ნივთიერებების მოძებნა, რომლებსაც გააჩნიათ დიდი მაგნიტური მომენტი და ამავდროულად ძლიერი მეკ_ი, დიდი გამოწვევაა თანამედროვე კონდენსირებული გარემოს ფიზიკაში. ასევე, ამოცანას ართულებს ის ფაქტიც, რომ პრაქტიკული გამოყენებისთვის საჭიროა ისეთი მულტიფეროიკული ნივთიერებები, რომლებსაც მეკ_ი   ოთახის ტემპერატურაზე გააჩნიათ.

ახლახანს, აღმოაჩინეს რომ ჰექსაფერიტებს აქვთ პოტენციალი იყვნენ მაღალ ტემპერატურული მულტიფეროიკები. ამ ტიპის ნივთიერებებში მაგნიტური ველის საშუალებით შესაძლებელია ელექტრული მოწესრიგების ინდუცირება, რასაც თან ახლავს მეკ-ის გაჩენა. ამ თეზისში წარმოდგენილია Y-ტიპის $Ba_{0.6}Sr_{1.4}Zn_2Fe_{12}O_{22}$ ჰექსაფერიტის მონოკრისტალის მაგნიტური და მაგნიტოელექტრული თვისებების შესწავლის ექსპერიმენტული შედეგები.

Y-ტიპის $Ba_{0.6}Sr_{1.4}Zn_2Fe_{12}O_{22}$ ჰექსაფერიტის მონოკრისტალური ნიმუშები მოვამზადეთ ნაკადით ზრდის მეთოდის საშუალებით. მიღებული ნიმუშები

შევისწავლეთ რენტგენის სხივების მონოკრისტალზე გაბნევის მეთოდით (Single-Crystal X-ray Diffraction) და მიღებული შედეგების გაანალიზებით, დავადგინეთ კრისტალის მესრის პარამეტრები. მაგნიტური და მაგნიტოელექტრული თვისებები შევისწავლეთ ვიბრაციული მაგნიტომეტრის და ფერომაგნიტური რეზონსის საშუალებით. აღმოჩნდა, რომ 400 კელვინი ტემპერატურის ქვემოთ ნივთიერება ფერიმაგნიტურადაა მოწესრიგებული, ხოლო 331 კელვინ ტემპერატურაზე ნივთიერება გადადის ფერიმაგნიტური მოწესრიგებიდან ხრახნისებრ სპინურ მოწესრიგებაში. მაგნიტურმა გაზომვებმა აჩვენა, რომ მეტამაგნიტური გადასვლების გამო, მაგნტური ველის ზრდასთან ერთად დამაგნიტების მრუდი იცვლება საფეხურისებრად. ასევე, აღმოჩნდა რომ ნიმუშს მცირე კოერციტიული ველი გააჩნია, რაც მიანიშნებს რომ ნივთიერება მაგნიტურად რბილია. Y-ტიპის $Ba_{0.6}Sr_{1.4}Zn_2Fe_{12}O_{22}$ ჰექსაფერიტის მონოკრისტალურ ნიმუშში ფერომაგნიტური რეზონანსული ველის კუთხეზე დამოკიდებულება შევისწავლეთ ფერომაგნიტური რეზონანსის საშუალებით და გამოვთვალეთ ანიზოტროპიის ველი. მეკ_ის შესასწავლად გამოვიყენეთ ახალი მეთოდი, რომელიც დაფუძნებულია სტანდარტულ ელექტრონულ პარამაგნიტური რეზონანსის ტექნიკაზე (დამატებული აქვს ელექტრული ველით მოდულაციის ფუნქცია). ამ მეთოდის ძირითადი იდეა მდგომარეობს შემდეგში: თუ ნიმუშს გააჩნია მეკ_ი, ელექტრული ველით მოდულაცია ნიმუშში გამოიწვევს დამაგნიტების მოდულაციას და შესაბამისად მაგნიტური ველის ინდუქციის მოდულაციას. ამ მეთოდის გამოყენებით, ჩვენ პირველად, ვაჩვენეთ რომ Y-ტიპის $Ba_{0.6}Sr_{1.4}Zn_2Fe_{12}O_{22}$ ჰექსაფერიტის მონოკრისტალურ ნიმუშს აქვს მეკ_ი ოთახის ტემპერატურაზე. ეს შედეგი მიუთითებს, რომ Y-ტიპის $Ba_{0.6}Sr_{1.4}Zn_2Fe_{12}O_{22}$ ჰექსაფერიტის მონოკრისტალურ ნიმუშში „Intermediate-II" ფაზა, ისევე როგორც „Intermediate-III" ფაზა არის ფეროელექტრული. და თუ ეს ასეა, „Intermediate-II" ფაზში მაგნიტური სისტემა უნდა იყოს ქირალური, და სპინური მოწესრიგება განივი კონუსური. ამ დაშვების შესამოწმებლად გამოვიყენეთ ნეიტრონების გაბნევის მეთოდი Y-ტიპის $Ba_{0.6}Sr_{1.4}Zn_2Fe_{12}O_{22}$ ჰექსაფერიტის მონოკრისტალურ შენაერთში, „Intermediate-II" და „Intermediate-III" ფაზებში.

აღმოჩნდა, რომ ორივე ფაზებში მაგნიტური სტრუქტურა ქირალურია, რაც ადასტურებს რომ „Intermediate-II" და „Intermediate-III" ფაზებში სპინური სტრუქტურა განივი კონუსურია.

მიღებული შედეგები აჩვენებს, რომ ოთახის ტემპერატურაზე Y-ტიპის $Ba_{0.6}Sr_{1.4}Zn_2Fe_{12}O_{22}$ ჰექსაფერიტს აქვს მცი_ი და დიდი დამაგნიტება. ეს ორი ფაქტორი ძალიან მნიშვნელოვანია მაგნიტოელექტრული მოწყობილობების შესაქმნელად.

Abstract

Functional electronic and magnetic materials form an important part of modern technology. For example, ferroelectrics materials are widely used as tunable capacitors and form the basis of ferroelectric random access memory (Fe-RAM) for computers. On the other hand, the materials most widely used for recording and storing data, such as in the hard drive, are ferromagnetic. There is an increased interest in the combination of electronic and magnetic properties in a multifunctional device. Materials in which ferroelectric and magnetic orders coexist are known as multiferroic materials. Recently, multiferroic materials have attracted unprecedented attention because such materials exhibit so-called magnetoelectric (ME) coupling. The ME coupling is of high technological relevance, since it implies that electrical properties are affected by a magnetic field or, conversely, that magnetic properties can be varied by an electric field. Therefore, the ME effect, which is the cross-correlation between electricity and magnetism, is one of the central subjects in contemporary condensed-matter science. Finding multiferroic materials with both high magnetic moment and strong ME coupling is a big challenge, however, because the traditional mechanism of ferroelectricity is incompatible with ferromagnetism. Then, the problem is how to design the multiferroic material and how to enhance its ME coupling. Moreover, for practical application of this technology, coexistence of long range magnetic and electric orders at room temperature is required.

Recently, iron oxide based materials called hexaferrites attracted attention due to their potential as high-temperature multiferroics. In these materials a magnetic field driven ferroelectricity provides non-conventional mechanism of cross coupling between magnetism and ferroelectricity with resulting ME coupling. This thesis presents experimental study of magnetic and magnetoelectric properties of Y-type $Ba_{0.6}Sr_{1.4}Zn_2Fe_{12}O_{22}$ hexaferrite single crystals.

We prepared single crystals of Y-type $Ba_{0.6}Sr_{1.4}Zn_2Fe_{12}O_{22}$ hexaferrite by flux growth method. They were characterized by single-crystal X-ray diffraction measurements. The crystal lattice space group and lattice parameters were determined and structure refinement was performed. Macroscopic and microscopic magnetic and ME properties were studied by magnetometry and Ferromagnetic Resonance (FMR) measurements. It was shown that this

compound exhibits ferrimagnetic order below about 400 K with additional magnetic transition from collinear ferrimagnetic phase to a proper screw spin phase below 331 K. Magnetic hysteresis measurements showed stepwise behavior of initial magnetization curve due to sequential metamagnetic transitions with increasing magnetic field. The obtained small coercivity field indicates soft magnetic behaviour.

Using FMR method in Y-type $Ba_{0.6}Sr_{1.4}Zn_2Fe_{12}O_{22}$ hexaferrite we investigated angular dependence of FMR resonance field and calculated magnetic anisotropy field. In order to detect ME coupling we used recently developed novel electrically modulated magnetic resonance spectroscopy. This method is based on the standard Ferromagnetic/Electron Paramagnetic Resonance (FMR/EPR) technique combined with electric field modulation (EFM). By using this method we showed for the first time that Y-type $Ba_{0.6}Sr_{1.4}Zn_2Fe_{12}O_{22}$ hexaferrite has a significant ME coupling at room temperature. This indicates that in Y-type $Ba_{0.6}Sr_{1.4}Zn_2Fe_{12}O_{22}$ intermediate-II phase, similar to intermediate-III phase, is ferroelectric. If this is the case, intermediate-II phase should also have a transverse conical spin structure with corresponding chirality. To check this possibility, we performed neutron diffraction experiments with polarization analysis in the intermediate-II and intermediate-III phases of Y-type $Ba_{0.6}Sr_{1.4}Zn_2Fe_{12}O_{22}$ hexaferrite single crystal. It was found that the chiral magnetism exists in both of these phases, which means that in contrast to previous assumptions, intermediate-II phase also has transverse conical spin structure similar to the intermediate-III phase.

Obtained results show that Y-type $Ba_{0.6}Sr_{1.4}Zn_2Fe_{12}O_{22}$ hexaferrite has a rare combination of sizable ME coupling and large magnetization at room temperature, which is important for applications in magnetoelectric devices.

Table of Contents

Introduction

In 1960's a new type of materials with more than one ferroic order parameters were discovered. Materials in which ferroelectric and magnetic orders coexist are called multiferroics. Recently, multiferroic compounds have attracted significant attention because such they exhibit so-called magnetoelectric (ME) coupling [Fiebig, 2005; Erenstein, 2006]. The ME coupling is of high technological relevance, since it implies that electrical properties are affected by a magnetic field or, conversely, that magnetic properties can be varied by an electric field. Especially, the electric field control of magnetism is a hot topic because it has multiple potential applications in magnetic memory storage, sensorics, and spintronics [Wu, 2010; Ryan, 2013]. Therefore, the ME effect is one of the central subjects in contemporary condensed-matter science.

Finding multiferroic materials suitable for practical applications is a big challenge, however, because there are only very few known compounds which simultaneously display both electric and magnetic order at room temperature. Moreover, for ME effect both ferroic orders should be coupled. At present, of all multiferroic compounds, $BiFeO_3$ is one of the most interesting systems with antiferromagnetic order at Neel temperature T_N =650 K and a ferroelectric transition temperature at T_C =1100 K [Wang, 2003]. There were about 10000 publications devoted to $BiFeO_3$ in the past decade and it remains the leading candidate for room-temperature multiferroic single-phase devices. However, it is far from perfect: its magnetization is too small for many applications because of the antiferromagnetic order, and its dielectric loss and leakage current too large, despite efforts to dope it with various elements. Therefore the quest is to find compounds with large magnetization and sizable ME coupling at room temperature.

Recently, iron oxide based materials called hexaferrites attracted attention due to their potential as high-temperature multiferroics [Tokura, 2014]. Hexaferrites are ferrites with hexagonal structures. These are one of the oldest and the most extensively used magnetic materials which have fascinated material researchers worldwide by providing endless potential for numerous applications due to inherent flexibility in the highly anisotropic

structure [Pullar, 2012]. Depending on the chemical formula they are classified in six main types: M, Y, Z, X, U, W. Kimura et al. explored for the first time interesting ME properties of Y-type hexaferrite $Ba_{0.5}Sr_{1.5}Zn_2Fe_{12}O_{22}$ [Kimura, 2005]. The crystal structure of Y-type hexaferrite can be considered as an alternately stacked spinel (S) and tetragonal (T) blocks along the c axis. This crystal structure belongs to the space group $R\bar{3}m$, which does not allow spontaneous electric polarization. However, ME effect was demonstrated in $Ba_{0.5}Sr_{1.5}Zn_2Fe_{12}O_{22}$ by applying magnetic field H and inducing electric polarization P [Kimura, 2005].

Overview of the literature

2.1 Multiferroics

As explained in the introductory section the multiferiocs are defined as materials that exhibit more than one of the ferroic properties (Fig. 2.1). The concept of multiferroic was introduced by H. Schmid in 1994 [Schmid H, 1994]. There are three main types of ferroic orders: ferromagnetism, ferroelectricity and ferroelasticity. Ferromagnetism occurs in materials which have a spontaneous magnetization. In the ideal case, the magnetization of a ferromagnet in a magnetic field displays the usual hysteresis (blue). Ferroelectricity is a characteristic of certain materials that have a spontaneous electric polarization that is stable and with the application of externally applied electric field can be switched hysteretically (yellow).
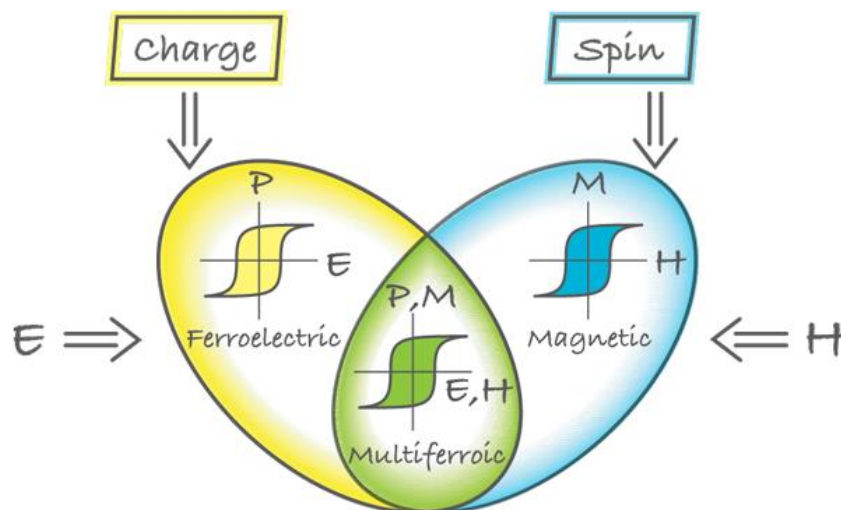

Fig. 2.1 Multiferroic materials combine magnetic and ferroelectrical properties, from [Khomskii, 2009].

Ferroelasticity is a phenomenon in which a material may exhibit a spontaneous deformation. This effect is the mechanical equivalent of ferroelectricity and ferromagnetism. With applying stress to a ferroelastic material, a phase change will occur with different crystal structure, or different orientation.

Basically, the microscopic origin of the magnetism is same in all magnets, but there are several different microscopic sources of ferroelectricity. Therefore, due to the different microscopic mechanisms of the ferroelectricity different types of multiferroics exists. With taking into account the microscopic mechanism of the ferroelectricity, multiferroic compounds are classified into two types, type-I and type-II [Khomskii, 2009]. Multiferroic materials according to this classification and different mechanisms of the ferroelectricity are listed in Table 2.1.

	Mechanisms of ferroelectricity	Materials
Type-I	Lone pair effect	$BiFeO_3$
	Charge ordering	$Pr_{0.5}Ca_{0.5}MnO_3$
	Geometrically driven ferroelectricity	$YMnO_3$
Type-II	Exchange striction	Ca_3CoMnO_6
	Antisymmetric Dzyaloshinski-Morya interaction	$RMnO_3$ (R: rare earths)
	Spin current	$RbFe(MoO_4)_2$

Table 2.1. Classification of the multiferroics and mechanisms of the ferroelectricity in multiferroics.

2.2 Type-I multiferroics

Type-I multiferioics are old and more numerous. This type contains the materials in which ferroelectricity and magnetism have the different mechanisms of the multiferroicity. The critical temperatures of the magnetic and ferroelectric transitions can be above room temperature, but unfortunately ME coupling is weak.

2.2.1 Lone pair effect

In $BiFeO_3$ compound the origin of ferroelectricity is lone pair asymmetry. Fig. 2.2.1 shows the crystal structure of multiferroic $BiFeO_3$ lone pair (Fig.2.2.1). The Bi^{3+} „A" cation has an active $6S^2$ lone pair electrons that do not participate in chemical bonds [Sang-wook, 2007; Khomskii, 2009]. The „A" cation drives a displacement of the partially filled d shell on the „B" anion site which is Fe^{3+} in the case of $BiFeO_3$ and contributes to the magnetism. The Bi^{3+} stereochemically active $6s^2$ lone pair causes the Bi 6p (empty) orbital to come closer in energy to the oxygen 2p orbitals. This process leads to a hybridization between the Bi and O orbitals and drives an off-centering of cations towards neighboring anions resulting in ferroelectricity. Because the ferroelectric and magnetic orders in this material are associated with different ions, the coupling between them is weak.
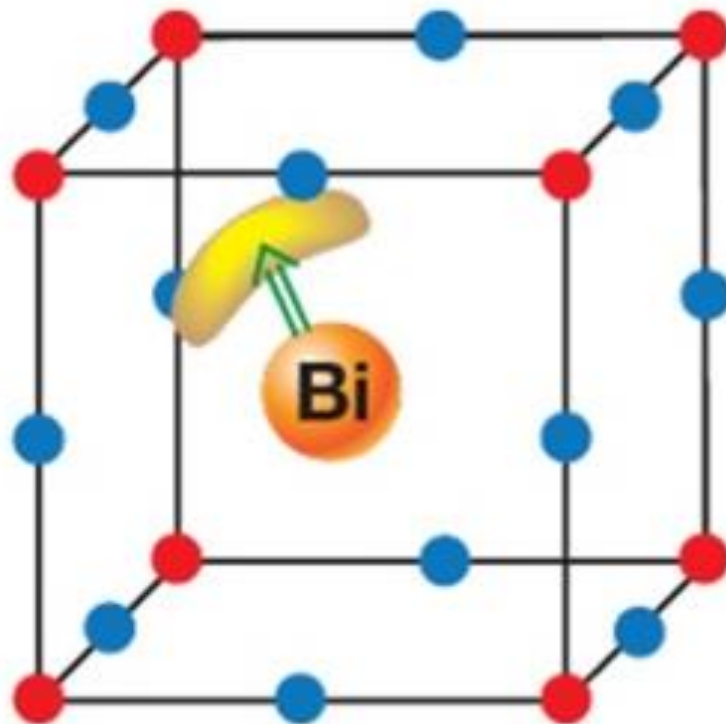

Fig. 2.2.1 the ordering of lone pairs (yellow) in $BiFeO_3$. Blue is an oxygen and red iron ions, respectively, from [Khomskii, 2009].

2.2.2 Charge ordering

Ordering of charge is another example of induction of ferroelectricity and eventually Type-I multiferroicity. This charge order is mainly observed in transition metal ions which have different valence states, e.g. $Pr_{0.5}Ca_{0.5}MnO_3$ compound [Cheong, 2007]. When charges order in a non-symmetric fashion, they induce electric polarization. The coexistence of bond-centred and site-centred charge orders in $Pr_{0.5}Ca_{0.5}MnO_3$ leads to a non-centrosymmetric charge distribution and a net electric polarization (Fig. 2.2.2).
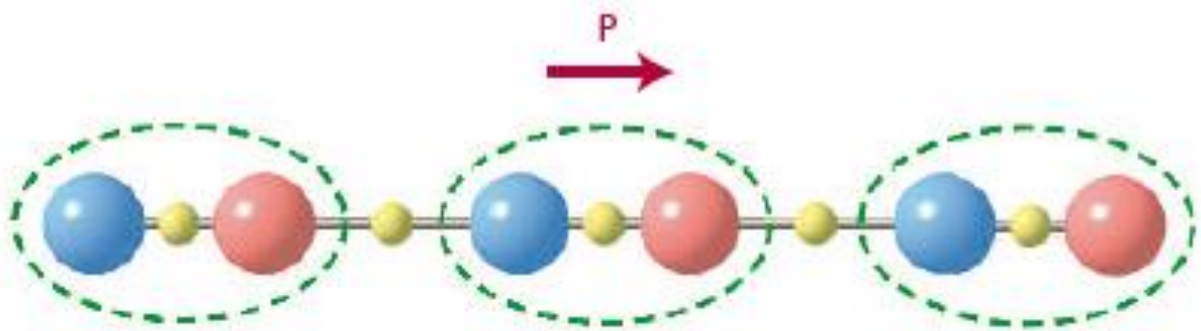

Fig. 2.2.2 Ferroelectricity in the charge ordered systems, Red/Blue spheres are cations with more/less positive charge. The site-centred and bond-centred charge orders are marked with green dashed lines. Reproduced from Ref. [Cheong, 2007].

2.2.3 Geometrically driven ferroelectricity

One more mechanism that can lead to ferroelectricity is geometrically driven ferroelectricity. This is a fundamentally different mechanism compared to lone pair and cause ferroelectricity in the hexagonal $YMnO_3$ magnetite. The hexagonal structure of $YMnO_3$ consists of non-connected layers of MnO_5 trigonal bipyramids, corner-linked by in-plane oxygen ions which form a closed packed plane separated by a layer of Y^{3+} (Fig. 2.2.3a) [Aken, 2004]. For the structure to form an energy favorable state, close packing of the MnO_5 polyhedra between the the Y^{3+} layers occurs. This tilting of rigid MnO_5 influence a long range dipole-dipol interaction and there appears two „downs" dipoles per one „up" dipole and system becomes ferroelectric (Fig. 2.2.3b) [Khomskii, 2009].
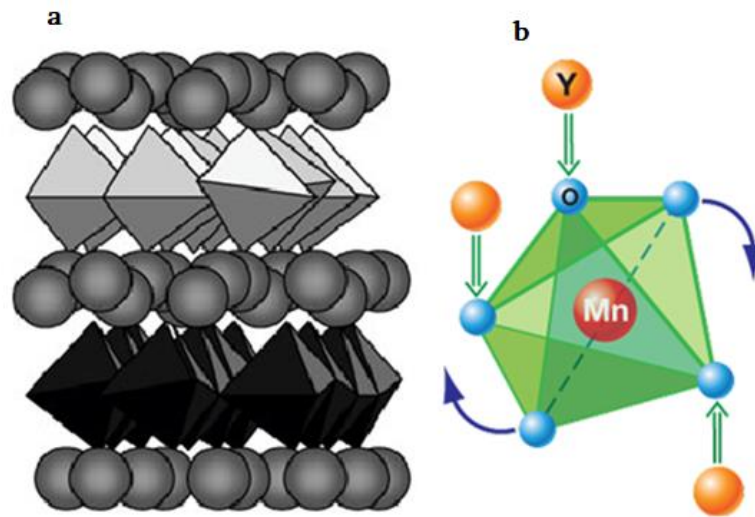
Fig. 2.2.3: a) the layered nature of YMnO$_3$ and 3.2.3 b) tilting of bipyramid in YMnO$_3$ (the green arrows are dipoles). Reproduced from Ref. [Khomskii, 2009; Van Aken, 2004].

2.3 Type-II multiferroics

Unlike type-I multiferroics, in type-II multiferrics magnetism causes ferroelectricity by breaking the crystal inversion symmetry. In this case the ordering temperatures for the two phenomena are identical.

2.3.1 Exchange striction

In the magnetic driven ferroelectrics the external magnetic field influences the configuration of the magnetic order and leads to change of ferroelectric properties. Development of the inversion-symmetry breaking magnetic order leads to the loss of the lattice inversion symmetry through exchange striction [Y. Choi, 2008], thereby leading to the development of ferroelectricity. This can be illustrated on the example of Ca$_3$CoMnO$_6$ (see Fig. 2.3.1 a). This compound consists of one-dimensional chains of alternating Co^{2+} and Mn^{4+} ions. At high temperatures, above 16 K, the distances between ions along the chain are the same and there is no polarization due to inversion symmetry of the chain. If the charges of magnetic ions alternate along the chain, this magnetic ordering breaks inversion symmetry on magnetic sites and can induce electric polarization via exchange striction.

Figure 2.3.1 b) shows two possible magnetic configurations leading to the opposite polarizations.
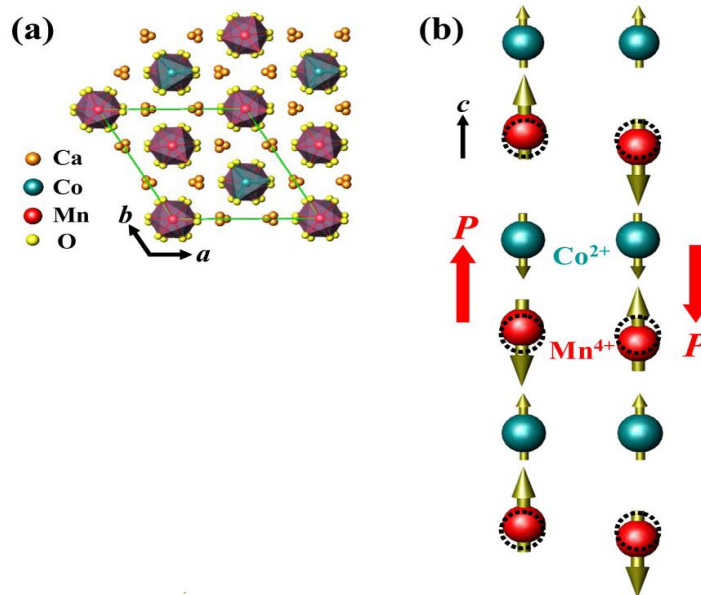

Fig. 2.3.1: a) the crystal structure of the Ca₃CoMnO₆ compound and b) magnetic chains with the up-up-down-down spin order and alternating ionic order, in which two possible orientation of electric polarization are induced through symmetric exchange striction, from [Y. Choi, 2008]. The atomic positions in the undistorted chains are shown with dashed circles.

2.3.2 Antisymmetric Dzyaloshinski-Morya interaction

One more microscopic mechanism to induce ferroelectricity is an antisymmetric Dzyaloshinskii–Moriya (DM) interaction [Dzyaloshinskii, 1960]. DM interaction is a contribution to the total magnetic exchange interaction between two neighboring magnetic S_i and S_j spins. This interaction is quantitatively represented in formula 2.3.2.

$$H_{DM} = D_{ij} \cdot [S_i \times S_j] \tag{2.3.2}$$

Where, D_{ij} is Dzyaloshinskii–Moriya vector.

This interaction is a relativistic correction to the usual superexchange interaction and its strength is proportional to the spin–orbit coupling constant, λ, and depends on the position of the oxygen ion between two magnetic transition metal ions.
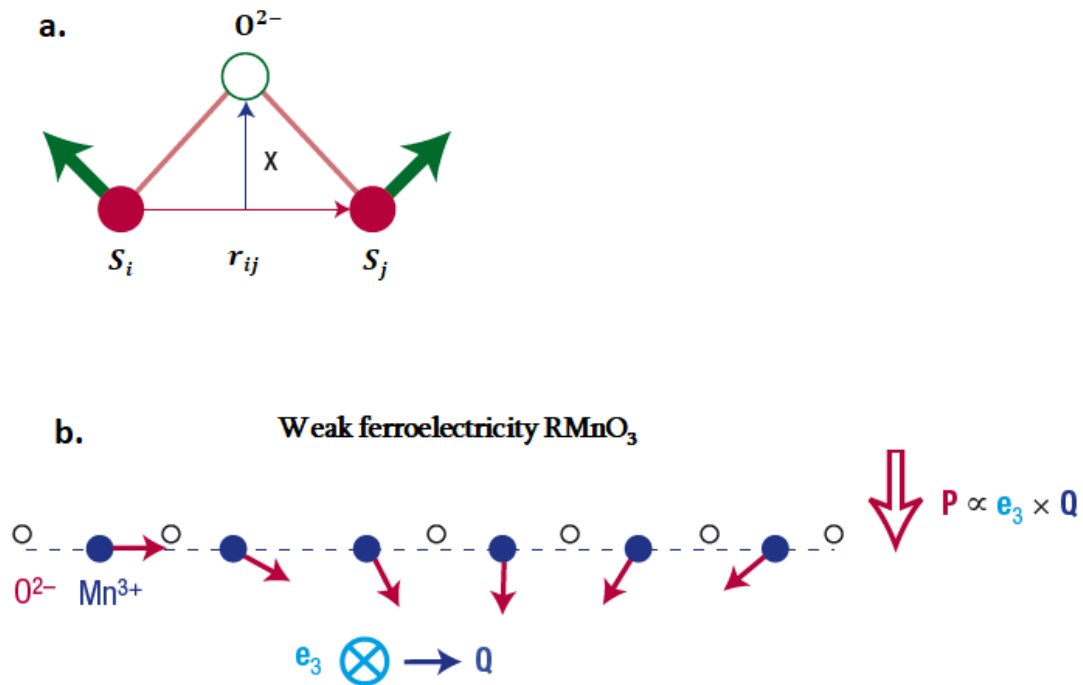
Effect of Dzyaloshinskii-Moriya interaction

Figure 2.3.2: a) Illustration of the antisymmetric Dzaloshinskii-Moriya Interaction and b) Weak ferroelectricity can be induced by the exchange striction in a magnetic spiral state, which pushes negative oxygen ions in one direction transverse to the spin chain formed by positive transition metal ions, adapted from Ref. [Cheong, 2007].

The exchange between spins of transition metal ions is usually mediated by ligands. These ligands form bonds between pairs of transition metals which bring into play the DM interaction. The DM vector $\boldsymbol{D}_{ij}$ is proportional to $x \times \boldsymbol{r}_{ij}$, where $\boldsymbol{r}_{ij}$ is a unit vector along the line connecting the magnetic ions $\boldsymbol{i}$ and $\boldsymbol{j}$, and x is the shift of the oxygen ion from the line. DM exchange energy is strongly dependent on the value of x. Based on the spin frustration within a system and the strength of the spin spiral magnetic interaction, the distance, x, denoted on figure 2.3.2 will increase or decrease. The change in x is representative of the DM interaction which pushes negative oxygen ions in one direction perpendicular to the spin

chain formed by positive ions. It is process which induces electric polarization perpendicular to the chain and is clearly demonstrated in the $RMnO_3$ system [Cheong, 2007].

2.3.3 Spin current

Spin current mechanism was proposed for the first time by Katsura and co-workers [Katsura 2004]. This mechanism can be explained using figure 2.3.3, which represents the bond between the two transition metal ions M_1, M_2 through the oxygen atom O. The $\vec{e_1}$ and $\vec{e_2}$ magnetic moments have non-collinear configuration. Between M_1 and M_2 arises the spin current $\vec{J_s}$ (denoted by the green arrow) proportional to $\vec{e_1} \times \vec{e_2}$. The direction of the electrical polarization is proportional to the vector product of the spin current $\vec{J_s}$ and unit vector $\vec{e_{ij}}$ along propagation vector direction. Therefore, the net polarization is given in the same direction as the polarization by DM mechanism. Phenomenologically, Inverse DM interaction and spin current mechanism are equivalent, with the difference that, in spin current mechanism polarization is from electronic contribution from spin current (which changes electron density) whereas in DM interaction shift of nonmagnetic atoms contributes to polarization. Therefore, spin current mechanism can also be called as inverse DM interaction.
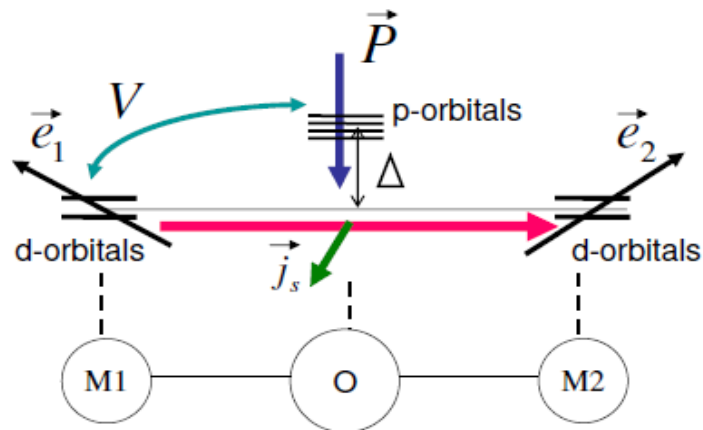

Fig. 2.3.3. The cluster model with two transition metal ions M_1, M_2 with the oxygen atom O between them, from [Katsura, 2004].

2.3.4 Magnetoelectric coupling

In 1888, Röntgen observed that a moving dielectric body placed in an electric field became magnetized, which was followed by the observation of the reverse effect: polarization generation of a moving dielectric in a magnetic field [W. C. Röntgen, 1888]. Both, however, are not the intrinsic effects of matter. In 1894, by crystal symmetry consideration, Curie predicted the possibility of an intrinsic magnetoelectric effect (ME) in some crystals [P. Curie, 1894]. Subsequently, Debye coined this kind of effect as a "ME effect" [P. Debye, 1926]. The first successful observation of the ME effect was realized in Cr_2O_3 [Astrov, D. 1960].

As was mentioned in the introduction section, multiferroic materials have ME coupling, but unfortunately not all of them. Fig. 2.3.4 shows the relationship between multiferroic and magnetoelectric materials which clearly indicates that there are very few materials which show the magnitoelectric behavior.
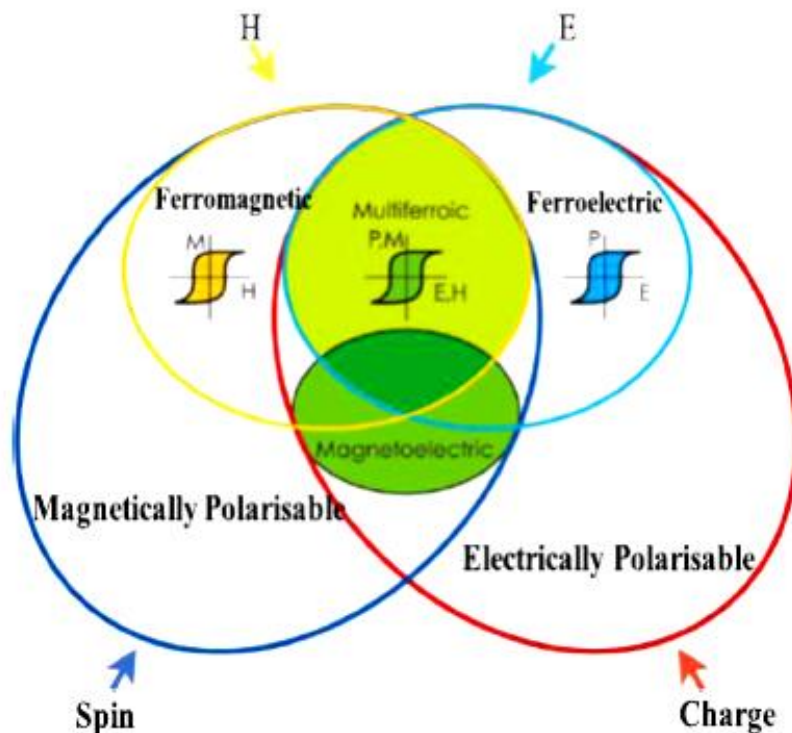

Fig. 2.3.4 The relationship between multiferroic and magnetoelectric materials. Reproduced from Ref [Khomskii, 2009] and adapted by ESRF.

Thermodynamically, the ME effect can be understood within the Landau theory, approached by the expansion of free energy for a ME system, i.e.

$$F(E,H) = F_0 - P_i^s E_i - M_i^s H_i - \frac{1}{2}\varepsilon_0\varepsilon_{ij}E_iE_j - \frac{1}{2}\mu_0\mu_{ij}H_iH_j - \alpha_{ij}E_iH_j - \frac{1}{2}\beta_{ijk}E_iH_jH_k - \frac{1}{2}\gamma_{ijk}H_iE_jE_k - .....$$

(2.3.4.1)

where F_0 is the ground state free energy. Subscripts (i, j, k) refer to the three components of a variable in spatial coordinates. E_i and H_i are components of electric field E and magnetic field H, respectively. P_i^s and M_i^s are the components of spontaneous polarization P^s and magnetization M^s, ε_0 and μ_0 are the dielectric and magnetic susceptibilities of vacuum, ε_{ij} and μ_{ij} are the second-order tensors of dielectric and magnetic susceptibilities, and most importantly, α_{ij} is the second-order tensor which accounts for the linear ME coupling. Third-order tensors β_{ijk} and γ_{ijk} in Eq. 2.3.4.1 correspond to the quadratic ME coupling (magnetization is proportional to the square of the electric field) [Muniraju, 2012]. Then the polarization and magnetization can be obtained by differentiating F with respect to E_i or H_i :

$$P_i(E,H) = -\frac{\partial F}{\partial E_i} = P_i^s + \varepsilon_0\varepsilon_{ij}E_j + \alpha_{ij}H_j + \frac{1}{2}\beta_{ijk}H_jH_k + \gamma_{ijk}H_iE_j + ..., \quad (2.3.4.2)$$

$$M_i(E,H) = -\frac{\partial F}{\partial H_i} = M_i^s + \mu_0\mu_{ij}H_j + \alpha_{ij}E_j + \beta_{ijk}H_jE_i + \frac{1}{2}\gamma_{ijk}E_jE_k + ..., \quad (2.3.4.3)$$

2.4 Hexaferrites

Hexaferrites are ferrites with hexagonal structures. These are one of the oldest and the most extensively used magnetic materials which have fascinated material researchers worldwide by providing endless potential for numerous applications due to inherent flexibility in the highly anisotropic structure [Pullar, 2012]. Depending on the chemical formula they are classified in six main types: M, Y, Z, X, U, W (Table 2.4). Schematic crystal structures of each type are shown in figure 2.4.1

Six main types of hexaferrites

Type	Chemical formula	Stacking sequence	$c\ (\mathring{A})$	Space group
M	$(Ba,Sr)\,Fe_{12}O_{19}$	RSR^*S^*	~ 23	$P6_3/mmc$
W	$(Ba,Sr)\,Me_2Fe_{16}O_{27}$	$RS_2R^*S_2^*$	~ 33	$P6_3/mmc$
Y	$(Ba,Sr)_2\,Me_2Fe_{12}O_{22}$	$TST'S'T''S''$	~ 43	$R\bar{3}m$
Z	$(Ba,Sr)_3\,Me_2Fe_{24}O_{41}$	$RSTSR^*S^*T^*S^*$	~ 43	$P6_3/mmc$
X	$(Ba,Sr)_2\,Me_2Fe_{28}O_{46}$	$(RSR^*S_2^*)_3$	~ 84	$R\bar{3}m$
U	$(Ba,Sr)_4\,Me_2Fe_{36}O_{60}$	$(RSR^*S^*TS^*)_3$	~ 113	$R\bar{3}m$

Table 2.4. classification of the hexaferrites depending on their chemical formulas and stacking sequences. The $(*)$ symbol means that the corresponding block turns 180° about the hexagonal c axis and the apostrophe means that corresponding block is rotated 120° around this axis.
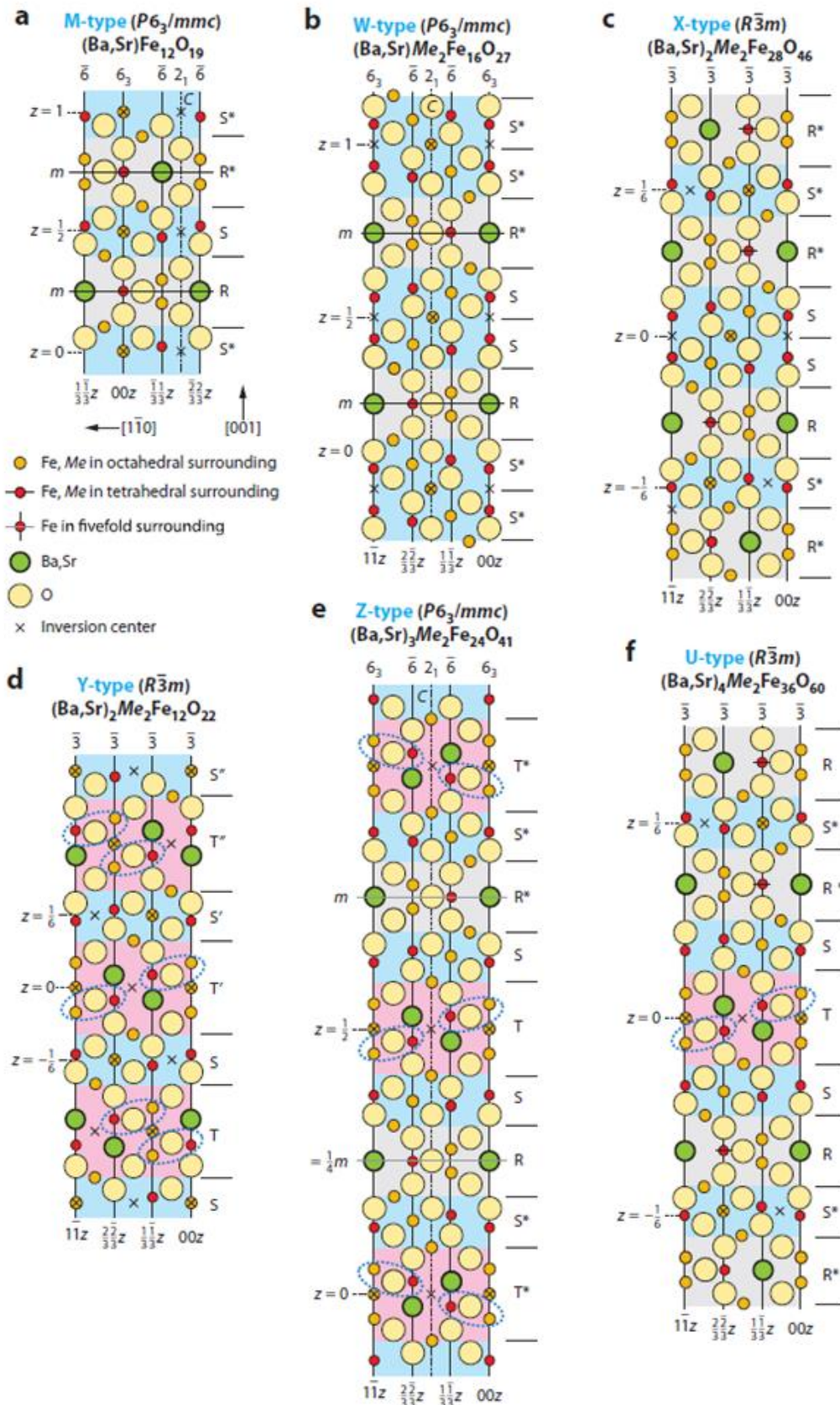
Fig. 2.4.1. Schematic view of crystal structure of hexaferrites, from [Kimura, 2012]. Dashed blue ellipsoids are (Fe,*Me*)-O-(Fe,*Me*) bond angles. „*Me*" denotes divalent metal ion.

The M-type hexafferrites are well suited for permanent magnet applications. They are used in loudspeakers, electric motors, clocks, correction magnets in cathode ray tubes, dynamos and etc. The M-type hexafferrites are also widely used for various microwave devices and modern radars. The X, U and W-type hexaferrites are good MW absorbers in the X and K bands. The Y and Z-type hexaferrites have good potential for applications in mobile communication and memory storage devices [Singh, 2016; Shen, 2017]. In fact, these classes of materials are the only materials having magnetic ordering above 100 K with spiral spin based multiferroicity. Moreover, high magnetic moments are observed in all the classes of hexaferrites. In the year 2005, a class of hexaferrite, called Y-type hexaferrite, was found to display magnetic field driven ferroelectricity below 130 K and the maximum of the field-driven polarization was near 1 Tesla [Kimura, 2008].
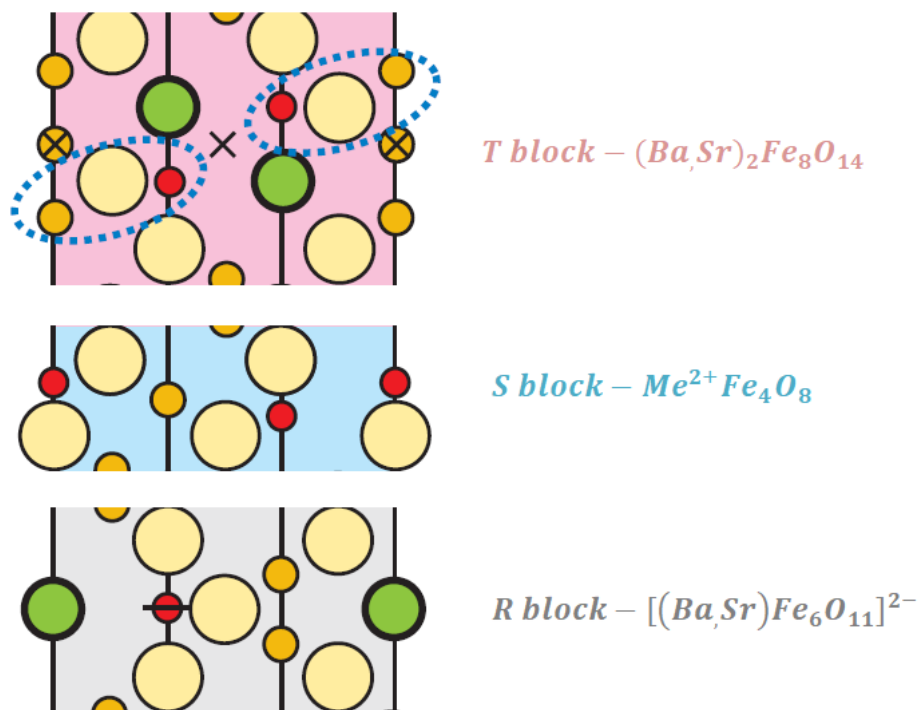

$T\ block - (Ba,Sr)_2Fe_8O_{14}$

$S\ block - Me^{2+}Fe_4O_8$

$R\ block - [(Ba,Sr)Fe_6O_{11}]^{2-}$

Fig. 2.4.2 Basic blocks of hexaferrites („*Me*" denotes divalent metal ion). Dashed blue ellipsoids are (Fe,*Me*)-O-(Fe,*Me*) bond angles. Reproduced from Ref. [Kimura, 2012].

Low field (±30 mT) ME coupling was observed in Mg- and Al-substituted Y-type hexaferrite [Chun, 2010]. Later, in Sc- and Mg- substituted M-type hexaferrite magnetic field driven ferroelectricity was found [Tokunaga Y, 2012]. In about the same time, room temperature ME coupling was demonstrated in Z-type hexaferrite compound [Kitagawa,

2010]. These hexaferrites structures can be described as stacking sequences of three basic blocks: S ($Me^{2+}Fe_4O_8$; spinel block), R [$(Ba,Sr)Fe_6O_{11}]^{2-}$, and T [$(Ba,Sr)_2Fe_8O_{14}$], see fig 2.4.2, [Kimura, 2012].

2.4.1 M-type

M-type hexaferrites have the simplest stacking structures among all six hexaferrites (fig. 2.4.1 a). This type of ferrite is made of one S and one R block, with an overlap of hexagonally and cubically packed layers and belongs to $P6_3/mmc$ space group. A ferrimagnetic M-type hexaferrites (Ba(Fe,Sc,Mg)$_{12}$O$_{19}$) are the most popular and well-studied ferrites. The measurements revealed that, in Sc-doped M-type hexaferrite, a longitudinal conical state (fig. 2.4.1.1 b) is stabilized above room temperatures and the finite polarization is induced by a magnetic field, *H,* applied in the ab plane [Tokunaga, 2012]. Because the longitudinal-conical spin state is sustained above room temperatures, M-type hexaferrites have the potential to show magnetically induced polarization at room temperature. However, its low resistivity at room temperature is an issue to be solved.
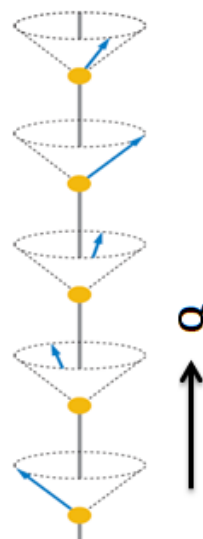

Fig. 2.4.1.1 Longitudinal-conical magnetic structure of M-type Ba(Fe,Sc,Mg)$_{12}$O$_{19}$ hexaferrite, from [Kimura, 2012]. *Q* denotes the magnetic modulation vector.

2.4.2 W-type

W-type hexaferrite crystal structures (Fig. 2.4.2.1 a) belong to $P6_3/mmc$ space group and contain $RS_2R^*S_2^*$ stacking sequence (table 4.1), which is very similar to the stacking sequences of M type hexaferrites. R is a three-oxygen-layer block, S (spinel block) is a two-oxygen-layer block and the star means that the corresponding block has been turned $180°$ around the hexagonal axis. The metal cations in W-type are situated in seven crystallographically non-equivalent positions, see fig. 2.4.2.1 b [Song, 2014].
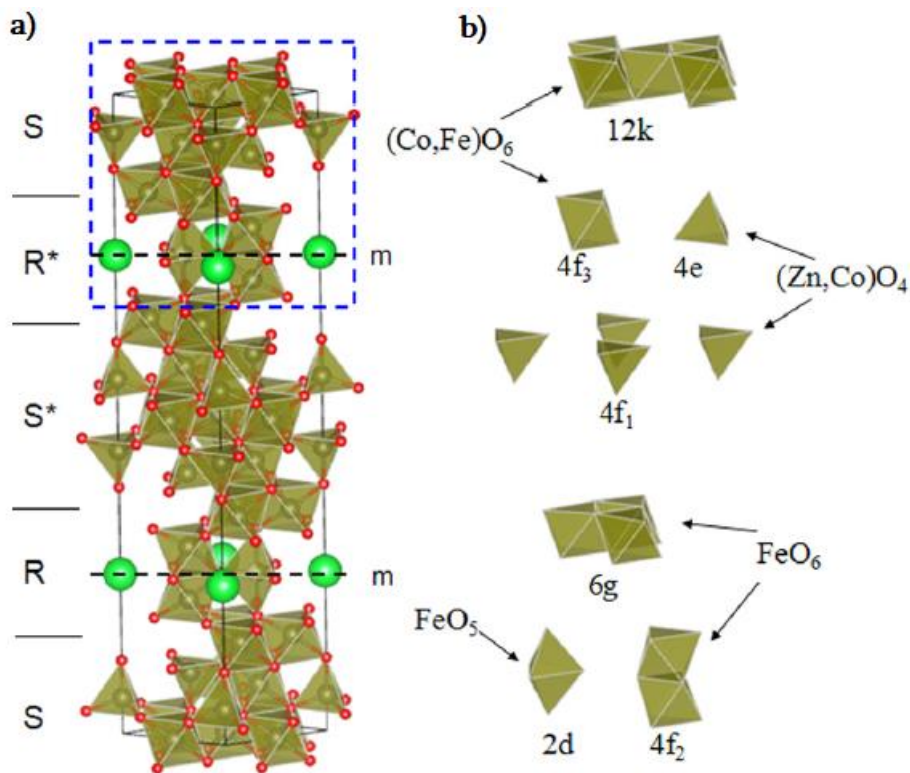

Fig. 4.1.2.1: a) Schematic view of the crystal structure of W-type hexaferrite with hexagonal *c-axis* vertical (the star means that the corresponding block has been turned $180°$ around the hexagonal *c-axis* and *m* denotes mirror plane) and b) crystallographically non-equivalent positions of W-type hexaferrite. Reproduced from Ref. [Song, 2014].

Recently, it was discovered that W-type $SrZn_{1.15}Co_{0.85}Fe_{16}O_{27}$ hexaferrite has a ME coupling near room temperature [Song, 2014]. Co^{2+} ions are located in octahedral site and have a strong planar contribution in the anisotropy. Therefore, some spin-reorientation transitions can be observed in Co-doped W-type hexaferrites. It can be seen from figure

4.1.2.2 that this compound shows complicated thermomagnetic behaviour, which can be understood in terms of the change of magnetocrystalline anisotropy [Song Y, 2014]. As is known, the W-type hexaferrites have an easy axis of magnetization along the c-axis due to the contribution of the spin from the bipyramidal Fe^{3+} cations in R-block. In the S-block Co^{2+} ions have a strong planar contribution to the magnetic anisotropy, which causes altering of the easy axis of magnetization in the Co-doped W-type hexaferrites.
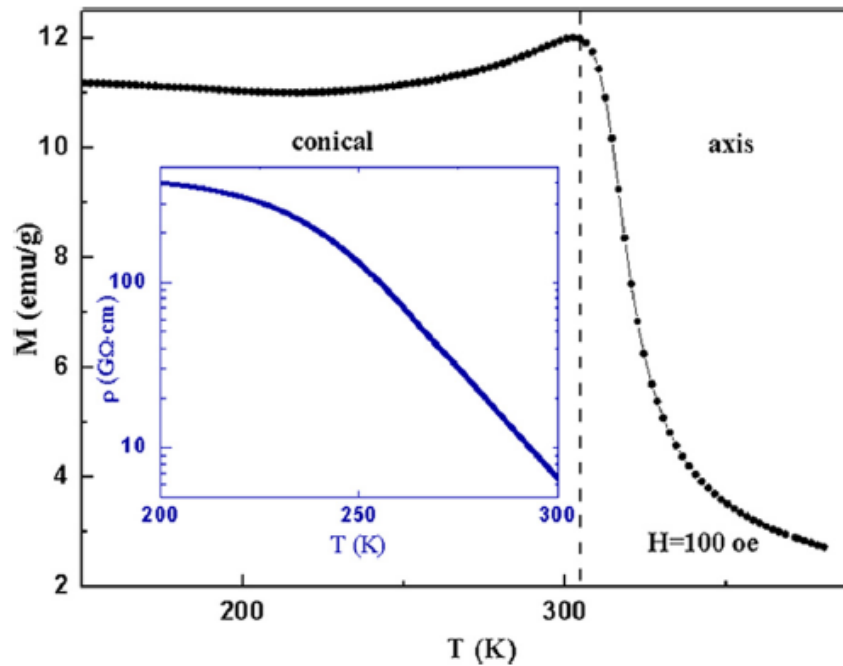

Fig. 4.1.2.2 Temperature dependence of the magnetization for W-type $SrZn_{1.15}Co_{0.85}Fe_{16}O_{27}$ hexaferrite measured at 0.01 T, from [Song, 2014]. The inset shows the variation of electrical resistivity as a function of temperature of the sample.

The axial anisotropy of S-block and planar anisotropy of R-block is strong and opposite, but the superexchange interaction between magnetic ions crossing the boundary between S and R blocks and tends to keep their magnetizations aligned. The competition between magnetocrystalline anisotropy and the superexchange interaction results in the series of spin-reorientation transitions, which is the origin of the complex thermomagnetic behavior in this compound.
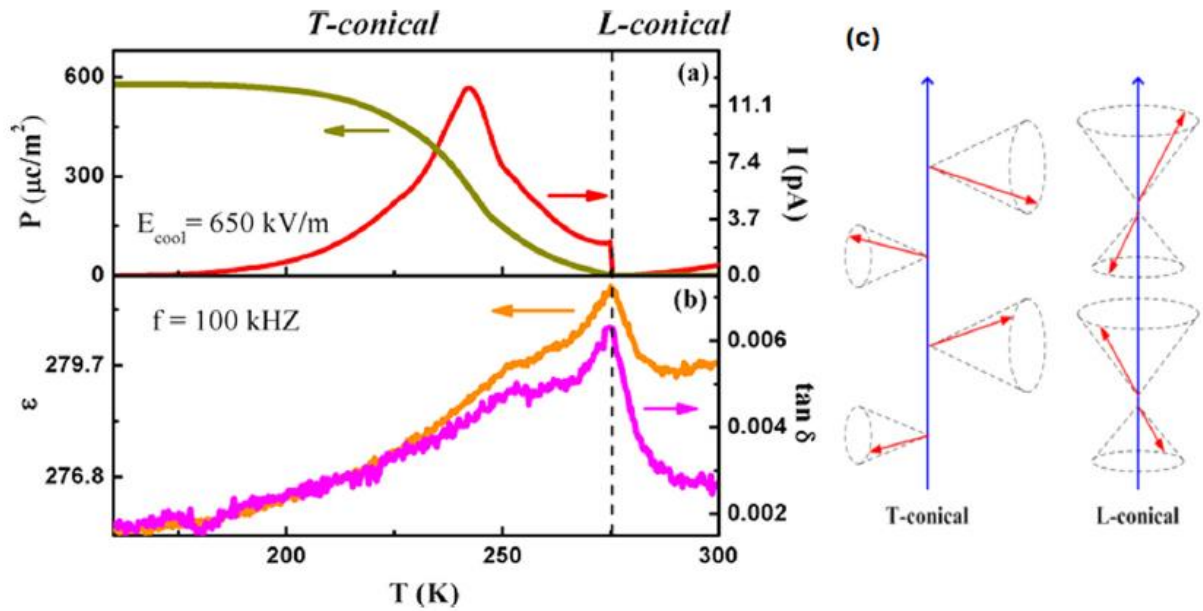
Fig. 4.1.2.3: a) Temperature dependence of pyroelectric current and ferroelectric polarization, b) Temperature dependence of relative dielectric constant for SZCFO measured at a frequency of 100 kHz for W-type SrZn$_{1.15}$Co$_{0.85}$Fe$_{16}$O$_{27}$ hexaferrite and (c) Schematic images of spin structure for T and L conical, from [Song, 2014].

The Curie temperature for W-type hexaferrites is above 600 K [Purushotham, 1996]. Below the Curie temperature W-type SrZn$_{1.15}$Co$_{0.85}$Fe$_{16}$O$_{27}$ compound has collinear ferromagnetic ordering with easy magnetization parallel to *c-axis*. With decreasing of the temperature easy-plane spin order of Co^{2+} ions begins to affect the magnetic anisotropy and at 302 K easy magnetization direction changes. Based on the earlier studies, it is likely that the spin shows conical order with an angle with respect to the *c*-axis around T=302 K [Paoluzi, 1988; Collomb, 1988]. Inset of figure 4.1.2.2 shows the temperature dependence of resistivity. As can be seen, the resistivity is quite high (ρ=6.5 GΩ·cm at 300 K). Figure 4.1.2.3 a displays the temperature dependence of pyroelectric current and ferroelectric polarization of W-type SrZn$_{1.15}$Co$_{0.85}$Fe$_{16}$O$_{27}$ compound. One can see that both pyroelectric current and ferroelectric polarization appear below 275 K. It was found that in the temperature range 275-302 K the spin system has L-conical structure (see Fig. 4.1.2.3 c). Below 275 K, where the electric polarization appears, the spin system has T-conical structure [Song, 2014]. Therefore, it can be concluded that the appearance of electric polarization is correlated with the change of magnetic structure in W-type SrZn$_{1.15}$Co$_{0.85}$Fe$_{16}$O$_{27}$ hexaferrite. Fig. 4.1.2.3b

shows the relative dielectric constant and dielectric loss as a function of temperature at a frequency of 100 kHz. Both quantities have maximum at 275 K, which corresponds to a ferroelectric phase transition in $SrZn_{1.15}Co_{0.85}Fe_{16}O_{27}$. These results show that the W-type $SrZn_{1.15}Co_{0.85}Fe_{16}O_{27}$ hexaferrite has multiferroic properties below 275 K, which might be useful for practical applications.

2.4.3 Y-type

The most well-known hexaferrite is the Y-type. The crystal structure (fig. 2.4.3.1.a) of Y-type hexaferrite can be considered as an alternating stacking of the S and the T structural blocks ($TST'S'T''S''$ where, the apostrophe means the corresponding block is rotated by 120^0 around this axis) along the c axis. The fundamental crystal structure of this compound belongs to the space group $R\bar{3}m$ (Table 2.4) and this group does not allow spontaneous polarization [Kimura, 2012]. The S blocks are same as in M-type hexaferrite, but the T-block ($Ba_2Fe_8O_{14}$) contains four layers of oxygen, with one Ba^{2+} ion substituting an oxygen ion in each of the two middle layers. One major difference in the transition metal sites in the T-block, compared to R-block in M-type hexaferrite, is that the trigonal bi-pyramidal site is absent in T-block. To understanding the magnetic structure of hexaferrites spin *block* model is widely accepted. According to the spin *block* model T and S structural blocks are indicated as L and S spin blocks. The L block has large and S small magnetic moment, respectively (fig. 2.4.3.1.a). The boundary of these blocks is located between the fourth [Fe(4)] and fifth [Fe(5)] layers, as shown in Figure 2.4.3.1 a. By replacing Ba ion with Sr, reinforcement of the superexchange interaction between these blocks is achieved [Pollert , 1985] and therefore, Fe(4)-O(2)-Fe(5) bond angle is changing. The Sr free crystal shows a collinear ferrimagnetic order (fig. 2.4.3.1.d) at 392 K with parallel orientations of the Fe(4) and Fe(5) moments [Gorter, 1957].
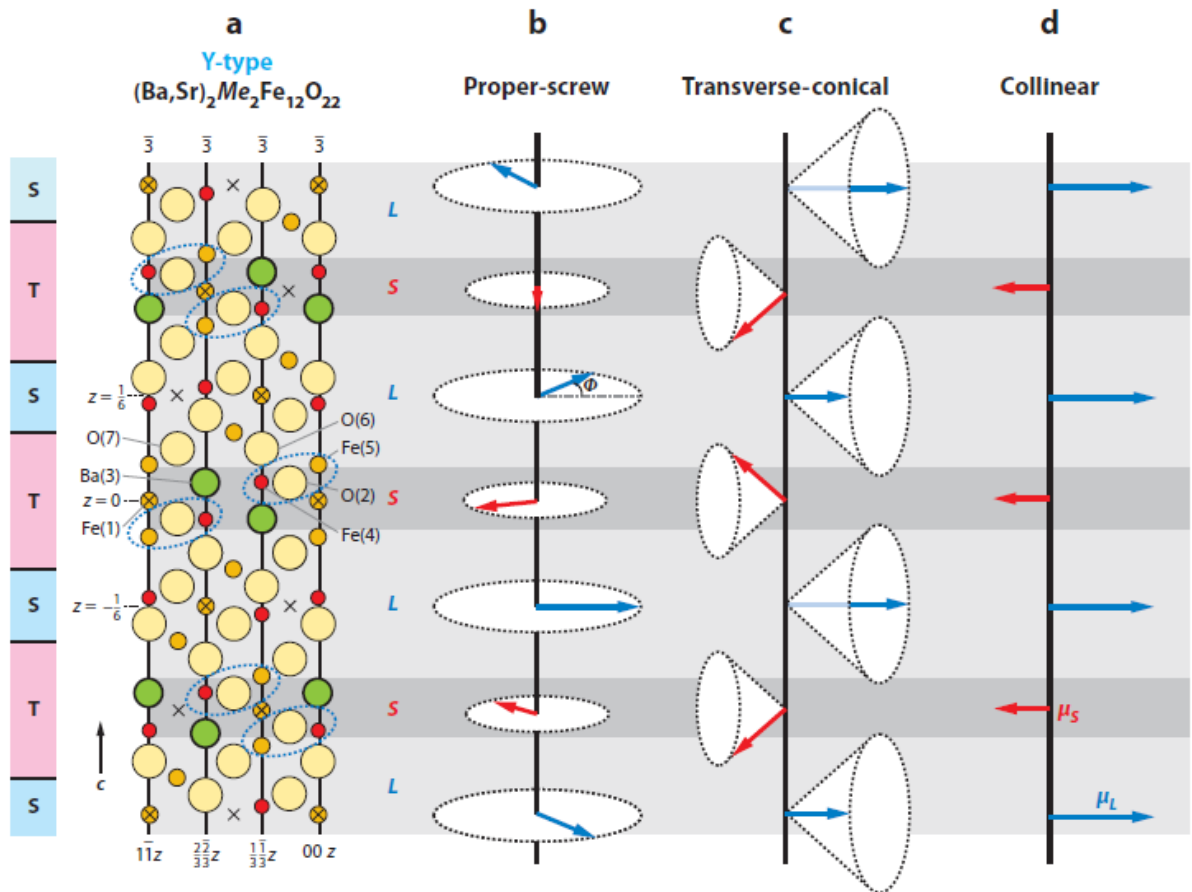
Fig. 2.4.3.1 : a) crystal structure of $(Ba,Sr)_2Me_2Fe_{12}O_{22}$ hexaferrite (Dashed blue ellipsoids are (Fe,Me)-O-(Fe,Me) bond angles), b) proper-screw magnetic structure, c) transverse-conical spin structure and d) collinear magnetic structure. The long (blue coloured) and short (red coloured) arrows are the effective magnetic moments of L and S magnetic blocks. Reproduced from Ref. [Kimura, 2012].

At room temperature in the Sr-rich samples, $Ba_{0.5}Sr_{1.5}Zn_2Fe_{12}O_{22}$, the angle between Fe(4) and Fe(5) moments becomes $\phi = 54°$ [Momozawa, 1985] and the system shows a proper-screw magnetic structure (Fig. 2.4.3.1.b). The increase of the bond angle causes the magnetic frustration at the boundary between the L and S blocks and then stabilizes a non-collinear screw magnetic structure. In the proper-screw magnetic structure, magnetically induced electric polarization cannot exist. However, by applying a magnetic field perpendicular to the c-axis, metamagnetic transitions take place and proper-screw magnetic structure transforms to the transverse-conical (Fig. 2.4.3.1.c). As a result, the system shows

magnetically induced electric polarization. Figure 2.4.3.2 presents results obtained in Ba$_{0.5}$Sr$_{1.5}$Zn$_2$Fe$_{12}$O$_{22}$ hexaferrite by Kimura *et al.* [Kimura, 2012].
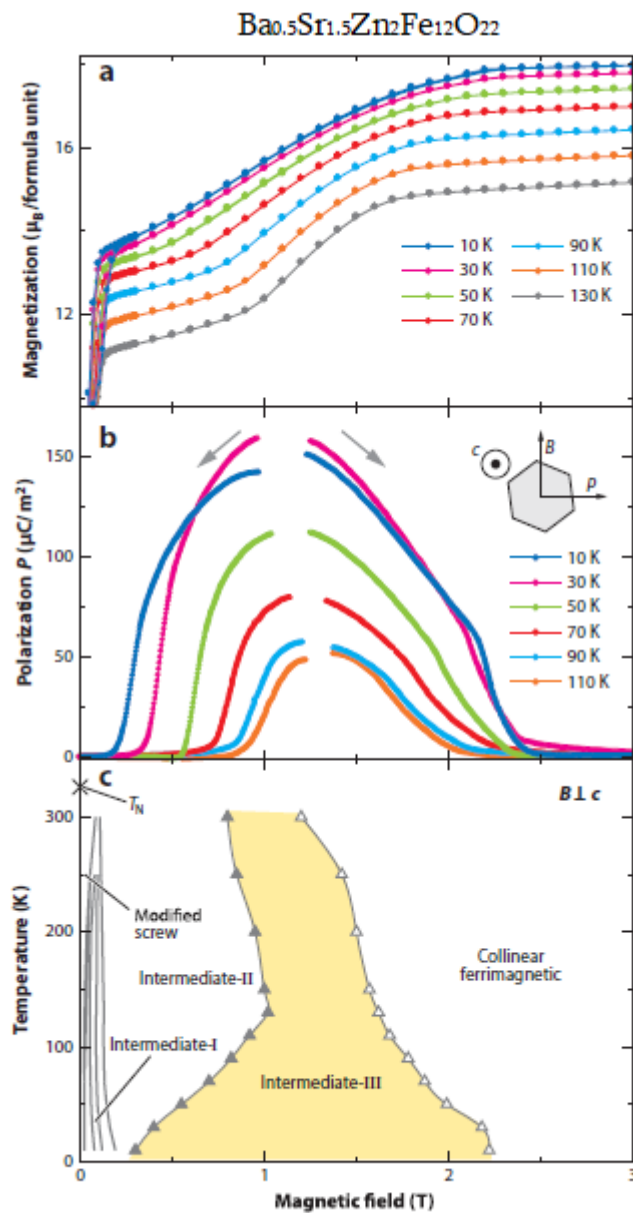
Fig. 2.4.3.2: a) magnetization versus magnetic field and b) electric polarization of the single crystal of Ba$_{0.5}$Sr$_{1.5}$Zn$_2$Fe$_{12}$O$_{22}$ hexaferrite at the temperatures. The magnetic field is perpendicular to the c axis and experimental configurations are shown in the inset. c) Magnetic phase diagram of the Ba$_{0.5}$Sr$_{1.5}$Zn$_2$Fe$_{12}$O$_{22}$ hexaferrite. The magnetic field is applied perpendicular to the c axis. The yellow area denotes the ferroelectric intermediate-III phase. Reproduced from Ref. [Kimura, 2012].

One can see from fig. 2.4.3.2a that M(H) curves in $Ba_{0.5}Sr_{1.5}Zn_2Fe_{12}O_{22}$ have unusual shape different form typical ferrimegnetic compound. With increasing magnetic field magnetization increases stepwise, which means that some metamagnetic transitions takes place [Momozawa, 1985]. Using this magnetization data and neutron diffraction results [Momozawa, 1993; Momozawa, 1985] the magnetic phase diagram was obtained (fig. 2.4.3.2c).

Figure 4.1.3.2b shows that no spontaneous polarization exists at zero magnetic fields. The electric polarization shows a rapid increase at the first metamagnetic transition field. With further increase of magnetic field, the electric polarization has maximum and finally vanishes at the transition into the collinear ferrimagnetic phase. According to these experimental results the magnetically induced polarization is the most evident in the intermediate-III phase and only Intermediate-III phase is ferroelectric. It will be shown later that the intermediate-II phase is also ferroelectric.

2.4.4 X-type

The X-type ferrite has a $(RSR^*S_2^*)_3$ stacking sequence and belongs to R$\bar{3}$m space group. The crystal structure (Fig. 2.4.1 c) is combinations of M and W phases and is extremely hard to separate. The first pure phase X-type hexafferrite was produces by J. Smit in 1959 [Smit, 1959]. The X-type hexaferrite has high anisotropic field, high saturation magnetization, low coercivity and small remanence. All these factors enhance its microwave absorbing properties [Zunuzovi, 2015; Sadiq, 2014]. For achieving the maximum value of the microwave absorption the incident microwave should be able to enter material at its greatest extent and the incident wave can be attenuated entirely. Figure 2.4.4 shows the variation of attenuation constant with frequency [Sadiq, 2014]. The attenuation constant has maximum value at high frequency (12.858 GHz), which is in good agreement with the reflection loss results. The successive reflection loss of 23.4 dB at 12.858 GHz makes this material promising for applications at high frequencies.
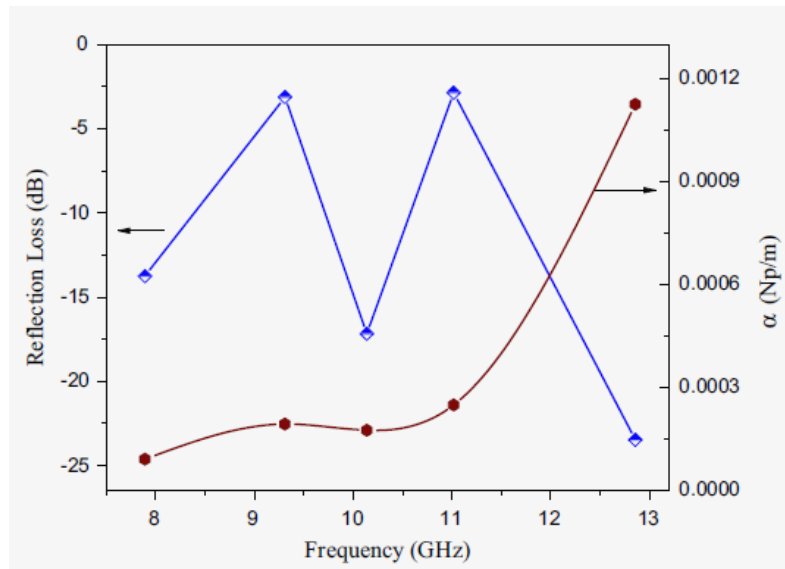
Fig. 2.4.4. Variation of reflection loss (blue colour line) and attenuation constant (wine colour line) of X-type $Sr_{1.94}Ce_{0.06}Ni_2Fe_{27.7}Zn_{0.3}O_{46}$ hexaferrite with frequency, from [Sadiq, 2014].

2.4.5 Z-type

In the year 2010, room temperature magneto-electric coupling was demonstrated in Z-type hexaferrite [Kitagava, 2010]. The structure of this compound (Fig.2.4.1 d) belongs to $P6_3/mmc$ space group and has a long stacking sequence ($RSTSR^*S^*T^*S^*$) of the S, R and T structural blocks (Table 4.1).

Fig. 2.4.5.1: a) magnetic field dependence of dielectric constant and b) dielectric loss tangent measured at 100 kHz of Z-type $Sr_3Co_2Fe_{24}O_{41}$ polycrystalline sample, from [Kimura, 2012].

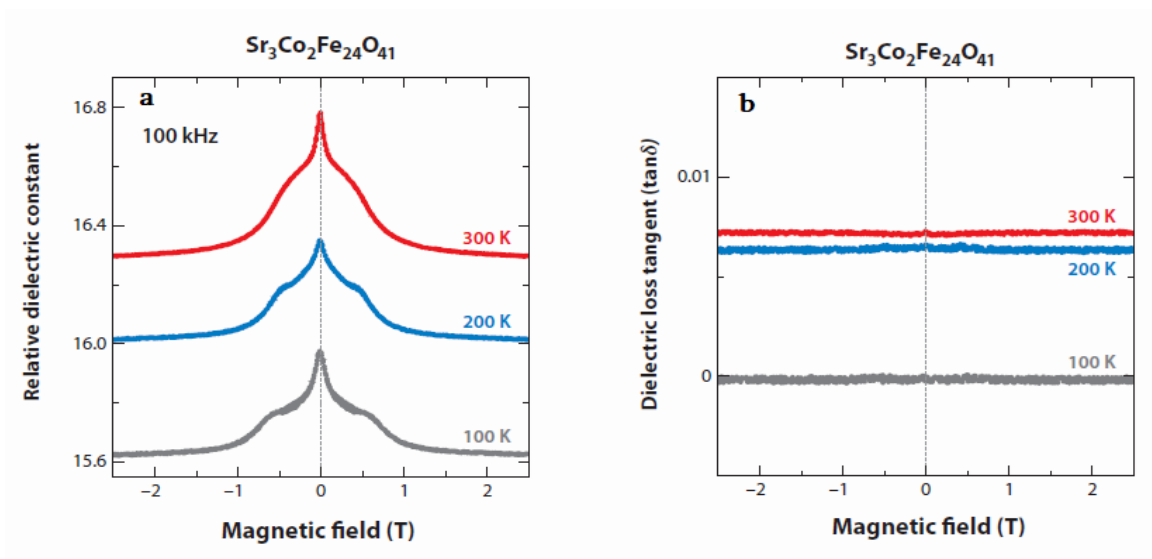Therefore, single Z phase is extremely hard to produce. Z-type $Sr_3Co_2Fe_{24}O_{41}$ hexaferrite has a high resistivity, small value of the loss tangent and dielectric constant at room temperature, as shown in figs. 2.4.5.1 a,b [Kimura, 2012].
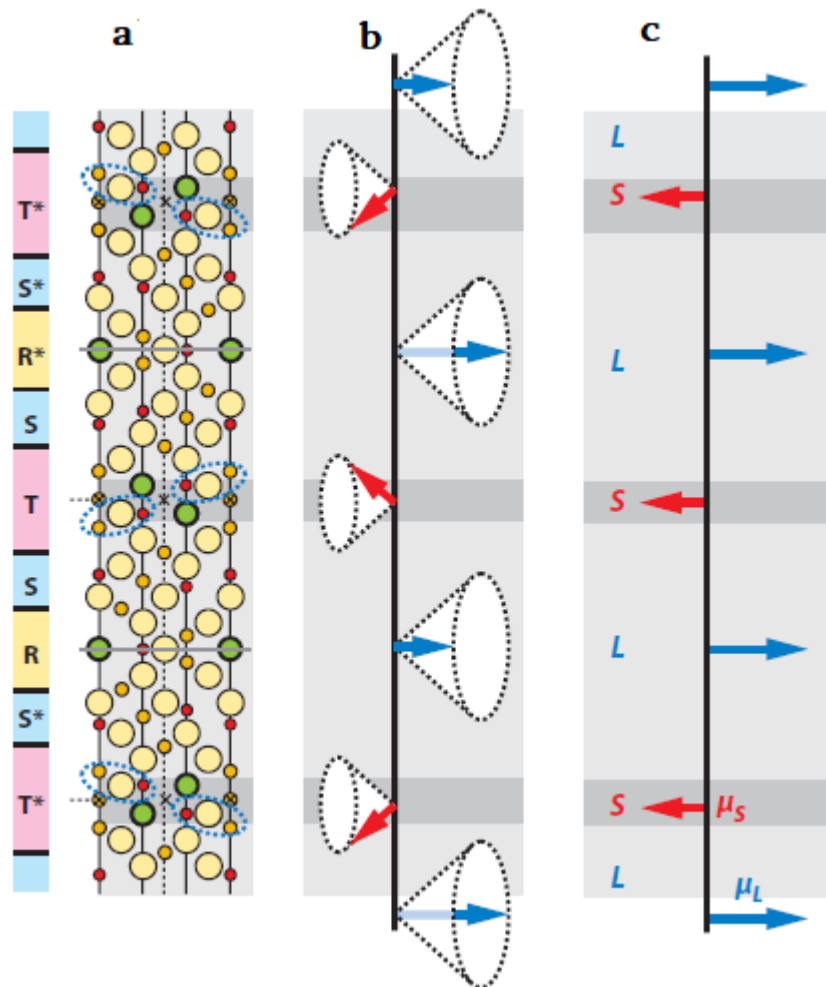
Fig. 2.4.5.2: a) crystal structure of Z-type $Sr_3Co_2Fe_{24}O_{41}$ hexaferrite (Dashed blue ellipsoids are Fe(4)-O(2)-Fe(5) bond angles), b) spiral magnetic ordering and c) ferromagnetic ordering, from [Kimura, 2012].

Figure 2.4.5.3a shows that with increasing magnetic field the magnetization increases in two steps and then saturates [Kimura, 2012]. The magnetization shows a rapid increase from 0 to 0.1 T, with further gentle increase from 0.1 to 0.7 T and at around 1 Tesla almost saturates. Figure 2.4.5.3 b demonstrates that there is no spontaneous electric polarization at zero magnetic field, but by applying a magnetic field electric polarization appears at ~0.2 T

and reaches its maximum value at around 0.3 T. With the further increase of the magnetic field, the electric polarization starts to decrease. At 1 T the electric polarization vanishes and system becomes a simple ferrimagnet (Fig. 2.4.5.2 c). Figure 2.4.5.3b also shows that the electric polarizations persist till 300 K. These results demonstrate that the Z-type hexaferrite $Sr_3Co_2Fe_{24}O_{41}$ can be suitable for practical applications.

Fig. 2.4.5.3: a) magnetic field dependence of magnetization (inset shows a zoomed views of magnetization at 300 K) and b) electric polarization at 100, 200 and 300 K temperatures for $Sr_3Co_2Fe_{24}O_{41}$ polycrystalline sample (inset represents the experimental configurations). Reproduced from Ref. [Kimura, 2012].

2.4.6 U-type

The U-type hexaferrite structure (Fig.2.4.1 f) with the space group $R\bar{3}m$ (Table 2.4) can be described as the sequence $(RSR^*S^*TS^*)_3$. The polycrystalline samples prepared by the solid state reaction method show a small but finite ME effect up to 350 K, which means that the U-type hexaferrite is a room temperature ME material [Okumura, 2011]. Figure 2.4.6 shows the magnetic field dependence of (a) magnetization and (b) electric polarization at different temperatures for polycrystalline $Sr_4Co_2Fe_{36}O_{60}$ sintered in an oxygen atmosphere.
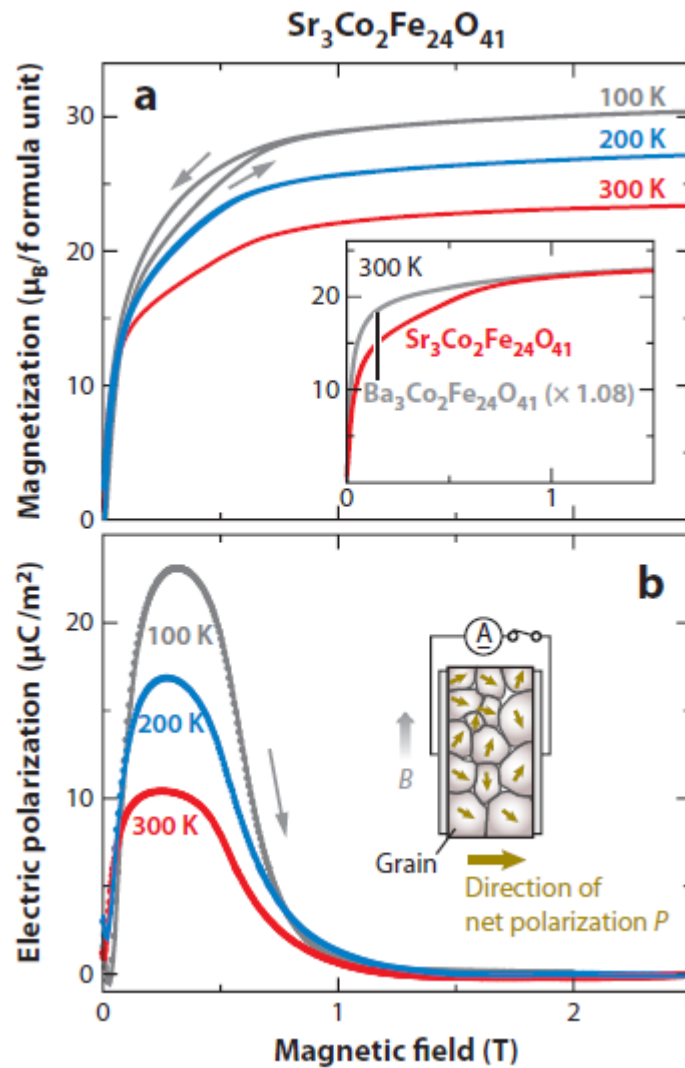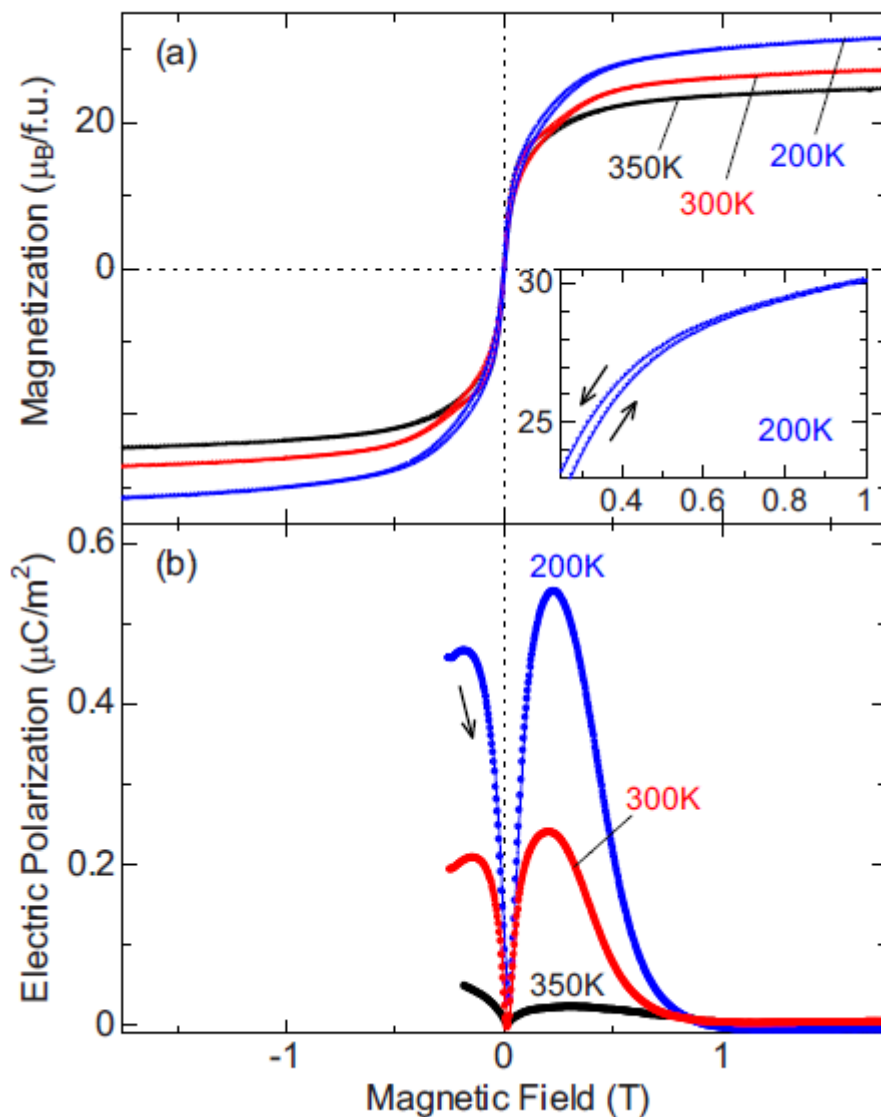

Fig. 2.4.6: a) magnetic-field dependence of the magnetization (inset represents a zoomed view of the data at 200 K) and b) electric polarization at selected temperatures for the U-type $Sr_4Co_2Fe_{36}O_{60}$ hexaferrite, from [Okumura, 2011].

As can be seen in figure 2.4.6 a, the *M(H)* curves show a small but substantial hysteresis and then the hysteresis vanishes at around 0.6 T (Fig. 2.4.6 a), and then *M* is nearly saturated above 0.8 T. The magnetic field dependence of the electric polarization reveals that the sample has magnetoelectic coupling. As is shown in figure 2.4.6 b, there is almost no spontaneous polarization at zero magnetic field. By applying magnetic field the electric polarization appears and rapidly increases up to 0.2-0.3 T and then starts to decrease. Finally, the electric polarization vanishes at around 0.7 T where *M* is almost saturated. These results demonstrate that U-type $Sr_4Co_2Fe_{36}O_{60}$ hexaferrite exhibits the ME effect in a wide range of temperatures below 350 K.

2.5 Magnetic anisotropy

The magnetic anisotropy describes how magnetic properties of the objects can be different depending on direction. In the simplest case, there is no preferential direction for an object's magnetic moment. Magnetically anisotropic materials will be easier or harder to magnetize depending on which way the object is rotated. For most magnetically anisotropic materials, there are two easiest directions to magnetize the material, which are a 180° rotation apart. The line parallel to these directions is called the easy axis. The easy axis is an energetically favourable direction of spontaneous magnetization. There are several different types of anisotropy: magnetocrystalline and shape anisotropy.

2.5.1 Magnetocrystalline anisotropy

Magnetocrystalline anisotropy (MCA) originates from coupling between the spin and orbital degrees of freedom in the crystal lattice. The simplest case of MCA can be considered as uniaxial anisotropy which can be written in the form of anisotropy energy (up to the fourth order terms) as [Kullity, 2011]:

$$E_{anisot} = K_{u1} sin^2\theta \, K_{u2} sin^4\theta \qquad\qquad (2.5.1)$$

where, θ is the angle between anisotropy axis and magnetization direction. Positive large values of K_{u1} favor an easy axis. For hexagonal systems, for positive values of K_{u1}, if $K_{u2} > K_{u1}$ *c-axis* is the easy axis and if $K_{u2} < K_{u1}$ basal plane is the easy plane. For negative values of K_{u1}, if $K_{u2} < -K_{u1}/2$ basal plane is the easy plane and if $2K_{u2} > -K_{u1}$ an easy cone is observed.

MCA is an intrinsic property of a ferrimagnet and is independent of grain size or shape. It can be most easily seen by measuring the magnetization curves along different crystal directions. Depending on the crystallographic orientation of the sample in the magnetic field, the magnetization reaches saturation in different fields, see figure 2.5.1 [Kasap, 1997]. For easy [100] direction the magnetic field to reach saturation is smaller than magnetic field hard [111] direction.

On the other hand, to magnetize the crystal along the [111] direction by applying a field along this direction is needed to apply a stronger field than that along [100].
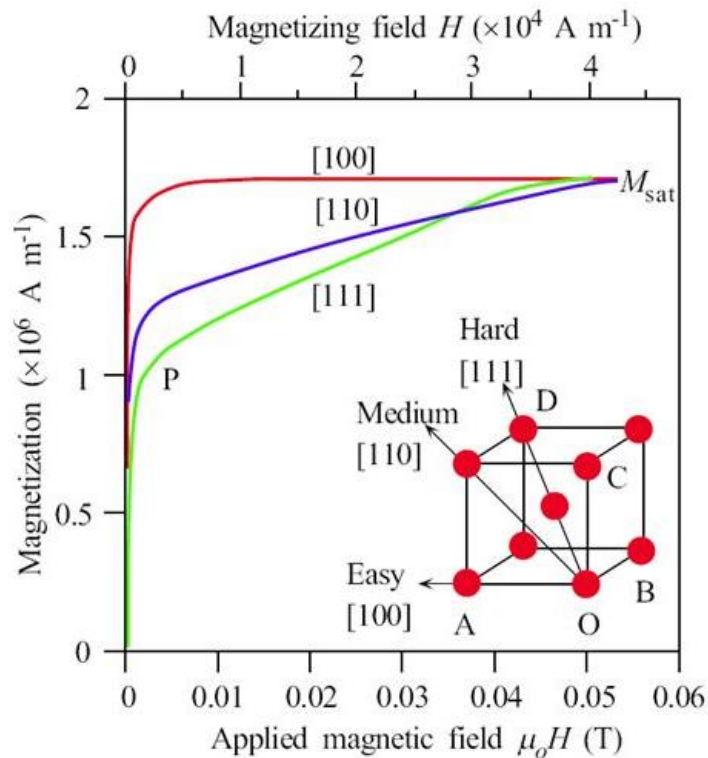

Fig. 2.5.1. Magnetocrystalline anisotropy in single iron crystal. *M* vs *H* depends on the crystal direction. Easiest magnetization is along [100] and hardest [111] direction, from [Kasap, 1997].

2.5.2 Shape anisotropy

The magnetic shape anisotropy is mediated by the dipolar interaction. This interaction is long range and depends upon the shape of the sample. A magnetized body will produce magnetic charges or poles at the surface. This surface charge distribution is itself another source of a magnetic field, called the demagnetizing field. When a particle is not perfectly spherical, the demagnetizing field (Eq. 2.5.2) will not be equal for all directions and creates one or more easy axes.

$$H_d = -NM \hspace{5cm} (2.5.2)$$

where, H_d is demagnetizing field, N demagnetizing factor (shape factor) and M magnetization. Demagnetizing factor is strongly dependent on the sample shape geometry. Therefore, H_d is depends on shape of the sample. On the table 2.5.2 are listed shape factor for the different geometries of the sample.

Sample geometry	Shape factor, N (dimensionless)
Flat sheet, $\vec{M}$ normal to surface	1
Long cylinder, $\vec{M}$ along length of cylinder	0
Long cylinder, $\vec{M}$ along width of cylinder	1/2
Sphere, $\vec{M}$ along orthogonal axes	1/3

Table 2.5.2 The shape factor for the different geometries of the sample.

2.5.3 Neutron scattering

In order to determine the properties of the matter on the atomic scale (10^{-10}m) the neutron scattering is the best tool. *Neutron scattering* provides a direct measure of spatial and temporal correlations of atomic positions and magnetic states of the target system. The first neutron diffraction experiments were performed in the 1930s. Neutrons have some very

specific properties which make them extremely useful for condensed matter studies. Neutrons are subatomic particles with no net electric charge, unlike other particles such as protons and electrons, which have an intrinsic electric charge. Coulomb forces involving strong charge repulsion or attraction, charge-free neutrons can move through matter undeterred by these factors. The wavelengths of neutrons are similar to atomic spacings, like to the case for X-rays. Therefore they can provide structural information from the picometer to the 100 μm range. Neutrons can determine molecular vibration and lattice excitations, because of the energy of thermal neutrons is similar to the energy of elementary excitations in solids. A neutron is a spin 1/2 particle with magnetic moment -1.91 μ_N (μ_N -<u>nuclear magneton</u>), making it additionally sensitive to magnetic environment in the sample. The scattering potential ($V_n(\vec{r})$) for a neutron can be expressed as a sum of nuclear ($V_N(\vec{r})$) and magnetic ($V_M(\vec{r})$) contributions [Toperverg, 2015]. Therefore, *neutron scattering provides the opportunity to explore important information about atomic structure and dynamics.*

2.5.4 Nuclear scattering

In Nuclear scattering neutrons interacts with the nucleus of the atoms via nuclear forces and potential $V_N(\vec{r})$ is Fermi pseudo potential. Using Fermi pseudo potential for a crystal the nucleus scattering the scattering potential can be written as the sum of individual nuclear interaction:

$$V_N(\vec{r}) = \frac{2\pi\hbar h^2}{m_N} \sum_j b_j \delta(\vec{r} - \vec{r_j}) \qquad (2.5.4.1)$$

Where, j is nucleus which is located at position r_j, b_j is the scattering length of the nuclear scattering and δ Dirac delta function, respectively. In contrast to x-ray scattering the form factor for nuclear neutron scattering is independent of scattering vector ($\mathbf{Q}$), as the nucleus is much smaller compared to electron clouds and the scattering amplitude can be written as:

$$N(\vec{Q}) = \sum_j b_j \cdot e^{i\vec{Q}} \qquad (2.5.4.2)$$

The value of b_j is different for same atoms with different isotopes. To account for different distribution of different isotopes in nature we have to consider the average isotope distribution. So the differential scattering cross section can be written as:

$$\frac{d\sigma}{d\Omega} = \langle \sum_j b_j e^{i\vec{Q}\vec{r_j}} \ e^{-i\vec{Q}\vec{r_j}} \rangle = \langle b \rangle^2 |b_j e^{i\vec{Q}\vec{r_j}}|^2 + N\langle (b - \langle b \rangle)^2 \rangle \qquad (2.5.4.3)$$

Here, only the first term contains phase information (coherent scattering) and the second term is the incoherent scattering term contributing to the isotropic background.

2.5.5 Magnetic scattering

The magnetic moment of neutron interacts with magnetic field, also the magnetic dipolar moments originating from unpaired electronic spins. The dipolar interaction potential of a neutron with the magnetic field is given by $V_M = -\boldsymbol{\mu}_N \cdot \boldsymbol{B}$ where $\boldsymbol{B}$ is the magnetic induction. In the scattering process a neutron changes its spin moment in its quantization axis z from σ_z to σ_z' (σ is spin operator) as wave vector changes from k to k'. The magnetic cross section can be written as:

$$\frac{d\sigma}{d\Omega} = \left| -\frac{1}{2\mu_B} \langle \sigma_z' | \hat{\sigma} \overrightarrow{M_\perp}(\vec{Q}) | \sigma_z \rangle \right|^2 \qquad (2.5.5.1)$$

Only $\overrightarrow{M_\perp}(\vec{Q})$ term contributes to magnetic scattering and is the Fourier transformed magnetization component perpendicular to $\vec{Q}$.

$$\overrightarrow{M_\perp}(\vec{Q}) = \hat{Q} \times \vec{M}(\vec{Q}) \times \hat{Q}$$
$$\vec{M}(\vec{Q}) = \int \vec{M}(\vec{r}) e^{i\vec{Q}\cdot\vec{r}} d^3r \qquad (2.5.5.2)$$
$$\vec{M}(\vec{r}) = \overrightarrow{M_s}(\vec{r}) + \overrightarrow{M_L}(\vec{r})$$

In contrast to nuclear scattering, magnetic neutron scattering depends on a form factor. In most of the transition metal compounds orbital magnetic moment is quenched. Contributions to $\vec{M}(\vec{Q})$ is only from the spin part.

$$\vec{M}(\vec{Q}) = -2\mu_B \cdot f_m(\vec{Q})\sum_i e^{i\vec{Q}\cdot\vec{r}} \cdot \vec{S_i}$$

(2.5.5.3)

$$f_m(\vec{Q}) = \int_{atom} \rho_s(\vec{r})e^{i\vec{Q}\cdot\vec{r}}d^3r$$

here, f_m is the magnetic form factor which is the Fourier transformation of the spin density ρ_s distribution of a single atom. The magnetic scattering takes place at the outer unpaired electrons, so form factor falls with similar to X-ray scattering. However, in magnetic scattering contributions are from only unpaired outer shell electrons whereas in X-ray all electrons contribute. The form factor fall is much faster in neutron magnetic scattering compared to that of X-ray scattering.

3 Experimental methods

3.1 Single crystal growth

The single crystals of good quality are essential to study physical properties of materials and to reveal their intrinsic properties. For example, only in single crystals it is possible to study anisotropic electric, magnetic and optical properties. Also, by using single crystals one can avoid spurious effects related to grain boundaries in polycrystalline samples. There are several methods to grow single crystals. In the present thesis we used flux method to obtain hexaferrite single crystals.

3.1.1 Flux growth method

The flux method is one of the most commonly used processes to produce bulk single crystals. The solute components of the desired substance are dissolved in the molten solvent at high temperature. The solute-solvent ratio determines the growth temperature of this method. The flux allows the growth to carry on well below the melting temperature of the solute material. This is the main advantage of the flux growth. Simple materials (Ni, Fe...), oxides (B_2O_3, Bi_2O_3), hydroxides (KOH, NaOH), salts (BaO, PbO...) can be used as a solvent.

Production of metallic crystals generally uses crucibles made from ceramics such as alumina, zirconia and boron nitride. Also, to avoid impurities, high quality (99.9997 %) platinum crucible are used. Figure 3.1.1 shows the platinum crucible (left) and schematic view of the crystal growth inside the crucible (right).
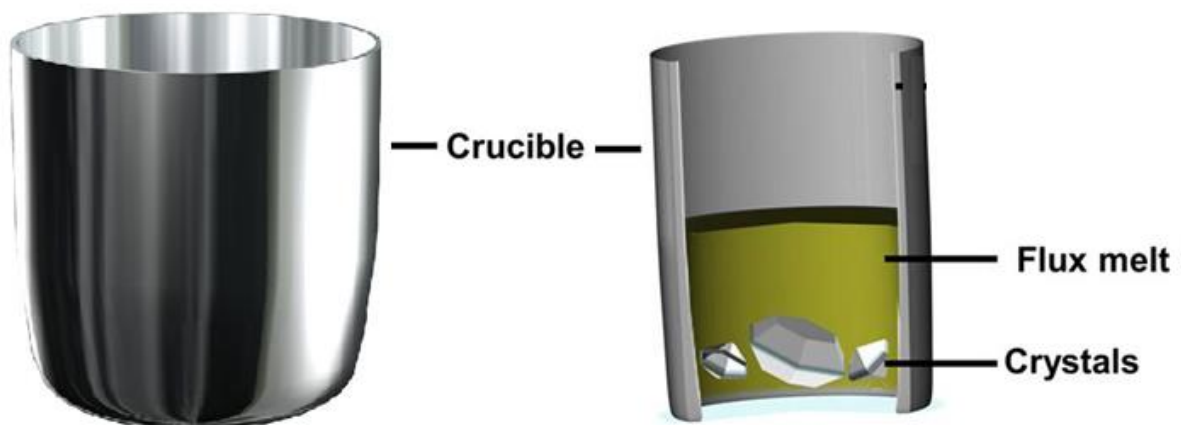

Fig. 3.1.1. The high quality (99.9997 %) platinum crucible (left) and schematic view of crystal growth inside crucible (right). Yellow is flux melt and the grown crystals are shown at the bottom.

To understand more about the flux method the phase diagram is needed. A typical example of a phase diagram used in crystal growth is shown in Fig. 3.1.1.2 a [Elwell & Scheel]. The solute material is an element or a compound with a melting point generally higher than that of the solvent, but in principle it is possible to grow crystals from eutectic systems in which the solvent has a higher melting point. A eutectic system is a homogeneous

mixture of substances that melts or solidifies at a single temperature that is lower than the melting point of any of the components. A solution of composition n_A equilibrated at temperature T_A can be cooled, in the absence of secondary nucleation aids and agitation, to a temperature T_B for spontaneous nucleation formation. In the region between the liquid's and the critical temperature curves intersecting *B* the solution can be under cooled or supersaturated. This region is called the metastable region. The metastability results because a nucleus of critical size must be formed before crystalline material is precipitated [Elwell & Scheel]. Similarly, crystallization can be made with desirable composition or ratio of the solute and solvent for desirable growth temperature. The metastable region is very important to the growth the crystals, the experimental conditions must be controlled to avoid unwanted nucleation. Therefore, in order to avoid the formation of unwanted phases, temperature oscillation method is used. A typical temperature cycling process is shown in Fig. 3.1.1.2 b.
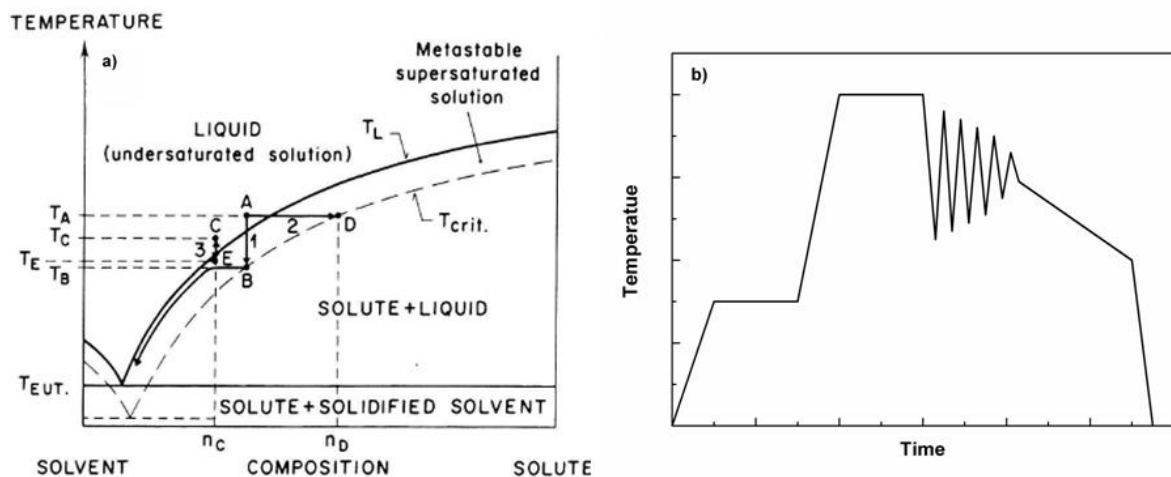

Fig. 3.1.1.2: a) Eutectic phase diagram showing the metastable region and crystal growth by slow cooling (1), by solvent evaporation (2) and by gradient transport (3), from Ref. [Elwell & Scheel] and b) typical temperature profile in the crystal growth.

3.2 Single-crystal X-ray diffraction

The discovery of X-ray diffraction by crystals was made in April 1912 by Laue [Forman, 1969]. X-rays are electromagnetic radiation with wavelengths between about 0.01 – 100 Å. X-rays have a shorter wavelength (wavelength has the same order as the spacing of the atoms), higher frequency, higher energy and high penetration power. Due to these properties of X-rays, they are used in X-ray crystallography. The oldest and most precise method of X-ray crystallography to determine a crystal's structure is single-crystal X-ray diffraction (XRSC). In the single-crystal X-ray diffraction experiment (see Fig. 3.2.1), an intensive beam of X-rays strikes a studying single crystal. Depending on the crystal structure and orientation, the crystal diffracts the X-ray beam differently. The diffracted X-rays beam makes a diffraction pattern of spots on the detector. These spots are called reflections.
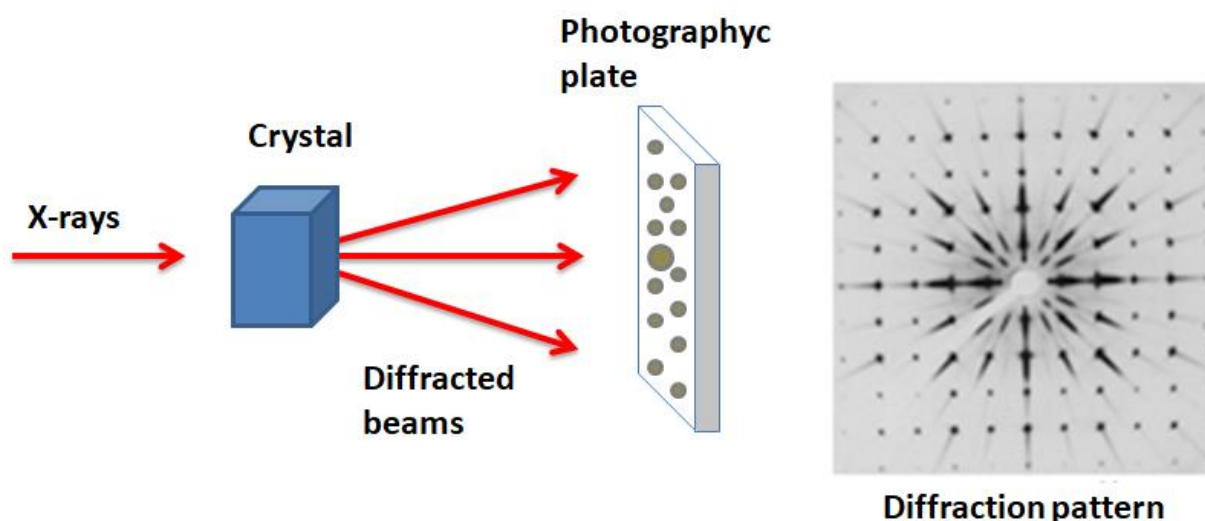

Fig. 3.2.1. The single-crystal X-ray diffraction experiment (left) and diffraction pattern (right).

The diffraction pattern consists of reflections of different intensity which can be used to determine the structure of the crystal. Reflection of X-rays only occurs when the condition of the Bragg's law is satisfied:

$$n\lambda = 2d\sin(\theta) \hspace{3cm} (3.2.1)$$

Bragg's equation describes the relationship for constructive interference, where x-rays of wavelength λ incident on the material at angle θ are diffracted by crystal planes separated by distance d and n represents an integer. The constructive interference occurs only when Eq. 3.2.1 is satisfied. Fig. 3.2.2 shows a schematic representation of Bragg's law.
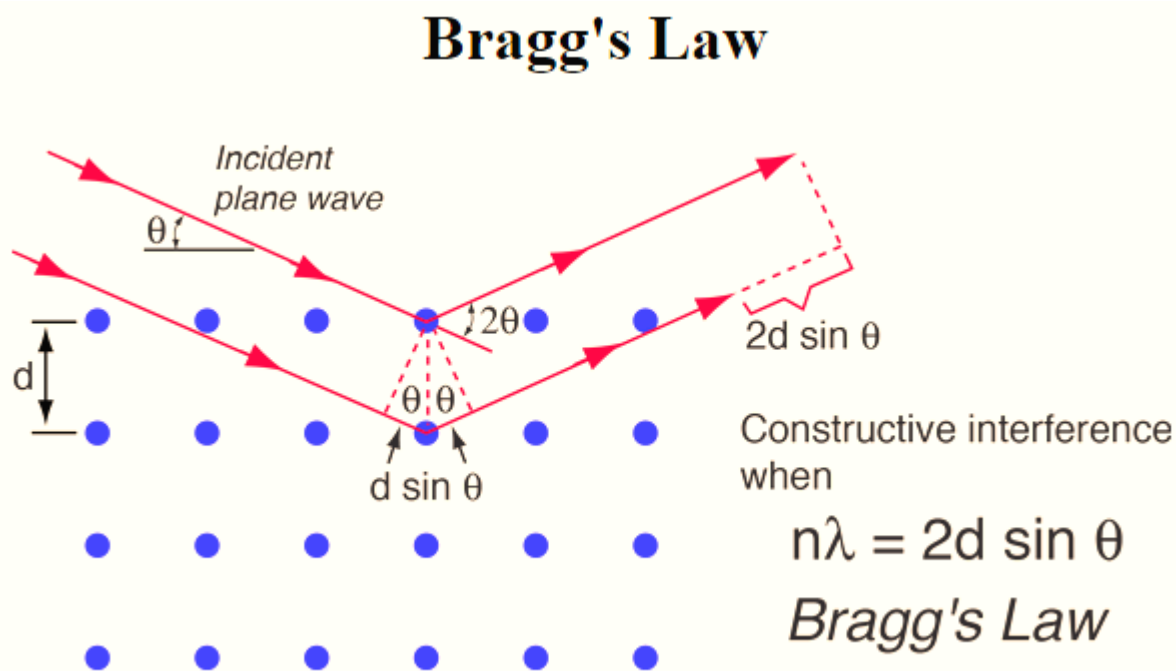

Fig. 3.2.2. Schematic representation of Bragg's law. Here, λ is the wavelength of the incident beam, d the space between the planes in the atomic lattice, n positive integer and θ angle of the incident beam. Reproduced from Ref [Bragg's law, 2020].

One of the best single-crystal X-ray *diffraction* instruments is Rigaku Oxford *Diffraction (Supernova)*. This instrument is equipped with cooling facilities for low-temperature experiments, kappa-axis four-circle goniometer (omega, kappa, phi and theta axis) for sample orientation with CCD area or scintillation point detector arm (Fig. 3.2.3) and also, both Cu and Mo microfocus X-ray sources. The X-rays are generated by a micro-focus sealed tube, which is mounted on the goniometer and powered by the high voltage X-ray generator. The X-ray optic consists of a high-speed shutter located next to the tube shield, X-ray focusing optics and a collimator for refining the X-ray beam.
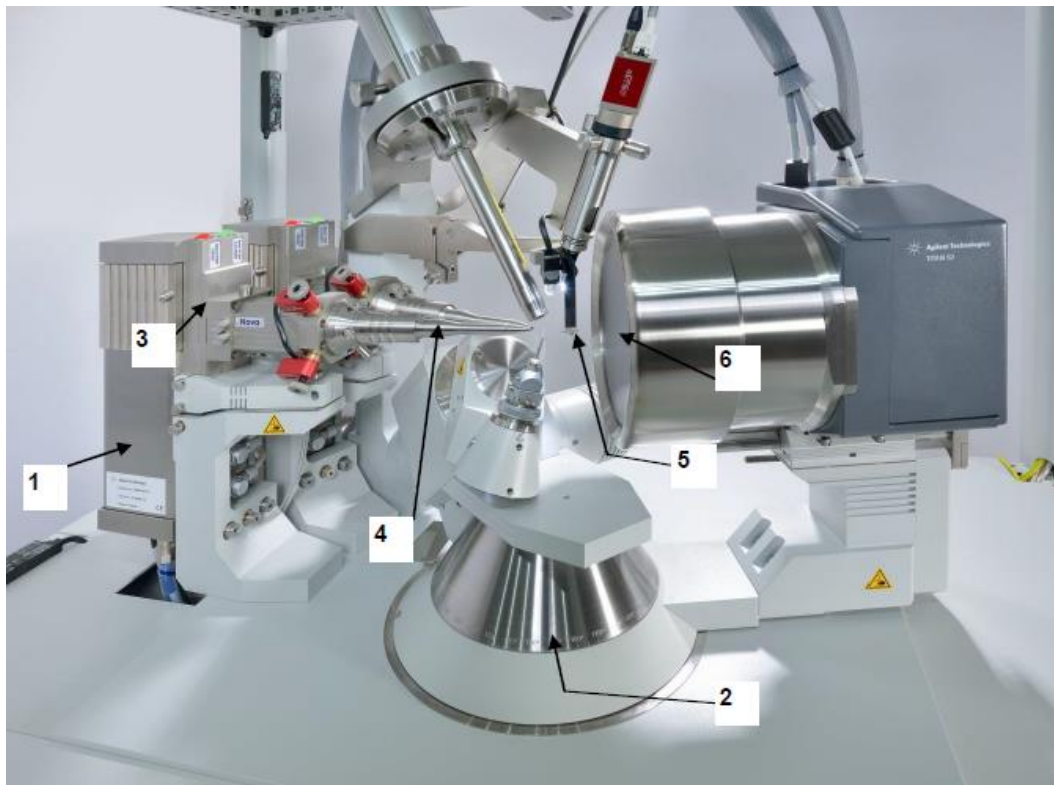
Fig. 3.2.3. The view of the diffractometer: 1) X-ray tube, 2) four-circle Kappa goniometer, 3) X-ray shutter, 4) collimator, 5) beamstop and 6) beryllium window, from [Agilent Technologies, 2014].

3.3 DynaCool Physical Property Measurement System with VSM option

The physical property measurement system (PPMS) is a multipurpose fast and sensitive DC magnetometer, which can be used to determine the properties of materials, including electrical resistivity, magnetization, Hall Effect, heat capacity, thermal conductivity and thermal transport with a high degree of accuracy as a function of temperature or magnetic field. The DynaCool PPMS system is designed to measure the physical properties of materials in bulk, thin film and powder form in broad temperature interval 0.35 - 400 K, up to 16 Tesla of the magnetic field. The high magnetic field is reached using the large superconducting magnet, which is cooled by liquid helium. The VSM option transforms PPMS into a sensitive (sensitivity about 10^{-6} emu) DC magnetometer. The VSM option for the PPMS consists primarily of a VSM linear motor transport for vibrating the sample with 40 Hz in the vertical

direction and relatively large oscillation amplitude (1–3 mm peak), a coilset puck for detection, electronics for driving the linear motor transport and detecting the response from the pickup coils. The Operating principle for the VSM option in the PPMS is illustrated in Fig. 3.3.1.

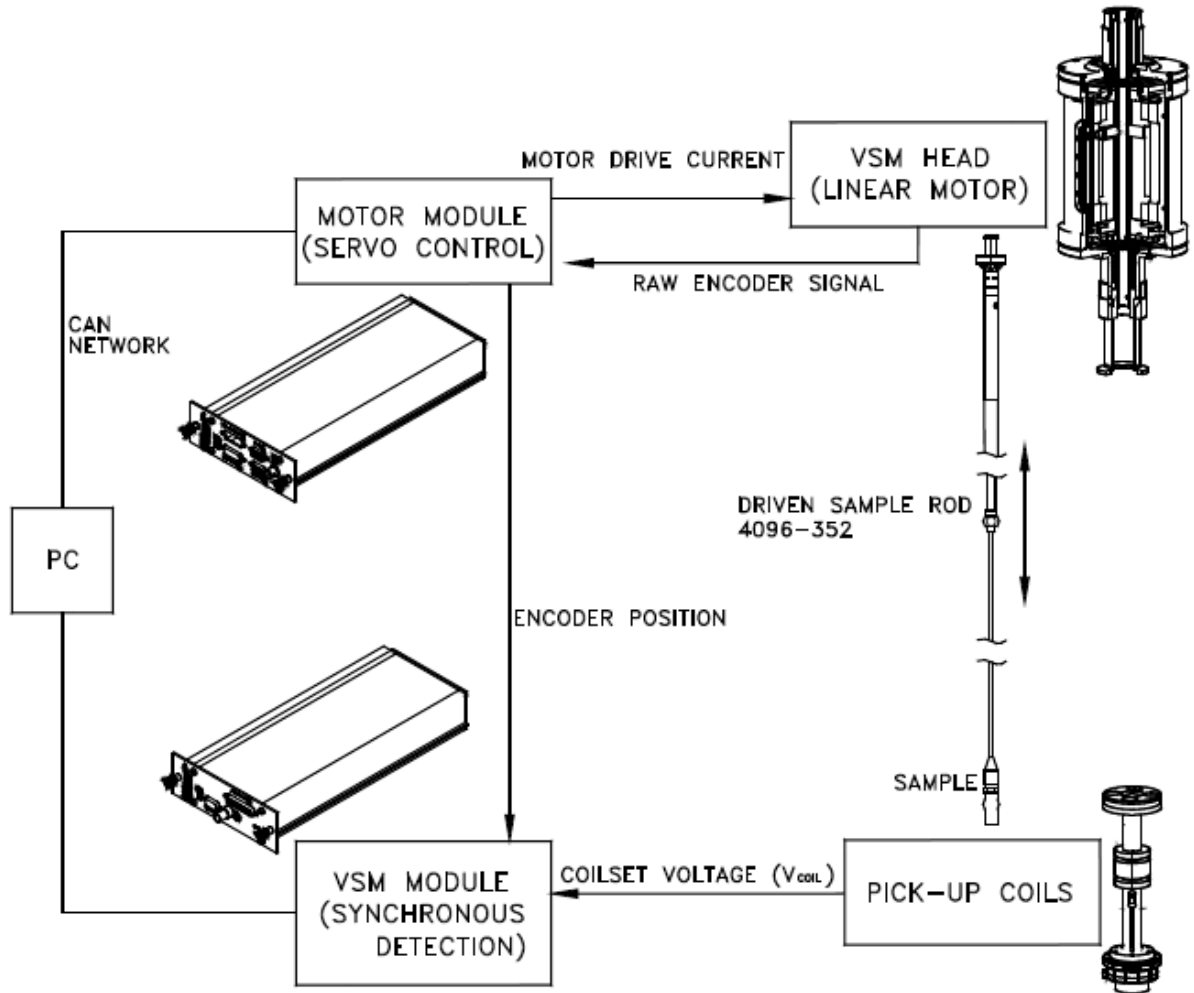Fig. 3.3.1. The operating principle for the VSM option in the PPMS, from [Quantum Design, 2008].

The basic principle of operation for a VSM is that a changing magnetic flux induces a voltage in a pickup coil. The time-dependent induced voltage is given by the following equation [Quantum Design, 2008]:

$$V_{coil} = \frac{d\phi}{dt} = \left(\frac{d\phi}{dz}\right)\left(\frac{dz}{dt}\right) \qquad\qquad 3.3.1$$

where, ϕ is the magnetic flux enclosed by the pickup coil, z the vertical position of the sample with respect to the coil and t is time. For a sinusoidal oscillating sample position, the voltage is based on the following equation:

$$V_{coil} = 2\pi f C m A \sin 2\pi f \qquad\qquad 3.3.2$$

where, C is coupling constant, m the DC magnetic moment of the sample, A the amplitude of oscillation and f the frequency of oscillation. By measuring the voltage induced in the detection coil, it is possible to determine the magnetic moment of the sample. The sample is mounted between two pick-up coils (Fig. 3.3.2) by a linear motor head. The sample is vibrated with 40 Hz in the vertical direction. Oscillation of the magnetic moment induces an electric current in the pick-up coil. Lock-in technique is used to separate the sample signal from the noise.
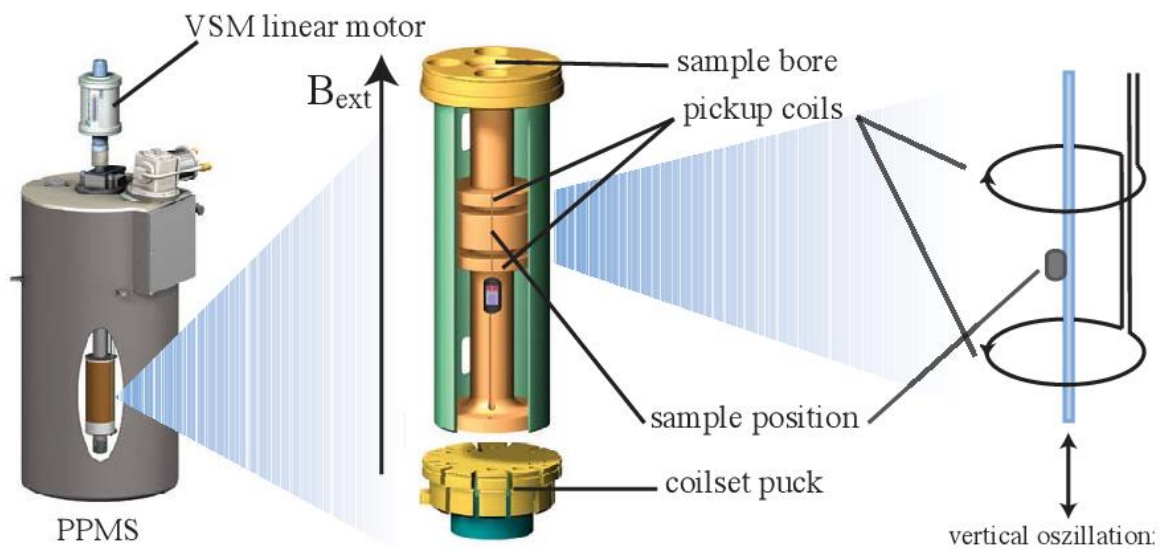

Fig. 3.3.2. PPMS system with VSM option. The VSM option for the PPMS consists primarily of a linear motors transport head for vibrating the sample and an oppositely wound coil set for detection. Reproduced from Ref. [Schmid, 2006].

3.4 Electron paramagnetic resonance

Electron paramagnetic resonance (EPR) or electron spin resonance (ESR) spectroscopy is a method for studying materials with unpaired electrons. Only EPR detects unpaired electrons unambiguously. In addition, EPR has the unique power to identify the paramagnetic species. EPR was first observed at Kazan State University in 1944 [*Zavoisky, 1945*]. The basic concepts of this technique are analogous to nuclear magnetic resonance, but it is the electro spins that are excited instead of the spins of atomic nuclei.
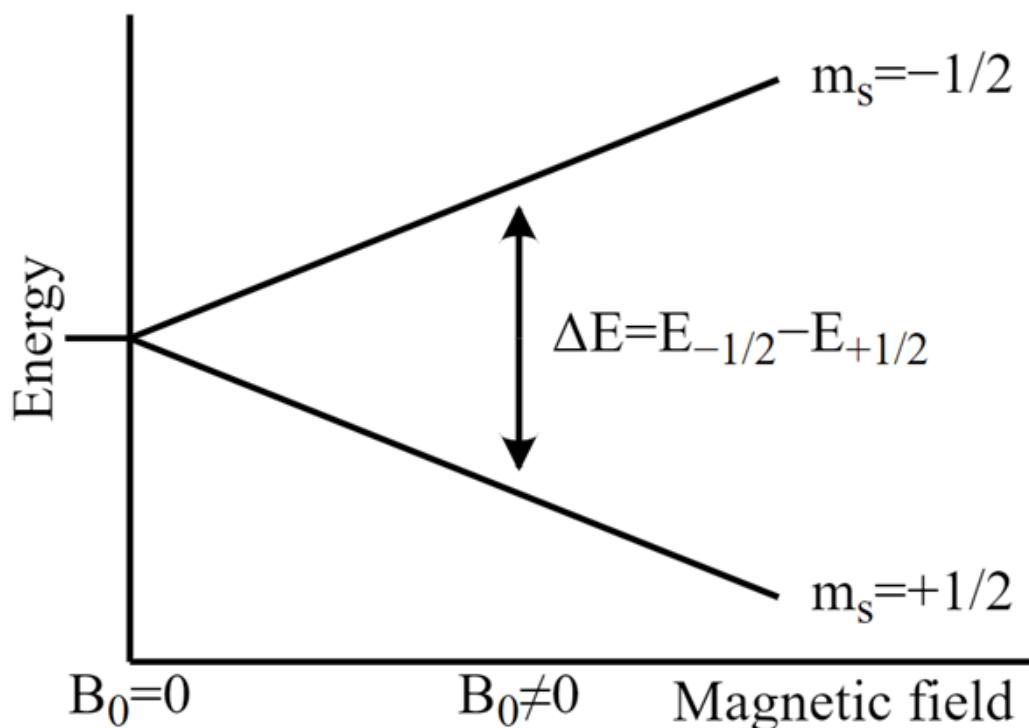
Fig. 3.4.1. Splitting of electron spin states in a magnetic field.

EPR technique is based on resonance absorption of microwave energy by the spin system. Every electron has a magnetic moment and spin quantum number $S=1/2$ with magnetic components $m_s=\pm 1/2$. In the absence of a magnetic field, the two spin states are degenerate. When an external magnetic field B_0 is applied, the degeneracy of the spin states is lifted and electron's magnetic moment align either parallel ($m_s=+1/2$) or antiparallel ($m_s=-1/2$) to the field (fig. 3.4.1), each alignment having specific energy due to the Zeeman effect [Eaton, 2010]:

$$E = m_s g_e \mu_B B_0 \qquad\qquad 3.4.1$$

here, g_e is electron's g-factor (for free electron $g_e = 2.0023$) and μ_B Bohr magneton, which is the natural unit of the electron's magnetic moment.

The separation between the lower and the upper state for unpaired free electrons is:

$$\Delta E = g_e \mu_B B_0 \qquad\qquad 3.4.2$$

Equation (3.4.2) implies that the splitting of the energy levels is directly proportional to the magnetic field's strength. Because the energy difference, ΔE, between the two spin states can be varied by changing the magnetic field strength, there are two potential approaches to obtaining spectra: a) the magnetic field could be held constant while the frequency of the electromagnetic radiation is scanned and b) the electromagnetic radiation frequency could be held constant while the magnetic field is scanned. Absorption of energy occurs when the magnetic field "tunes" the two spin states such that the energy difference matches the energy of the applied radiation. This field is called the resonance field. Because of difficulties in scanning microwave frequencies and because of the use of a resonant cavity for signal detection, most EPR spectrometers operate at constant microwave frequency and scan the magnetic field.

An unpaired electron can move between the two energy levels by absorbing or emitting a photon of energy $h\nu$ which is equal to ΔE. This leads to the main equation of EPR spectroscopy:

$$h\nu = g_e \mu_B B_0 \qquad\qquad 3.4.3$$

here, h is Planck constant and ν frequency of microwave field. Eq. 3.4.3 permits a large combination of frequency and magnetic field values, but the great majority of EPR

measurements are made with microwaves in the 9–10 GHz region, with resonance fields corresponding to about 3500 G (0.35 T).

The resonance fields for a $g = 2$ sample at various microwave frequencies are listed in Table 3.4.1.

Microwave band	Microwave frequency (GHz)	B_0 (for $g = 2$) gauss
L	1	390
S	3	1070
X	9	3380
K	24	8560
Q	35	12480
W	94	33600

Table 3.4.1 The field for resonance for a $g = 2$ sample at various microwave frequencies, adapted from Ref. [Eaton, 2010].

When magnetic field value satisfies Eq. 3.4.3, resonance absorption takes place (Fig. 3.4.2). Unfortunately, sometimes the signal/noise ratio is not sufficiently large to directly detect absorption signal. In such a case, magnetic field modulation with phase sensitive detection is a very useful technique to separate signal and noise.
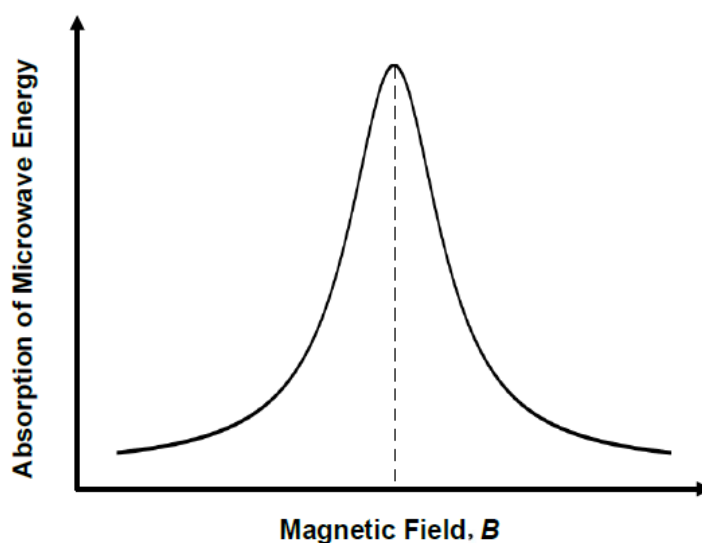

Fig. 3.4.2 A typical EPR absorption curve.

The microwave detector output from EPR absorption is very noisy at low frequencies, but the noise decreases with increasing frequency. EPR signal is shifted to a higher frequency by modulating sinusoidally with a frequency of 100 kHz and then demodulated in the signal channel to obtain the desired noise-suppressed and stable low frequency EPR signal.

If modulation is not used, the EPR signal has low frequency component and on the detector is dominate 1/frequency and not the EPR signal (Fig. 3.4.3 a). By using 100 kHz modulation field the EPR signal shifts to 100 kHz (Fig. 3.4.3 b), but the noise is not frequently shifted. After phase sensitive detection EPR signal is shifted to 0 and 200 kHz (Fig. 3.4.3 c) and 1/frequency is also shifted to 100 kHz. Finally, by using Resistor–Capacitor (RC) filter with a selectable time constant the unwanted 1/frequency noise and 200 kHz signal are filtered (Fig. 3.4.3 d).
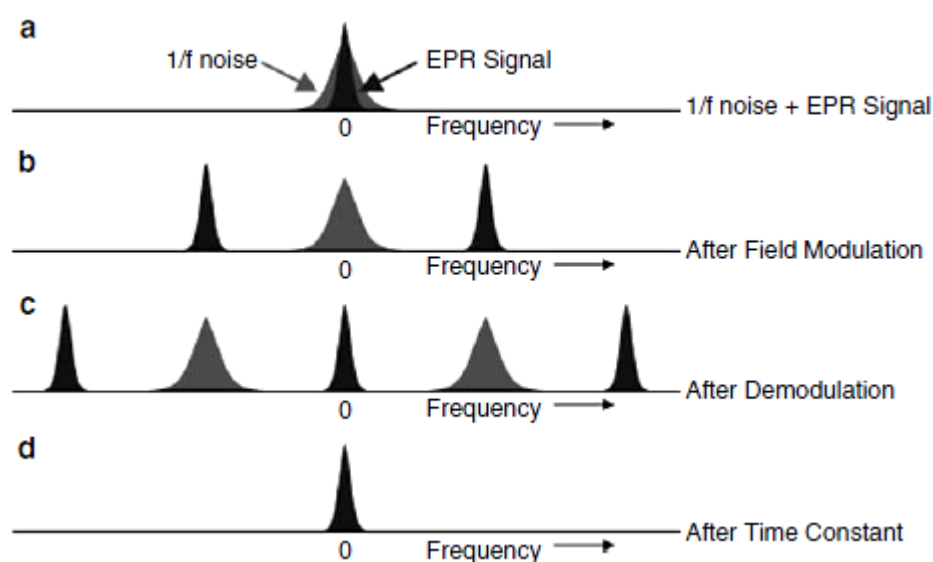

Fig. 3.4.3 The illustration of how field modulation and phase sensitive detection is realized in an EPR spectrometer, from [Eaton, 2010].

The EPR spectrum is usually directly measured as the first derivative of the absorption. This is accomplished by using phase sensitive detection. Figure 3.4.4 (left) shows the principle of phase-sensitive detection by magnetic field modulation.
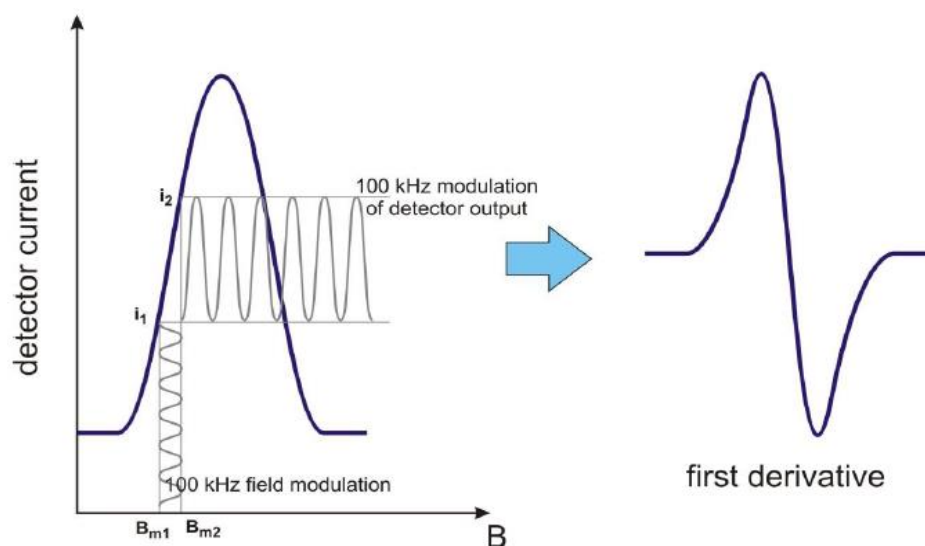
Fig. 3.4.4 The principle of phase-sensitive detection by magnetic field modulation, reproduced from Ref. [Eaton, 2010].

The main magnetic field is scanned slowly through the EPR line, a small additional oscillating magnetic field, B_m, is applied in the same direction as the main field, B. As B_m increases from the value B_{m1} to B_{m2}, the crystal detector output increases from i_1 to i_2. If the magnitude of B_m is small relative to line width, the detector current oscillating at 100 kHz has a peak-to-peak value that approximates the slope of the absorption curve. Consequently, the output of the phase-sensitive detector is the derivative of the absorption curve (Fig. 3.4.4 right). The relationship between the magnetic field modulated signal and the first derivative of the EPR absorption line is illustrated in Fig. 3.4.5.
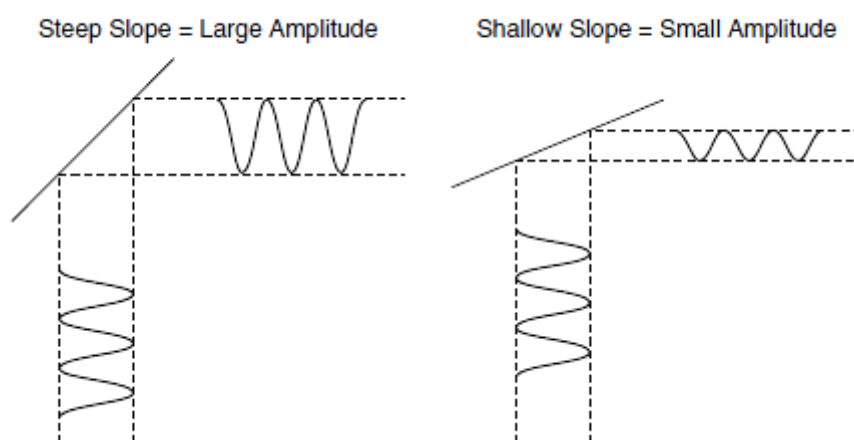

Fig. 3.4.5 Illustration of the relationship between the magnetic field modulated signal and the first derivative of the EPR absorption line, from [Eaton, 2010].

3.5 Ferromagnetic resonance

Ferromagnetic resonance (FMR) is the resonant absorption of electromagnetic radiation by the spin system of a ferromagnetic material. FMR is very similar to electron paramagnetic resonance (EPR) and also somewhat similar to nuclear magnetic resonance (NMR), except that FMR probes the sample magnetization resulting from the magnetic moments of dipolar-coupled but unpaired electrons, while NMR probes the magnetic moment of atomic nuclei that are screened by the atomic or molecular orbitals surrounding such nuclei of non-zero nuclear spin. FMR is a widely used technique for the characterization of ferromagnetic samples. Many important parameters of ferromagnetic state such as magnetization, magnetic anisotropy and magnetization dynamics can be obtained by the FMR method.

From a macroscopic point of view, the applied static magnetic field H_0 causes precession of the total magnetic moment around the direction of the local field, before relaxation processes damp this precession and the magnetization aligns with the effective field, $\vec{H}_{eff}$ (Fig. 3.5.1). The effective field is a combination of the external magnetic field, the demagnetizing field and some quantum mechanical effects.
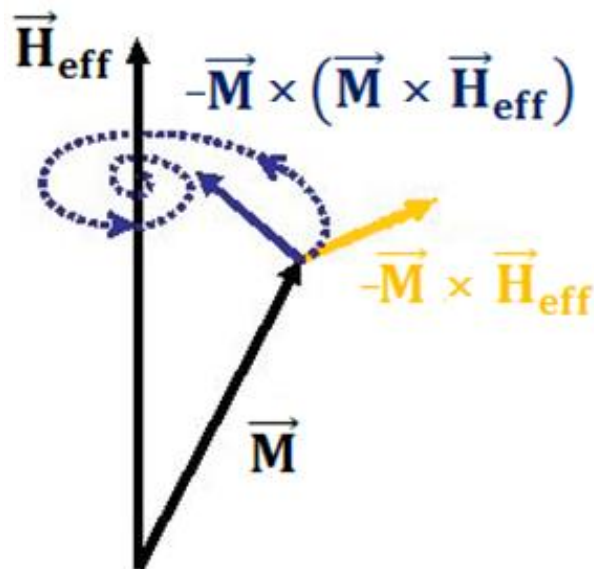

Fig. 3.5.1 The terms of the Landau–Lifshitz–Gilbert equation: precession (yellow) and damping (blue). The trajectory of the magnetization (dotted spiral) is drawn under the simplifying assumption that the effective field $\vec{H}_{eff}$ is constant.

If the sample is irradiated with an electromagnetic field in the microwave range (typically 1–35 GHz), and if this frequency coincides with the precession frequency, the resonance condition is fulfilled and the microwave power is absorbed by the sample. The motion of the magnetization is described by the Landau-Lifshitz-Gilbert equation:

$$\frac{\partial \vec{M}}{\partial t} = -\gamma(\vec{M} \times \vec{H}_{eff}) + \frac{G}{\gamma M_s^2}[\vec{M} \times \frac{\partial \vec{M}}{\partial t}] \qquad (3.5.1)$$

The first part of Eq. 3.5.1 corresponds to the precession. The second part introduces damping (Gilbert damping constant G). γ is the gyromagnetic ratio ($\gamma = g\mu_B/\hbar$). The effective magnetic field $\vec{H}_{eff}$ includes the applied DC field, the microwave magnetic field component, the demagnetizing field (shape anisotropy) and the magnetocrystalline anisotropy field. The classical equation of Landau-Lifshitz, without damping, is the following:

$$\frac{\partial \vec{M}}{\partial t} = -\gamma(\vec{M} \times \vec{H}_{eff}) \qquad (3.5.2)$$

The solution of the Landau-Lifshitz equation relates the resonant frequency (ω) to the total effective magnetic field:

$$\omega = \gamma \vec{H}_{eff} \qquad (3.5.3)$$

Eq. 3.5.3 shows that the resonance frequency of the magnetic materials depends on magnetic anisotropy. This means that the shape of the sample plays an important role, because the effective field depends on the demagnetization field. The resonance frequency for ellipsoid shape sample, with demagnetizing factors N_x, N_y, N_z, and with the static magnetic field in the z-direction is given by [Kittel, 1951]:

$$\omega_0 = \gamma\left([H_z + (N_x - N_z)M_z][H_z + (N_y - N_z)M_z]\right)^{\frac{1}{2}} \qquad (3.5.4)$$

The resonance frequency in a ferromagnetic single crystal depends on the angle between the magnetization vector and crystal axes, as a result of the magnetocrystalline anisotropy energy. For example, in the (001) plane of a cubic crystal:

$$\omega_0 = \gamma \left(\left[H_z + (N_x - N_z)M_z + \frac{2K_1}{M_z} cos4\theta \right] \left[H_z - (N_x - N_z)M_z + \frac{K_1}{M_z} (\frac{3}{2} + \frac{1}{2} cos4\theta) \right] \right)^{\frac{1}{2}} \quad (3.5.6)$$

In the (011) plane:

$$\omega_0 = \gamma \left(\left[H_z + (N_x - N_z)M_z + \frac{K_1}{M_z} (2 - \sin^2\theta - 3\sin^2 2\theta \right] \left[H_z - (N_y - N_z)M_z + \frac{2K_1}{M_z} (1 - \right. \right.$$

$$\left. \left. 2\sin^2 2\theta - \frac{3}{8}\sin^2 2\theta) \right] \right)^{\frac{1}{2}} \qquad (3.5.7)$$

In Eqs. 3.5.6 and 3.5.7, θ is the angle between [100] direction and z-axis. K_1 is the anisotropy constant. It must be noted that these equations are valid when the static field is sufficiently large that the magnetization (M) may be considered to be oriented approximately in the direction of the static field $(M_z \gg \frac{K}{M_z})$.

3.6 Novel microscopic method for the direct determination of the ME effect

In order to detect the magnetoelectric effect (ME) sensitive and reliable experimental techniques are required. Usually, for the determination of the ME coupling the electric polarization is measured as a function of the magnetic field or the magnetization is studied as a function of an applied electric field [Erenstein, 2006]. Also is one more method which is based on measurements of the temperature dependence of the dielectric permittivity [Bartkowska, 2015].

The novel microscopic method for the direct determination of the ME effect based on the standard Electron Paramagnetic/Ferromagnetic Resonance (EPR/FMR) technique combined with electric field modulation (EFM) method was developed by Georgian and Swiss researchers [Maisuradze, 2012]. In a standard EPR spectrometer, an external magnetic

field is swept and the resonance absorption of microwave energy by a Zeeman-split spin system is registered. In addition, to increase the sensitivity, the applied magnetic field H is modulated: $H = H' + H_m \sin(2\pi \nu_m t)$, where H_0 is the static applied magnetic field, H_m is the modulation amplitude, and ν_m is the modulation frequency. As a result, while sweeping the magnetic field H_0, the detected microwave absorption power $P(t) = P_m \sin(2\pi \nu_m t)$ is also modulated with the frequency ν_m. The amplitude P_m is proportional to the slope of the absorption signal $P(H)$ as illustrated in Fig. 3.6.1. Further amplification and lock-in detection of $P(t)$ results in the EPR derivative signal dP/dH. In the EFM EPR/FMR measurements an oscillating electric field instead of magnetic modulation is applied to detect the resonance absorption.
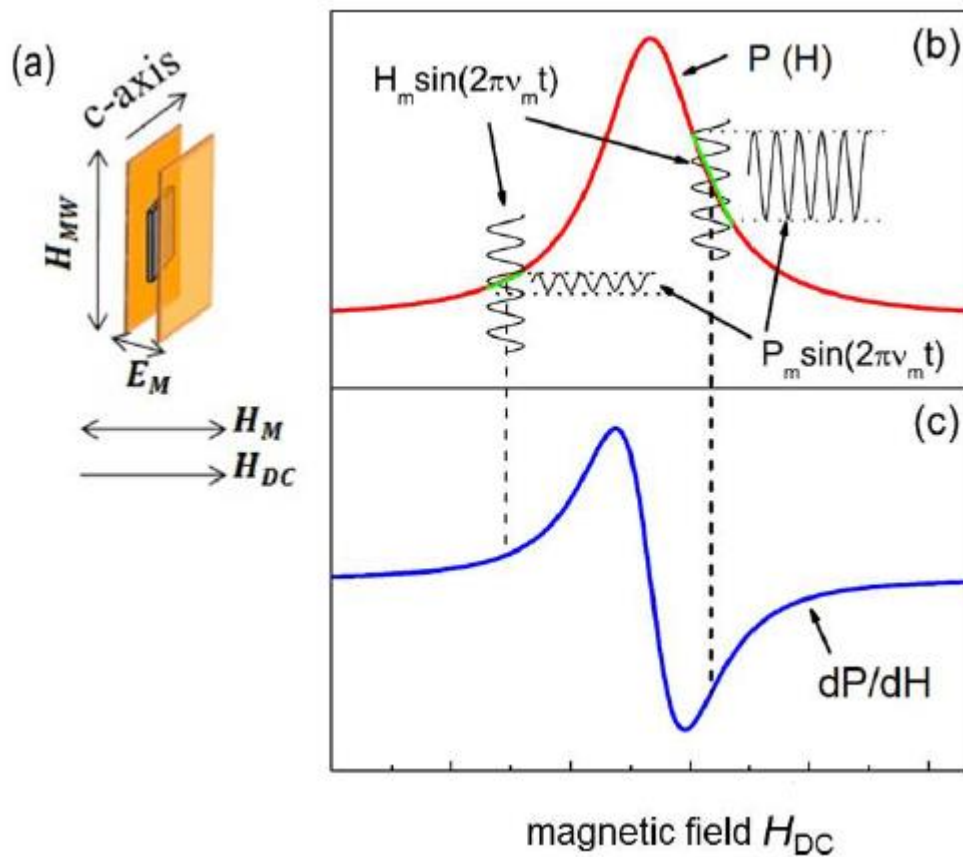

Fig. 3.6.1 a) Schematic view of the sample and the magnetic or electric field configuration, from [Maisuradze, 2012]. The sample is sandwiched between two copper plate electrodes. b) The basic principle of the EPR signal detection. The red curve represents the EPR absorption line $P(H)$. c) First derivative dP/dH signal of the EPR absorption line $P(H)$ after lock-in detection.

In a spin system without ME effect no modulated signal $P(t) = P_m \sin(2\pi v_m t)$ will occur. However, if the ME effect is present, modulation by an electric field $E(t)$ will lead to a modulation of the magnetic field in the sample $B(t)$. In this case, the EPR/FMR signal which is proportional to the ME coupling may be detected as was demonstrated in Fig. 3.6.2.
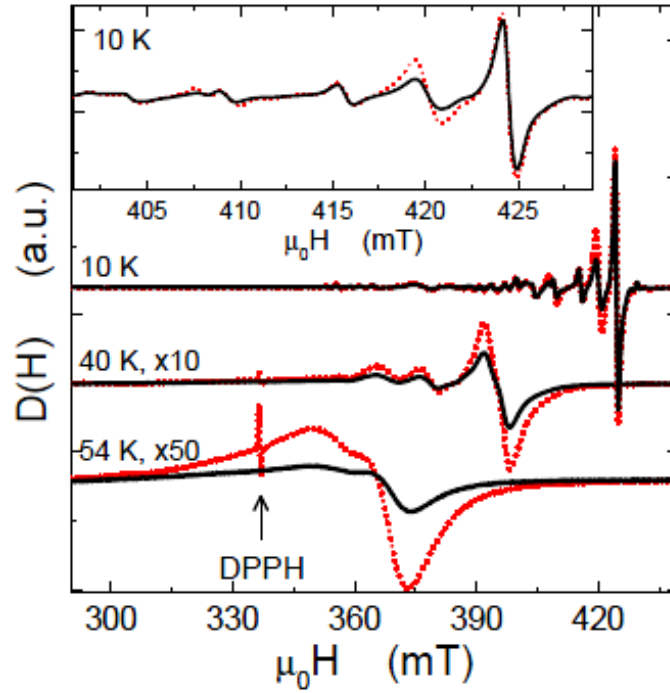

Fig. 3.6.2 Temperature dependence of signals of single-crystal Cu_2OSeO_3 compound detected using the MFM technique (dotted line) and the EFM technique (solid line). The sharp peak visible at 340 mT and 54 K is the signal of the marker sample DPPH which is present only in the case of MFM. The inset shows the expanded spectra at 10 K around 415 mT. Reproduced from Ref. [Maisuradze, 2012].

The ratio of the signal intensities detected by electric and magnetic modulations is proportional to the strength of the ME effect:

$$\alpha = \frac{I^{(EFM)}}{I^{MFM}} = \frac{\mu_0 H^i}{\mu_0 H_m} \qquad \qquad 3.6.1$$

here, I^{EFM} is signal intensity detected by electric field modulation and I^{MFM} with magnetic field modulation, $\mu_0 H_m$ is the field used in the MFM experiment and is equal to 1 mT, $\mu_0 H^i = \gamma E_m$ is the magnetic field induced by the electric field ($E_m = \frac{V}{d}$) and γ is the ME coupling strength. By using these notations the formula for calculation of the ME coupling strength can be obtained:

$$\gamma = \frac{I^{EFM}}{I^{MFM}} \times \frac{\mu_0 H_m}{V/d} \qquad\qquad (3.6.2)$$

3.7 Cold Neutron three axis spectrometer

The triple-axis spectrometer (Fig. 3.7.1) is the most widely used instrument in the study of materials with neutron scattering [Li, 2015]. The triple-axis spectrometer has three vertical rotation axes. The first, which rotates a monochromator, allows choosing a narrow band of neutron wavelengths provided by the neutron source. The spectrum of this band is centered at a wavelength, λ, defined by Bragg's law for the diffraction of radiation by a crystal:

$$n\lambda = 2d\sin(\theta) \qquad\qquad 3.7.1$$

here, d is the lattice spacing of the monochromator crystal, θ is the angle between incident beam and the crystallographic reflecting plane, also it is equal to the angle between reflected beam and the crystallographic plane and n is a positive integer. In the experiments θ cannot be determined directly, but 2θ is an experimentally measurable quantity. 2θ is the angle between transmitted and reflected beam (the angle through the neutrons are scattered) and is defined by two collimators which are located both sides of the monochromator sample. The second axis of rotation passes through the sample and allows for the investigation of the neutron scattering properties of the sample as a function of the scattering angle θ. The third axis passes through the analyzer crystal. The analyzer crystal defines the final energy.

One of the best three-axis spectrometers (IN-12) for cold neutrons (0.0 – 0.025 eV) operates at the Institut-Laue Langevin in Grenoble, France. This spectrometer is developed for the elastic and inelastic studies of low energy structural and magnetic excitations. The

monochromator of IN-12 is a set of horizontally and vertically focusing pyrolytic graphite (002) crystals, which delivers the incident wavelengths (1.26 Å < λ < 6.3 Å), energies (2.1 meV < E_i < 42 meV) and wavevectors 1.0 Å^{-1} < k_i < 5.0 Å^{-1}. The monochromator can cover an angular range of -10°< $2\theta_M$ < 140°. The sample is mounted on a motorized non-magnetic goniometer which may achieve tilts of ± 20° and covers an angular range of -120° < $2\theta_s$ < 120°. The spectrometer has two analysers: PG (002) for unpolarized work and a Heusler (111) for polarization analysis. The analyzers covers an angular range of -140° < $2\theta_A$ < 140°.
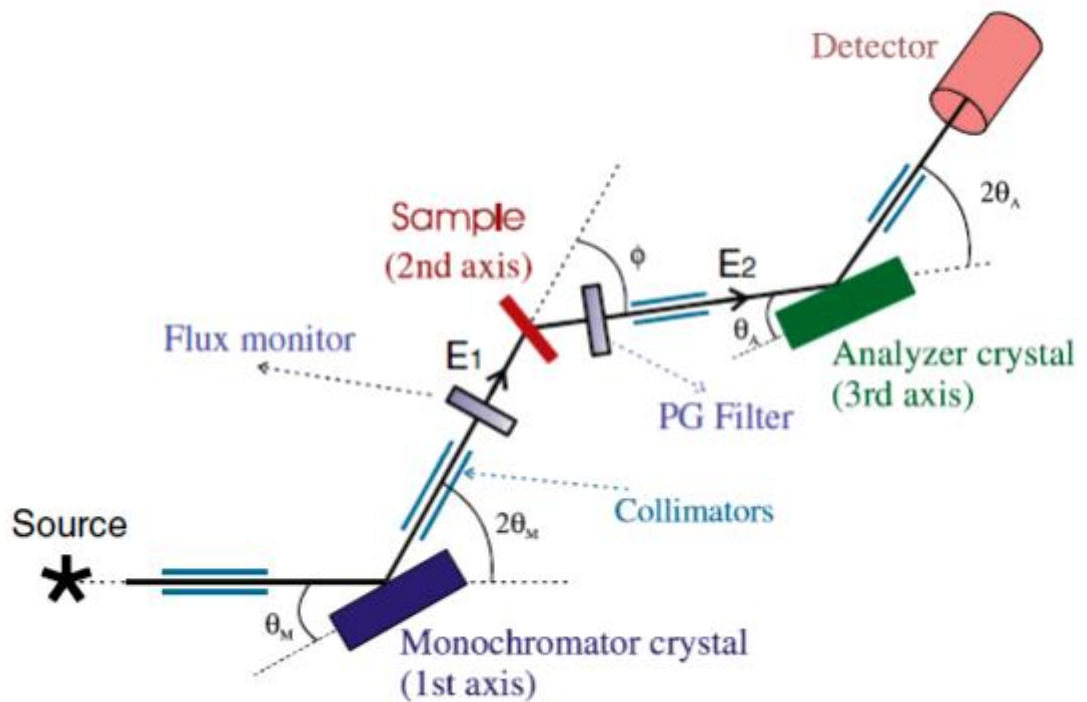

Fig. 3.7.1 Schematic drawing of the triple-axis spectrometer, from [Yamani, 2010]. The monochromator crystal at the first axis selects neutrons with specific energy, providing a monochromatic beam. The monochromated beam is shone onto the sample (2nd axis) where it interacts with the sample via both nuclear and magnetic interactions. The analyzer crystal at the third axis defines the final energy.

For use with the polarized neutrons a supermirror bender can be mounted after the first collimator to polarize the incident beam. The small field (< 15 Oe) may be imposed at the sample position using a system of coils or the superconducting magnet can be used to produce the large magnetic fields.

The neutrons have a nuclear magnetic moment. Therefore the scattering from a sample which exhibits magnetism will be sensitive to the properties of the sample. The scattering is also a function of the nuclear positions and motions. In case of, if the resonance produced by the magnetic properties of the sample is well separated from that produced by the nuclear scattering, no further effort is required. However, if there is required identification of the resonances as arising from a magnetic source, polarized neutrons beam is needed. In this case, the scattering law can then be measured as a function of whether the spin of the neutrons is reversed or not in the scattering. Such a spin flip can only be produced by magnetic interactions. These types of measurements are capable to find out which part of the scattering belongs to the magnetic properties of the sample and which one to the nuclear scatterings.

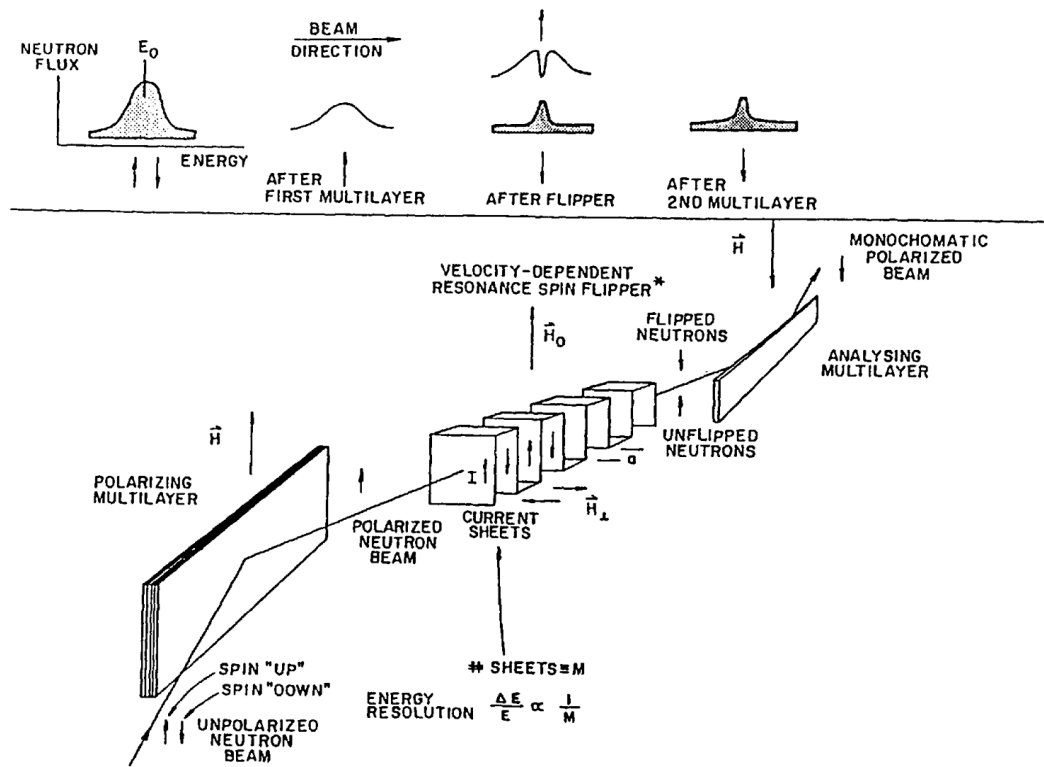Fig. 3.7.2 Schematic view of the neutron spin-flipper device, from [Trevino, 1992].

The polarized neutrons can be produced by using magnetic monochromator crystals. The scattering of the neutrons is strongly dependent on the relative orientation of the neutron magnetic moment and a magnetic field, extending from the monochromator to the sample. Figure 3.7.2 shows the schematic view of the neutron spin-flipper device which was

proposed by G.M Drabkin [Trevino, 1992]. The principle is the following: The unpolarized beam with a relatively broad energy bandwidth is first polarized by a supermirror. Afterwards, the beam crosses a current carrying foil, in such a form, that produces a small spatially oscillating magnetic field ($H^\perp$) which is perpendicular to both the propagation direction of the beam and a larger uniform magnetic field (H_0) that is superimposed over the full extent of the foil. Eq. 3.7.2 relates these two fields in the following way:

$$H^\perp = 2H_0/M \hspace{8cm} 3.7.2$$

here, M is the number of spaces between adjacent current sheets through the neutrons pass. Then, the resultant magnetic field acts as a velocity or energy selective resonance flipper. Neutrons only with velocities close to $v_0 = a\gamma H_0/\pi$ (γ is gyromagnetic ratio of the neutron and „a" spacing between adjacent sheets of the foil) can pass the spin-flip. The probability distribution as a function of velocity is centered at velocity v_0 and has a width proportional to $1/M$. Finally, those neutrons which are not flipped are subsequently not reflected by a second supermirror in which the magnetization direction is opposite to that of the first. Thus, the pair of supermirrors and the flipper act as the energy dependent filter whose characteristics are controlled electrically.

4 Experimental results and discussion

4.1 Single-crystal growth and sample preparation results

In this work, we have used flux growth technique for synthesizing single-crystal of Y-type $Ba_{0.6}Sr_{1.4}Zn_2Fe_{12}O_{22}$ hexaferrite, similar to described in section 3.1.1. High purity starting materials $BaCO_3$, $SrCO_3$, ZnO and Fe_2O_3 were used (see the composition of starting materials in Table 4.1). Na_2CO_3 was used as a solvent. The starting materials were mixed properly by grinding in a ball milling machine for 12 hours. The final mixture of these materials was packed into the high purity platinum (99.9997%) crucible and heated up to 1380^0 C. After, holding 10 hours at 1380^0 C temperature slow cooling with temperature oscillation was carried out. Temperature oscillation was used to avoid the formation of spinel phase.

$BaCO_3$	$SrCO_3$	ZnO	Fe_2O_3	Na_2CO_3

3.938	15.752	19.69	53.61	7.01

Table 4.1. Composition of starting materials used for crystal growth (composition in mole %).

Single crystals were formed at different places of the crucible, ranging from the center to the side walls. Therefore, nucleation centres can be considered to be on the walls of the crucible. While using a crucible of Pt alloy, it was found that the flux overflows through the wall of the crucibles. This could be due to higher affinity of the flux to stick to the walls and then overflow due to capillary action. We obtained single crystals of Y-type with various sizes. Most of the crystals were plate like and the biggest one was found to be 10mm × 8mm × 2mm (see Fig. 4.1). Nitric acid (HNO_3) was used to get the crystals out of the crucible.
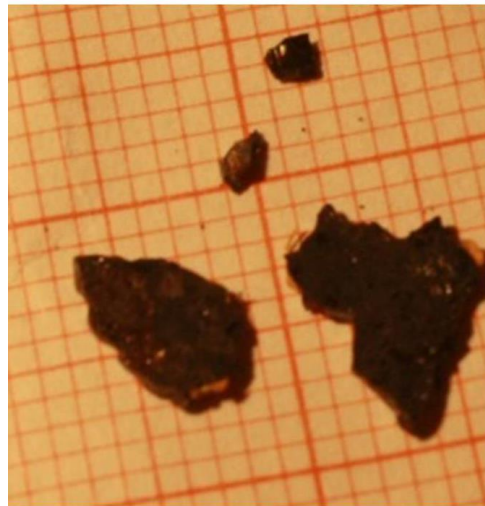

Fig. 4.1. Single crystals of Y-type $Ba_{1-x}Sr_{1.4}Zn_2Fe_{12}O_{22}$ hexaferrites.

4.2 Single crystal X-ray diffraction

After the synthesis of the crystals, primary characterization was performed for phase purity and crystal structures were determined. Single crystals were characterized by single-crystal X-ray diffraction measurements at room temperature on a Rigaku supernova single crystal diffractometer, using MoKα radiation. The lattice parameters were found to be a=b=5.85 Å and c=43.42Å in ($R\bar{3}m$) space group with hexagonal setting. Structure refinement of the structure was performed using JANA2006 [Petricek, 2014]. From the previous refinement studies it was found that Zn atoms are located in two tetrahedral sites [Collomb, 1989; Muller, 1991]. Therefore, we restricted Zn in our refinement to only 6c tetrahedral sites.

From the refinement of single crystal X-ray diffraction data, chemical composition of the crystal and partial occupancies of the Zn and Fe sites were determined (see Table 4.2.1). The partial occupancies of the Zn sites are close to those found in previous studies [Muller, 1991]. The Sr content (x) determined in a single crystal is slightly different from that of the starting reactant mixture. Such differences are often observed in complex hexaferrites and were reported before [Momozawa, 1986]. Therefore, for the accurate determination of (x), we need to depend upon the composition from refinement rather than predicting it from the composition initially used in the reactant mixture. Inconsistencies, in the value of (x), may arise with results from other studies also. Therefore, we compared the values from only those previous studies where compositions were taken from refined data of scattering studies.

Stoichiometric formula	Zn(1)	Fe(1)	Zn(2)	Fe(2)
$Ba_{0.58}Sr_{1.42}Zn_{1.66}Fe_{12.28}O_{22}$	0.14	0.84	0.68	0.31

Table 4.2.1 Chemical composition and partial occupancies of the Zn and Fe sites obtained from single crystal X-ray diffraction refinements.

Magnetic structures of $(Ba_{1-x}Sr_x)_2Zn_2Fe_{12}O_{22}$ depending upon (x), were studied by Utsumi [Utsumi, 2007]. A unit cell contains 6 different types of Fe atoms as shown in Table 4.2.2. Zn^{2+} ions are restricted in two tetrahedral sites with Wyckoff position (6c) in our refinement. A variable γ is defined where, occupation of $Zn(1)$ is γ and that of $Zn(2)$ is (1–γ), however, total occupation of Zn^{2+} does not add up to 2 in stoichiometric formula for different values of x [Collomb, 1989; Muller, 1991]. In the earlier studies, no clear trend was

observed for Zn with (x). Therefore, with only three compositions it is difficult to find a conclusive fitting for Zn with (x). The difference between the electrons content in Zn^{2+} and Fe^{3+} is just 6 electrons, so with X-rays which are sensitive to the number of electrons, it is difficult to precisely determine (γ). Partial occupancies of $Zn(1)$ and $Zn(2)$ are graphically shown in Fig. 4.2 a. The occupancies of $Zn(1)$ increase with increasing (x) and $Zn(2)$ decrease. The sum occupancies of $Zn(1)$ and $Zn(2)$ are less than unity. That is why in the overall composition is less Zn than the nominal stoichiometry. Earlier refinements also reported similar results [Collomb, 1989; Muller, 1991].

Atom (label)	Wyckoff positions	Structural block	Magnetic block	spin	C_{Fe}	Coordination
$Fe(1)$ $(Zn(1))$	$6c$	T	μ_S	↑	γ	Td
$Fe(2)$ $(Zn(2))$	$6c$	S	μ_L	↑	$1 - \gamma$	Td
$Fe(3)$	$6c$	T	μ_L	↑	1	Oh
$Fe(4)$	$3b$	S	μ_L	↓	1	Oh
$Fe(5)$	$18h$	T,S	μ_L	↓	1	Oh
$Fe(6)$	$3a$	T	μ_S	↓	1	Oh

Table 4.2.2 Different types of Fe^{3+}/Zn^{2+} in unit cell of Ba2Zn2Fe12O22.

The bond length of all the transition metal-O bonds was calculated from the refinement. $Zn(1) - O(1)$ bond length is shortest in the range of 1.9 Å. $Fe(3) - O(3)$ has the longest bond length ($\approx$ 2.25 Å) compared to other average bond lengths of $\approx$ 2 Å. The bond lengths can be seen in Fig. 4.2 b) and its values are given in Table 4.2.3.
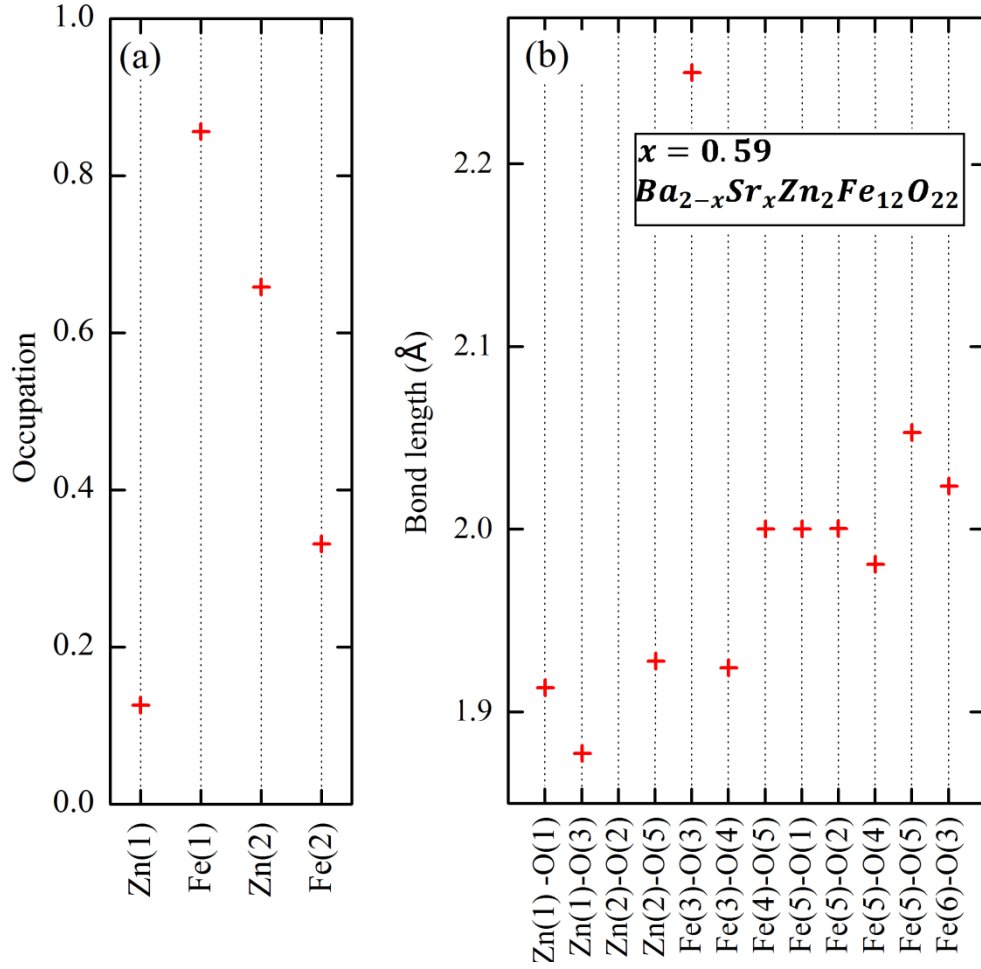
Fig. 4.2: a) Partial occupancies of $Zn(1)$ and $Zn(2)$ for Y-type hexafferite and (b) different $Fe/Zn-O$ bond lengths. x is given in the formula $Ba_{1-x}Sr_xZn_2Fe_{12}O_{22}$.

According to Momozawa et al. [Momozawa, 1985] there are three types of magnetic ordering depending upon the Sr content in the crystals of $Ba_{1-x}Sr_xZn_2Fe_{12}O_{22}$: ferrimagnetic ordering for $0 \leq x \leq 0.5$, helical magnetic ordering for $0.5 \leq x \leq 0.8$ and collinear ordering for $0.8 \leq x \leq 1$. From our samples we have (x) value in the helical range. We used magnetization measurements on the sample $Ba_{0.6}Sr_{1.4}Zn_2Fe_{12}O_{22}$ to find out if it displays the signature metamagnetic features reported [Momozawa, 1985].

Bond type	$x = 0.59$
$Zn(1) - O(1)$	1.913
$Zn(1) - O(3)$	1.877
$Zn(2) - O(2)$	1.98
$Zn(2) - O(5)$	1.928
$Fe(3) - O(3)$	2.251
$Fe(3) - O(4)$	1.925
$Fe(4) - O(5)$	2
$Fe(5) - O(1)$	1.999
$Fe(5) - O(2)$	2
$Fe(5) - O(4)$	1.981
$Fe(5) - O(5)$	2.054
$Fe(6) - O(5)$	2.023

Table 4.2.3. Different transition metal-O bond lengths from single crystal X-ray refinements of Y-type $Ba_{1-x}Sr_{1.4}Zn_2Fe_{12}O_{22}$ hexaferrite sample at room temperature. (x) is given in the formula: $Ba_{1-x}Sr_{1.4}Zn_2Fe_{12}O_{22}$.

4.3 Magnetic studies

Measurements of magnetic hysteresis loops and the temperature dependence of magnetization were performed using the Physical Property Measurement System equipped with VSM (Quantum Design PPMS and DynaCool).

We put the sample in the PPMS magnetometer, that the applied magnetic field was perpendicular to the c-axis. Fig. 4.3.1 shows the temperature dependence of the magnetization in $Ba_{0.6}Sr_{1.4}Zn_2Fe_{12}O_{22}$ single crystal at H=100 Oe under zero-field cooling (ZFC) and field-cooling (FC) mode (applied magnetic field was perpendicular to the c-axis). It was observed that there is no difference between ZFC and FC curves. A pronounced peak of magnetization was observed at 331 K, as can be seen in Fig. 4.3.1. Such a peak was observed previously in Y-type hexaferrites and was attributed either to ferrimagnetic transition [Kimura, 2005; Kamba, 2010] or to a transition from a collinear ferrimagnetic spin

phase to a proper screw spin phase with decreasing temperature [Zhang, 2016]. In our magnetometer maximum available temperature was 380 K, which is not sufficient to reach the paramagnetic state. However, we could determine the transition temperature from FMR measurements (discussed in section 4.4), which showed that the transition from paramagnetic to ferrimagnetic state starts below 400 K. Therefore we conclude that the magnetization peak observed at 331 K in the $Ba_{0.6}Sr_{1.4}Zn_2Fe_{12}O_{22}$ single crystal is not due to ferrimagnetic transition, but it is related to a transition from a collinear ferrimagnetic phase to a proper screw spin phase.

At low temperatures two additional small peaks of magnetization were observed at T=80 K and 20 K as shown in Fig. 1. A similar peak at around 25 K was reported before in polycrystalline samples of $Ba_{0.5}Sr_{1.5}Zn_2(Fe_{0.96}Al_{0.04})_{12}O_{22}$ and was attributed to a magnetic transition from longitudinal proper screw spin to conical spin phase [Wenfei, 2014]. The small peak at 80 K was not observed before to the best of our knowledge in Y-type hexaferrites and its origin is not clear at present.
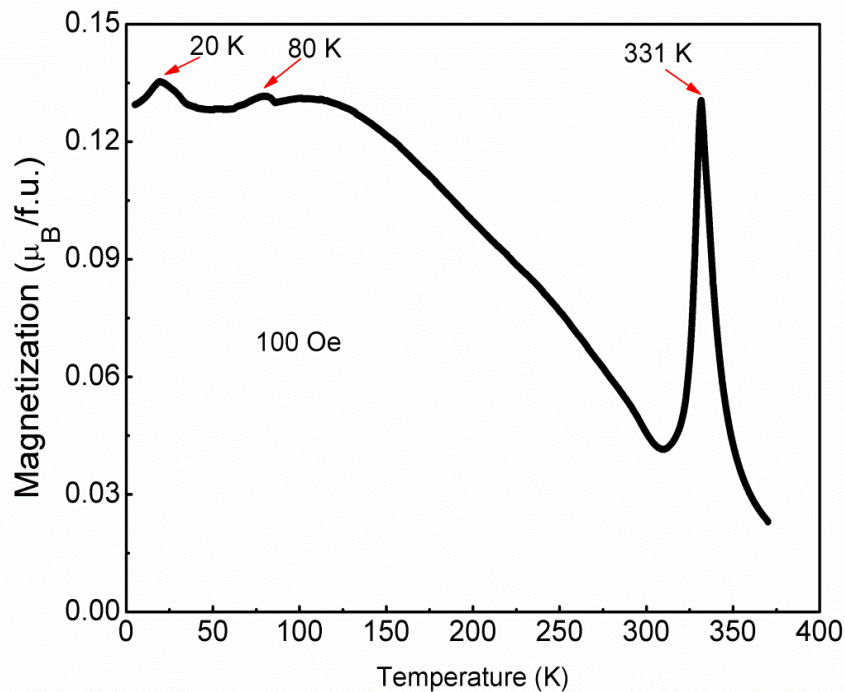

Fig. 4.3.1. Temperature dependence of the ZFC and FC magnetization in a field of 100 Oe ($H \perp c$) for the single crystal of the $Ba_{0.6}Sr_{1.4}Zn_2Fe_{12}O_{22}$ hexaferrite.

Fig. 4.3.2 shows magnetic hysteresis loops at two temperatures T=50 K and 300 K. Magnetic field up to 6 Tesla was applied perpendicular to the *c*-axis, which is identical to the helical plane. Inset of the Fig. 4.3.2 shows zoomed view of *M*(*H*) dependence in low magnetic fields. The obtained coercivity field in $Ba_{0.6}Sr_{1.4}Zn_2Fe_{12}O_{22}$ single crystal is quite small and equals to 15 and 20 Oe at 50 and 300 K, respectively.
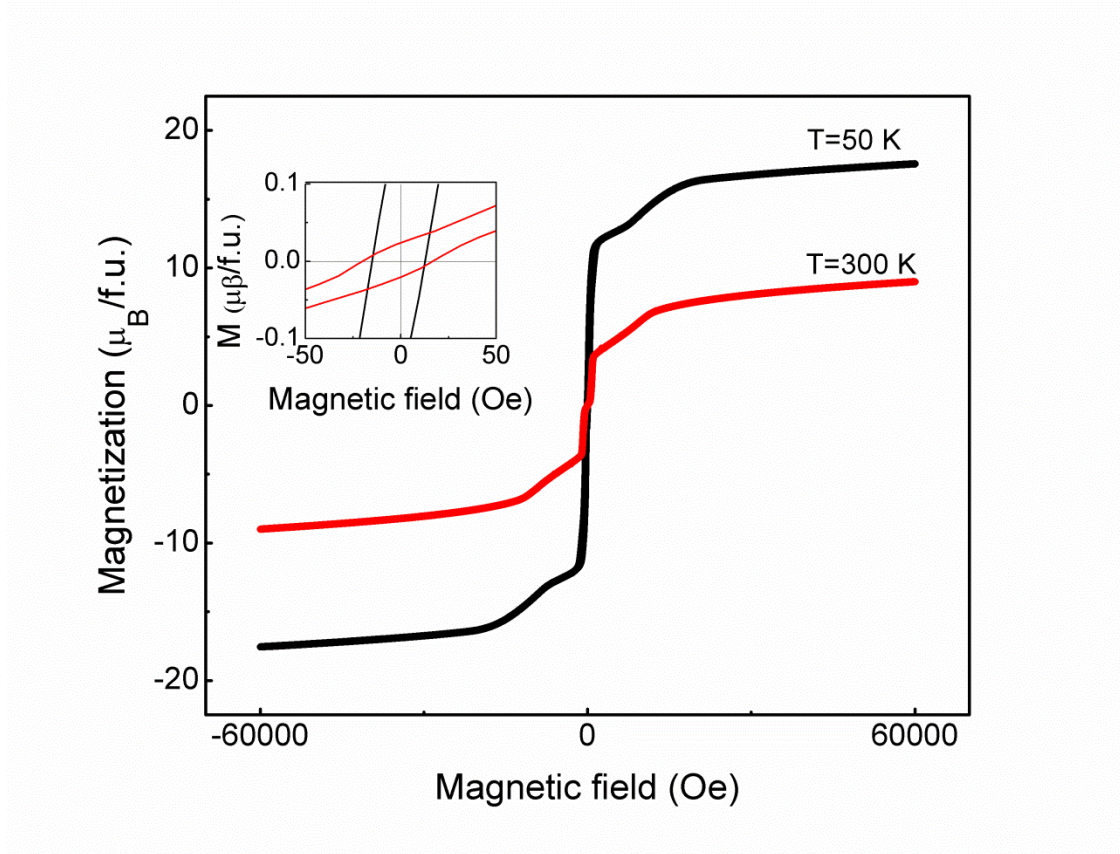

Fig. 4.3.2 Hysteresis loops measured at 50 K and 300 K of $Ba_{0.6}Sr_{1.4}Zn_2Fe_{12}O_{22}$ hexaferrite single crystal (*H*⊥*c*). The inset shows a zoomed view of *M*(*H*) dependence in low magnetic fields.

One can see from Fig. 4.3.2 that *M*(*H*) curves in $Ba_{0.6}Sr_{1.4}Zn_2Fe_{12}O_{22}$ have unusual shape different from typical ferrimagnetic compounds. This confirms that at least up to 300 K in low fields the sample is not in a simple collinear ferrimagnetic state. With increasing magnetic field magnetization increases stepwise with several kinks before reaching saturation value. In order to see more clearly this behavior, we plotted the magnetic field dependence of the initial magnetization (see Fig.4.2.3). Inset of Fig. 4.2.3 shows zoomed view of *M*(*H*) dependence in low magnetic fields at 300 K. Such a behavior was observed for the

first time by Momozava *et al.* [Momozawa, 1985]. From data presented in Fig. 4.2.3 four characteristic magnetic fields $H_{c1}-H_f$ can be identified as was reported previously in the Y-type hexaferrite with similar composition [Momozawa, 1985]. Obtained values of $H_{c1}-H_f$ are listed in Table 4.3.1.
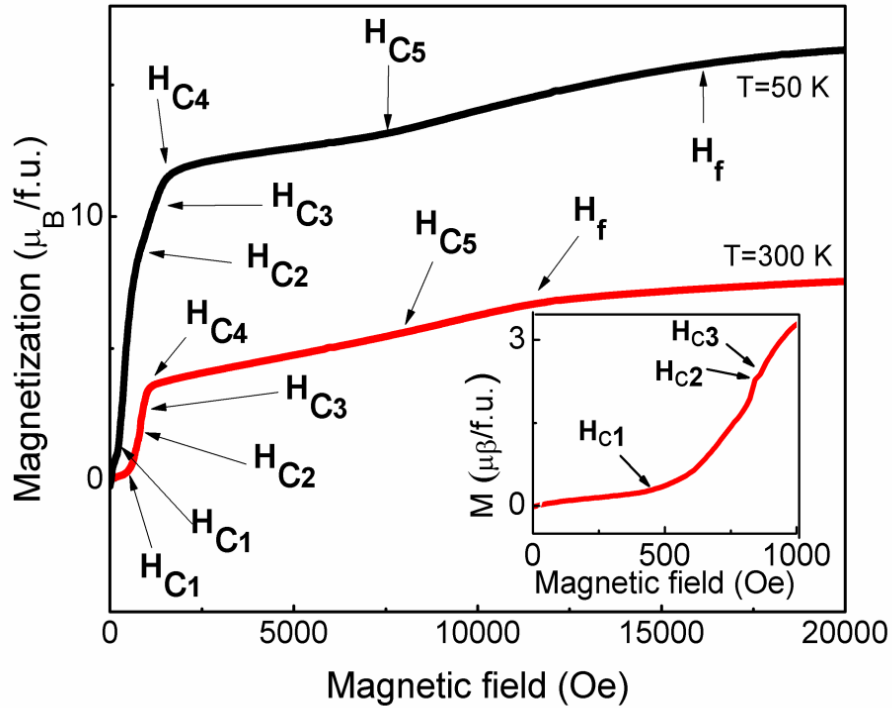

Fig.4.2.3 Magnetic field ($H\perp c$ axis) dependence of the initial magnetization measured at T=50 K and 300 K for the $Ba_{0.6}Sr_{1.4}Zn_2Fe_{12}O_{22}$ hexaferrite single crystal. The inset shows a zoomed view of $M(H)$ dependence in low magnetic fields at 300 K.

According to literature, reason for the stepwise behavior of the initial magnetization curves in Y- type hexaferrites is related to sequential metamagnetic transitions from helimagnetic to collinear ferrimagnetic phase with 3 intermediate phase transitions [Kimura, 2005; Momozawa, 1985].

T(K)	50	300
H_{c1}	0.2	0.4
H_{c2}	0.7	0.7

H_{c3}	0.9	0.8
H_{c4}	1.6	1.1
H_{c5}	7.2	7.1
H_f	16.2	12.1

Table 4.3.1 Characteristic magnetic phase transition fields H_{c1}-H_f determined from Figure 3 are shown in kOe.

4.4 FMR measurements

We performed FMR measurements in order to further investigate microscopic magnetic and magnetoelectric properties of $Ba_{0.6}Sr_{1.4}Zn_2Fe_{12}O_{22}$ hexaferrite single crystal. It was observed that this sample has a very strong FMR signal which we studied in a broad temperature range 160-450 K. Fig. 4.4.1 displays temperature dependence of the resonance field in $Ba_{0.6}Sr_{1.4}Zn_2Fe_{12}O_{22}$.
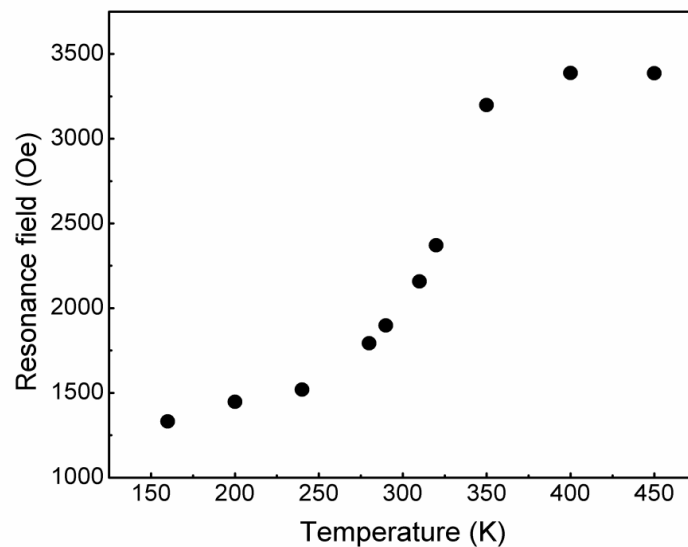

Fig. 4.4.1. Temperature dependence of the resonance field of $Ba_{0.6}Sr_{1.4}Zn_2Fe_{12}O_{22}$ hexaferrite single crystal with magnetic field parallel to crystal plane ($\theta=0^0$).

The resonance magnetic field is constant above 400 K as expected in the paramagnetic state. Below 400 K resonance field starts to decrease. This indicates that due to magnetic order an

internal magnetic field builds up in the sample and adds to the external magnetic field. As a result, resonance can be observed in smaller applied magnetic fields. Based on these results we can conclude that in $Ba_{0.6}Sr_{1.4}Zn_2Fe_{12}O_{22}$ the transition from paramagnetic to ferrimagnetic state takes place below 400 K.

This conclusion is also supported by the temperature dependence of magnetic resonance intensity, which is shown in figure 4.4.2. Below 350 K there is a strong increase of signal intensity. In contrast to EPR, FMR is the resonance of the total magnetization of the magnetically ordered sample. Therefore the strong increase of the resonance intensity is expected below the transition from para- to ferro/ferri-magnetic state.
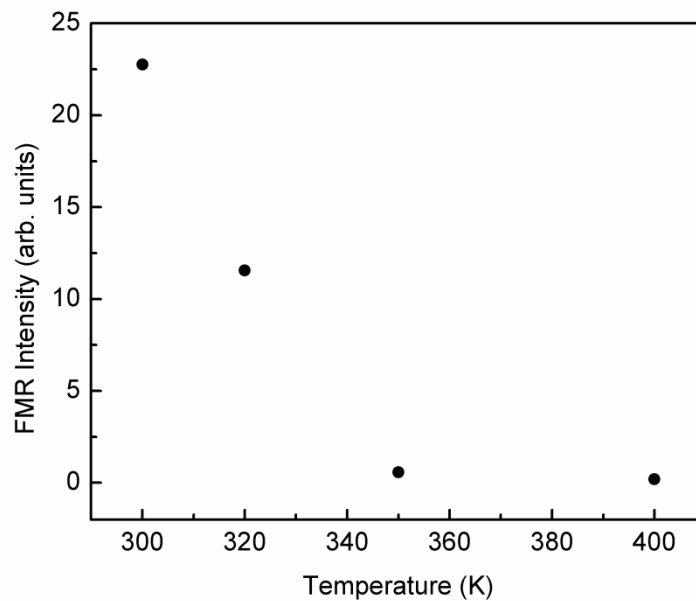

Figure 4.4.2. Temperature dependence of FMR signal intensity in $Ba_{0.6}Sr_{1.4}Zn_2Fe_{12}O_{22}$.

The FMR spectra were measured with the external magnetic field rotated out-of-plane and magnetic field was applied at an angle θ relative to crystal plane (see inset of Fig. 4.4.3 (a)). Figure 4.4.3 shows FMR spectra measured at room temperature with orientation of the static magnetic field parallel and perpendicular to crystal plane ($\theta=0^0$ and $\theta=90^0$). Small oscillations visible on the low field side of FMR signal in parallel orientation ($\theta=0^0$) are probably due to spin wave resonances. In this orientation the resonance field has also lowest value which indicates that the easy plane of magnetization is in the crystal plane, perpendicular to the c-axis direction. By approaching perpendicular orientation of the

magnetic field (θ=90^0) FMR line broadens significantly and the linewidth is very large at θ=90^0 as shown in Fig. 4.4.3 (b).
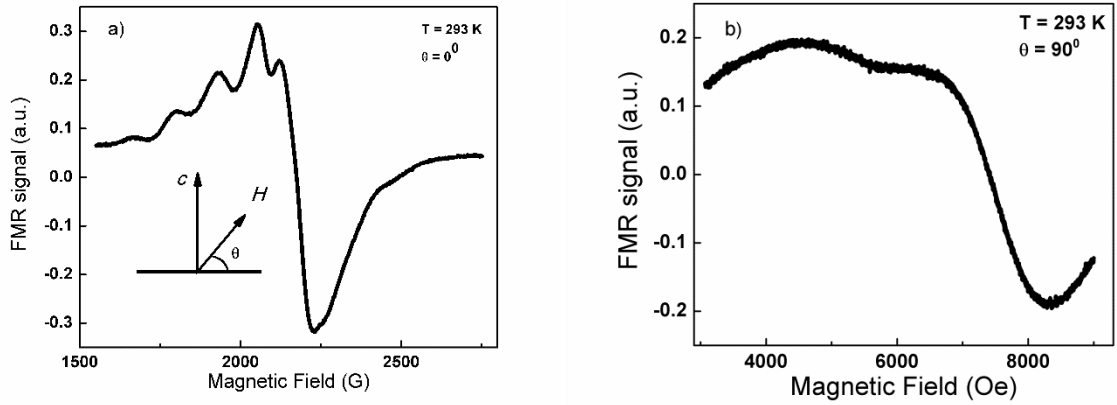

Fig. 4.4.3 FMR spectra at room temperature with different orientations of the static magnetic field, (a) parallel (θ=0^0) and (b) perpendicular (θ=90^0) to crystal plane for the Ba$_{0.6}$Sr$_{1.4}$Zn$_2$Fe$_{12}$O$_{22}$ hexaferrite single crystal. The inset of Fig. 4.4.3 (a) shows the geometry used for FMR measurements.

Angular dependence of FMR resonance field in Ba$_{0.6}$Sr$_{1.4}$Zn$_2$Fe$_{12}$O$_{22}$ at room temperature is presented in Fig. 4.4.4. In hexaferrite crystals for the case where the c-axis is along the z-axis and the easy plane of magnetization (crystal plane) is in the x-y plane so that the demagnetizing factors $N_x = N_y = 0$ and $N_z = 1$, one can write down following equations [Dorsey, 1990]:

$$\left(\frac{\omega}{\gamma}\right)^2 = H_\parallel (H_\parallel + H_{ss} + M_s) \qquad (4.4.1)$$

$$\left(\frac{\omega}{\gamma}\right) = H_\perp - H_{ss} - M_s \qquad (4.4.2)$$

Here $H_\parallel$ and $H_\perp$ are the resonance magnetic fields parallel and perpendicular to crystal plane, $\omega/2\pi$ is the spectrometer frequency, $\gamma = g\mu_B/\hbar$ is the gyromagnetic ratio, M_s is the saturation magnetization. Since helicoidal magnetic order is present in the Ba$_{0.6}$Sr$_{1.4}$Zn$_2$Fe$_{12}$O$_{22}$ hexaferrite, in Eqs. (4.4.1) and (4.4.2), usual uniaxial anisotropy magnetic field H_s is replaced with a spin spiral anisotropy magnetic field H_{ss} [Vittoria, 2015]. Taking

M_s =2010 Oe determined from magnetization measurements and by solving Eqs. (4.4.1) and (4.4.2), the values H_{ss} =1780 Oe and $g = 1.86$ were obtained. Observed deviation of the g-factor from pure spin value of $g=2$ indicates the presence of orbital contribution.
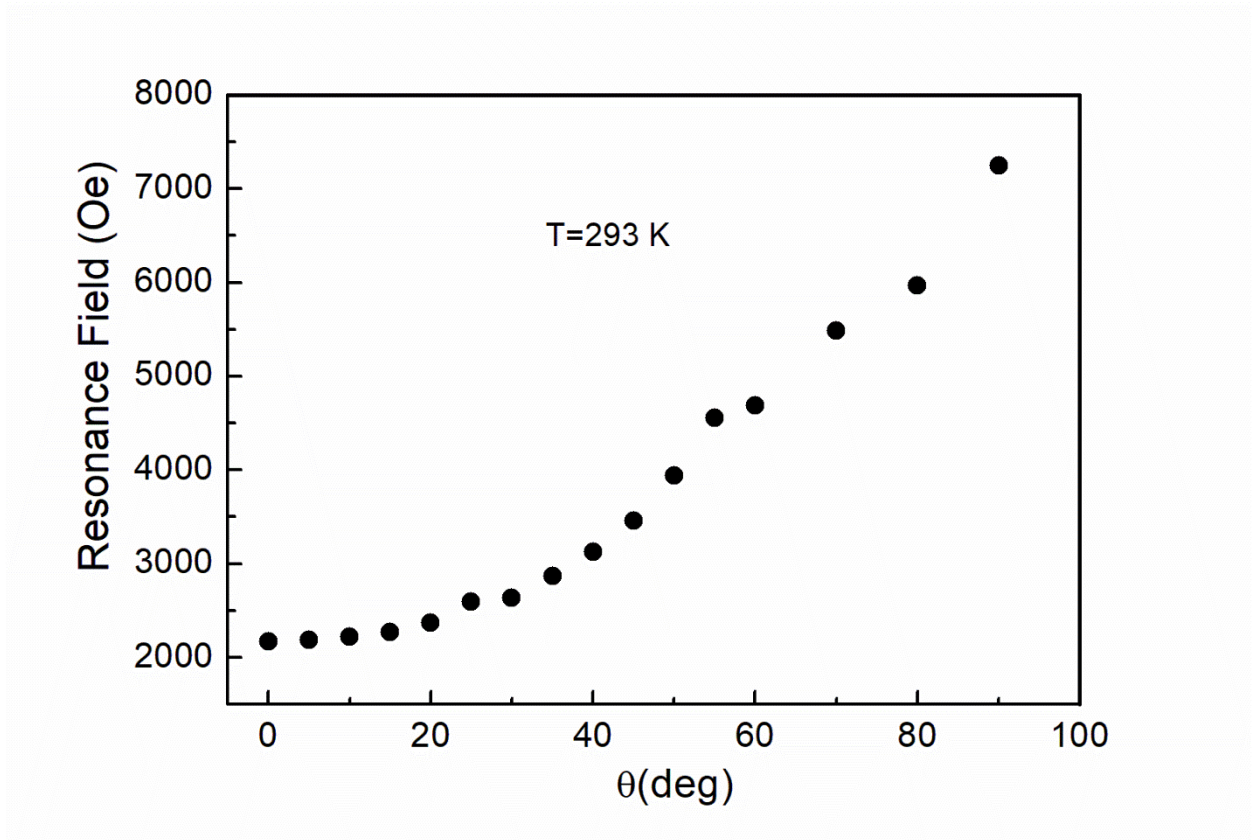

Fig. 4.4.4. Angular dependence of FMR resonance field at room temperature for the $Ba_{0.6}Sr_{1.4}Zn_2Fe_{12}O_{22}$ hexaferrite single crystal.

4.5 Magnetoelectric effect

In order to detect the ME effect, the single crystal of dimensions 1 mm x 1 mm x 0.02 mm was wrapped in a Scotch tape and placed in a capacitor-like structure between two copper electrodes. AC voltage of frequency 100 kHz from magnetic field modulation unit of the spectrometer after amplification to the necessary amplitude V_m was applied to electrodes. Experiments were performed in two steps. First usual FMR signals were detected using magnetic modulation. Afterwards magnetic modulation cable was removed from the cavity and an AC voltage of a frequency of 100 kHz from the magnetic field modulation unit of the

spectrometer after amplification to the necessary amplitude V_m was applied to copper electrodes. We note that in case of a frequency-dependence of the ME coupling, values obtained may be different from values obtained with other techniques operating at lower frequency. In particular, effects of current leakage may be expected to be less severe at high frequencies of the order of 100 kHz.

Fig. 4.5 shows the FMR signals measured at room temperature by using magnetic (black) and electric (red) field modulations, with a dc magnetic field applied at angle θ=75⁰. This angle was chosen because at θ=90⁰ FMR signal was very broad as shown in 4.4.2 (b) and it becomes very difficult to extract information about ME coupling at this angle. One can see that a clear electric field modulation FMR signal is detected in $Ba_{0.6}Sr_{1.4}Zn_2Fe_{12}O_{22}$. Observation of the electrically modulated FMR signal unambiguously proves the existence of ME coupling in $Ba_{0.6}Sr_{1.4}Zn_2Fe_{12}O_{22}$ since no signal can be observed in materials that do not possess ME coupling [Maisuradze, 2012].

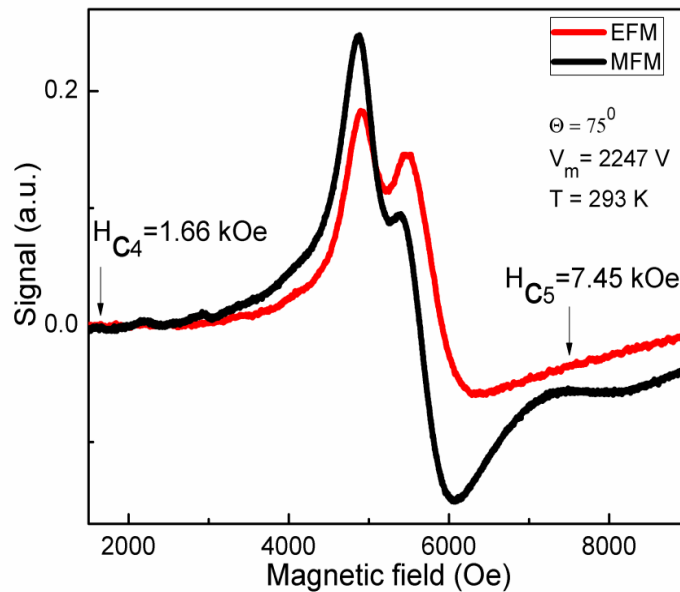Fig. 4.5. FMR spectra at θ=75⁰ for the $Ba_{0.6}Sr_{1.4}Zn_2Fe_{12}O_{22}$ hexaferrite single crystal detected at room temperature using the MFM technique (black line) and EFM technique (red line) with applied voltage $V_m = 2247$ V.

It is instructive to compare the range of magnetic fields in Fig. 4.5 with characteristic magnetic fields $H_{c1}-H_f$ obtained from magnetization measurements. For comparison, taking into account the θ angle, the characteristic fields of table I should be increased by a 3.5% $(1/\sin\theta)$.

Moreover, the ME coupling strength can be determined quantitatively from the ratio of the EFM and MFM-FMR signal intensities [Maisuradze, 2012; Popova, 2015]:

$$\gamma = (I^{EFM}/I^{MFM})(\mu_0 H_m/V/d)) \qquad (4.4.1)$$

where, $I^{EFM)}$ and I^{MFM} are the signal intensities detected by electric and magnetic modulations, $\mu_0 H_m$ is the modulation magnetic field, V is applied voltage and d is a distance between electrodes. Using Eq. 4.4.1 the value of ME coupling strength γ=2.7×10^{-5} Oe/V/mm was obtained at room temperature and θ=75^0, which corresponds to γ=2.7 ps/m. This is close to the value around 2 ps/m reported for prototypical ME compound Cr_2O_3 at room temperature [Borisov, 2007].

4.6 Neutron measurement results

As we mentioned in the section 2.4.3, the crystal structure of Y-type hexaferrite consists of alternately stacked spinal (S) and tetragonal (T) blocks crystallizing in R$\bar{3}$m space group [4]. This centrosymmetric space group does not allow any polarization, but scenario changes when magnetic field is applied perpendicular to c-axis. Magnetic field driven ferroelectric polarization was observed in the intermediate-III metamagnetic phase where a "2-fan" planner structure shown in Fig. 4.6.1 (a) was earlier reported [Momozava, 1985; Momozava, 1993]. However, later it was shown that the magnetic field driven ferroelectricity cannot be explained in the proposed fanlike structure [Momozawa, 1993]. Instead, it can exist in a transverse conical spin structure shown in Fig. 4.6.1 (b). Such magnetic structure has chirality which is consistent with the inverse Dzyaloshinskii-Moriya mechanism of ferroelectricity [Kimura, 2012].
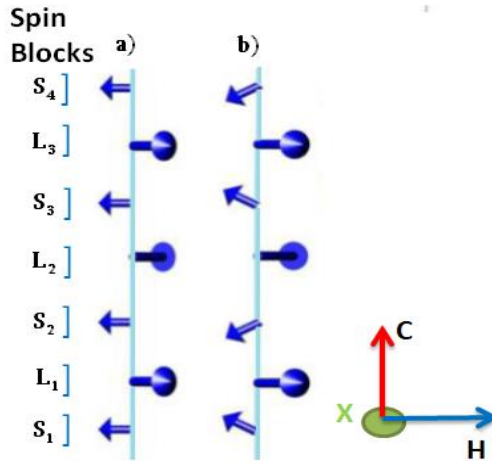
Fig. 4.6.1: a) schematic of the proposed "2-fan" magnetic structures in intermediate-II and intermediate-III phases and b) transverse conical spin structure in the ferroelectric phase for Y-type $Ba_{2-x}Sr_xZn_2Fe_{12}O_{22}$ hexaferrite.

In section 4.5, we presented ME effect at room temperature in single-crystal Y-type $Ba_{0.6}Sr_{1.4}Zn_2Fe_{12}O_{22}$ hexaferrite [Khazaradze, 2020]. This result indicates that the intermediate-II phase, similar to intermediate-III, is ferroelectric in this compound. If this is the case, intermediate-II phase should also have a transverse conical spin structure with corresponding chirality. Neutron diffraction with polarization analysis is a powerful tool for investigating chirality of magnetic structures in multiferroic oxides. Therefore, we performed the polarized neutron diffraction experiments to study magnetic structure in the intermediate-II and intermediate-III phases of magnetoelectric Y-type $Ba_{0.6}Sr_{1.4}Zn_2Fe_{12}O_{22}$ hexaferrite single-crystal. For neutron scattering experiments we used crystal with dimensions 3x1.5x0.3 mm.

The measurements were performed in the temperature range 5-100 K at different horizontal magnetic fields (H<2 T). We used full polarization analysis to separate the possible position of magnetic and structural peaks. Half polarized experiment was used to get access to the magnetic chirality. For both methods we needed the polarization in the scattering plane, therefore horizontal magnetic field was used. For the transverse conical spin structure,

in case of the vertical magnetic field the modulation of the magnetic moments in the scattering plane is restricted, which implies no chiral scattering.

The scattering cross section of the polarized neutrons is sensitive to spin chirality [Plakhty, 2000]. The scattering cross-section for polarized neutrons is given by Blume-Maleyev equation: [Blum, 1963; Maleyev, 1962]:

$$\sigma_Q = |N_Q|^2 + |M_Q^\perp|^2 + P(N_{-Q}M_Q^\perp + M_{-Q}^\perp N_Q) + iP(M_{-Q}^\perp \times M_{+Q}^\perp) \tag{4.6.1}$$

here, σ_Q is a scattering cross-section for polarized neutrons, **Q** is a scattering vector, N_Q and M_Q are nuclear and magnetic scattering amplitudes for a given **Q** and **P** polarization of a neutron beam, respectively.

In Eq. 4.6.1 only the last two terms depend on polarization of the incoming neutrons, and describe nuclear-magnetic interference scattering and chiraity. In our case, according to soft X-ray diffraction experiment there is no nuclear scattering present at (1, 0, 0.5) reflection. Therefore, in Eq. 4.6.1 we need only last chiral therm. We used polarized incident neutron beam without polarization analysis of the scattered beam (so-called half polarized experiment). By measuring the difference, $\Delta I(\omega, Q) = I^\uparrow(\omega, Q) - I^\downarrow(\omega, Q)$, for incident neutron polarizations parallel $I^\uparrow(\omega, Q)$ and antiparallel $I^\downarrow(\omega, Q)$ to the scattering vector **Q**, chiral magnetism was determined.

Fig. 4.6.2 shows full polarized analysis neutron scattering spectra of $Ba_{0.6}Sr_{1.4}Zn_2Fe_{12}O_{22}$ hexaferrite single-crystal for spin-flip and non-spin-flip intensities at 5 K. These measurements were performed for some selected reflections in a horizontal magnetic field configuration $H = 0.5$ T. For further measurements we selected (1, 0, 0.5) reflection where one of the most clear difference was observed between spin-flip and non-spin-flip intensities (see Fig. 4.6.2 d). For this reflection we explored chiral magnetism by performing half polarized experiments at different temperatures and magnetic fields.
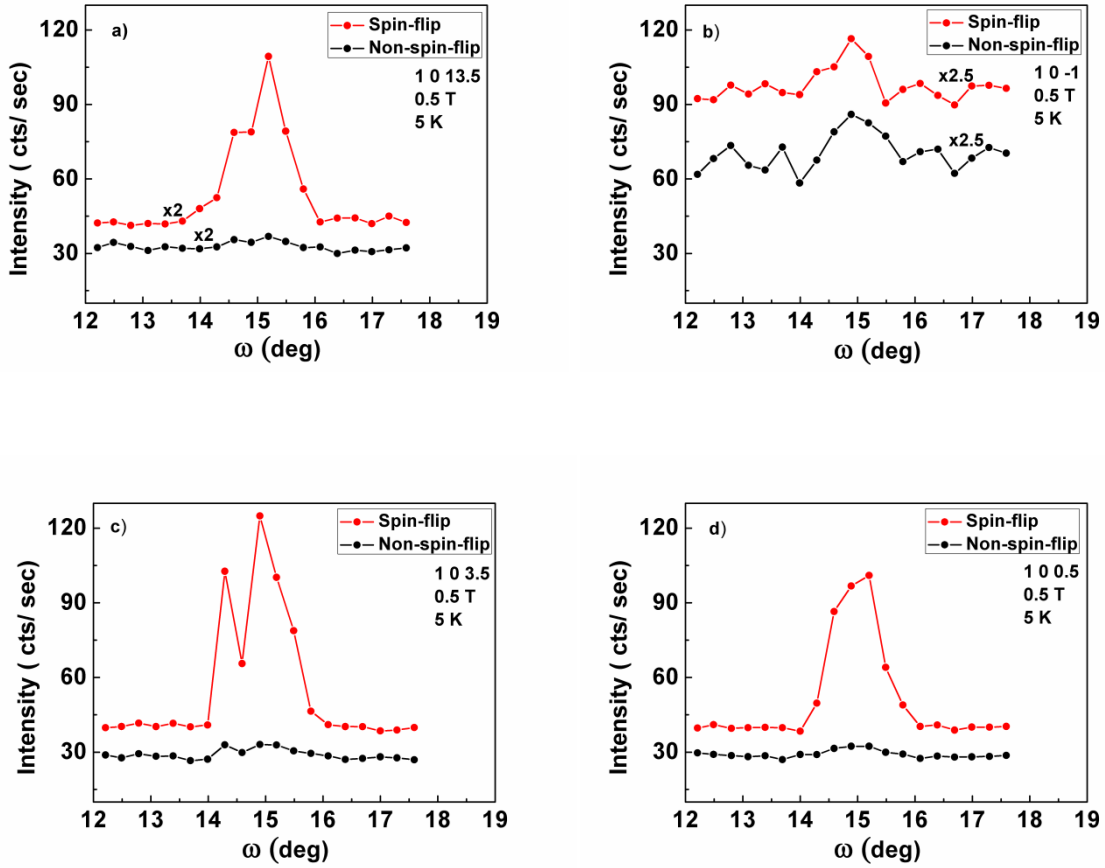
Fig. 4.6.2. Examples of full polarized analysis neutron scattering spectra for some selected reflections of $Ba_{0.6}Sr_{1.4}Zn_2Fe_{12}O_{22}$ hexaferrite single-crystal for spin-flip and non-spin-flip intensities at $T = 5$ K in horizontal field ($H = 0.5$ T) configuration.

Fig. 4.6.3 a shows ω-scans across the (1, 0, 0.5) reflection at T=100 K in $H = 0.6$ T horizontal magnetic field ($H \perp c$). One can see that the intensity is higher with neutron spin parallel ($I^{\uparrow}$) to the scattering vector Q compared to neutron spin antiparallel ($I^{\downarrow}$). The difference ($I^{\uparrow} - I^{\downarrow}$) is plotted in Fig. 4.6.3 b. Such behaviour is typical for the spiral magnets [Yamasaki, 2007]. Observed intensity difference provides evidence for the presence of chiral magnetism in intermediate-II phase. Therefore, one can conclude that the intermediate-II phase in Y-type $Ba_{0.6}Sr_{1.4}Zn_2Fe_{12}O_{22}$ hexaferrite can be ferroelectric in addition to the intermediate-III phase. This deviates from the conclusion derived by Kimura *et al.* based on macroscopic measurements [Kimura, 2005]. However, it is in agreement with our recent results obtained by ferromagnetic resonance [Khazaradze, 2020] and soft X-ray chiral scattering techniques.
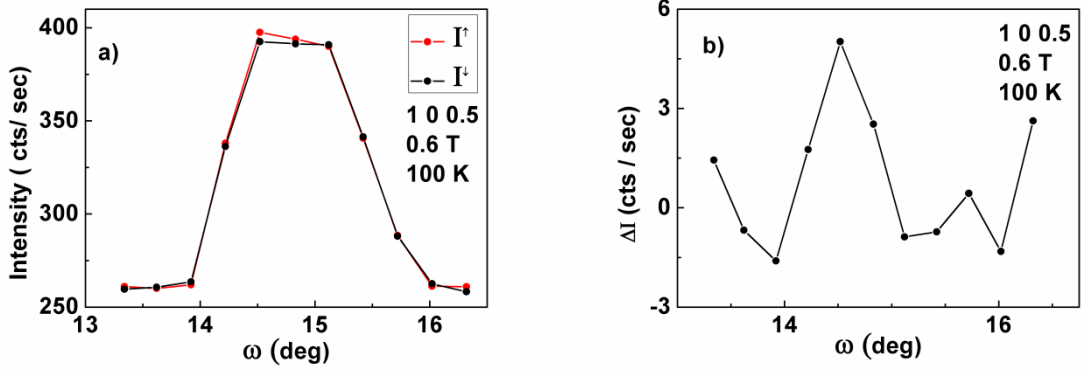
Fig. 4.6.3. a) ω-scans across the (1, 0, 0.5) reflection at T=100 K in H = 0.6 T horizontal magnetic field (**H**⊥ **c**) for positive ($I^\uparrow$) and negative polarized ($I^\downarrow$) neutrons. b) Difference between intensities $\Delta I = \left(I^\uparrow\right) - \left(I^\downarrow\right)$ of positive and negative polarized neutrons.

We also performed similar neutron diffraction measurements at T= 5 K and in horizontal magnetic fields H =0.3-1.3 T. In this field and temperature range Y-type $Ba_{0.6}Sr_{1.4}Zn_2Fe_{12}O_{22}$ hexaferrite is in intermediate-III phase [Kimura, 2012]. This phase is known to be ferroelectric. Indeed, we observed that in the intermediate-III phase, intensity of positive polarized neutrons ($I^\uparrow$) is higher than negative polarized neutrons ($I^\downarrow$), see Fig. 4.6.4. This confirms transverse conical spin structure also in intermediate-III phase. Therefore, we can conclude that the magnetic structure in both intermediate-II and intermediate-III phases allows the existence of magnetic field-induced ferroelectricity.
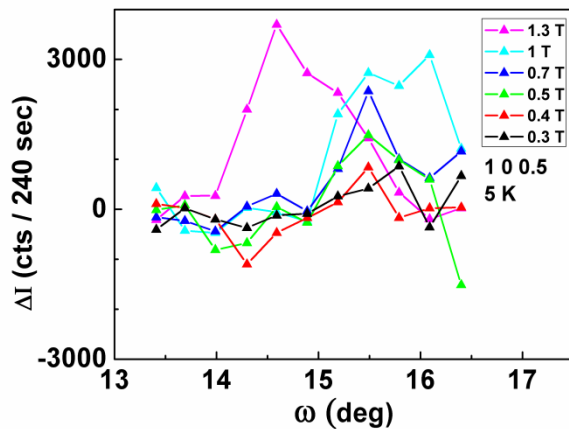

Fig. 4.6.4. Difference ($\Delta I = \left(I^\uparrow\right) - \left(I^\downarrow\right)$) in the intensities of positive ($I^\uparrow$) and negative polarized ($I^\downarrow$) neutrons at (1 0 0.5) reflection in 0.3-1.3 T horizontal magnetic fields (**H**⊥ **c**) at T= 5 K temperature (intermediate-III phase).

5 Summary and Conclusions

We have successfully grown single crystals of Y-type hexaferrite $Ba_{2-x}Sr_xZn_2Fe_{12}O_{22}$ (x=1.4) by flux growth method. Most of the crystals were plate like and the biggest one was found to have dimensions of $10 \times 8 \times 2$ mm^3. Single crystals were characterized by single-crystal X-ray diffraction measurements. The lattice parameters were found to be $a=b=5.85$ Å and $c=43.42$Å in ($R\bar{3}m$) space group with hexagonal setting. By performing structure refinement based on single crystal X-ray diffraction data, chemical composition of the crystal and partial occupancies of the Zn and Fe sites were determined. The Sr content (x) determined in a single crystal is slightly different from that of the starting reactant mixture. All transition metal-oxygen bond lengths were calculated from the structure refinement. It was found that the Zn(1)-O(1) bond length is shortest in the range of 1.9 Å, while Fe(3)-O(3) has the longest bond length (≈ 2.25 Å) compared to other average bond lengths of ≈ 2 Å.

It was found that Y-type hexaferrite $Ba_{1.6}Sr_{0.4}Zn_2Fe_{12}O_{22}$ orders magnetically below about 400 K and magnetization exhibits a sharp peak at 331 K, which corresponds to magnetic transition from collinear ferrimagnetic phase to a proper screw spin phase. Magnetic hysteresis measurements showed stepwise behavior of initial magnetization curve due to sequential metamagnetic transitions from helimagnetic to collinear ferrimagnetic phase with increasing magnetic field. From magnetic hysteresis measurements also a small coercivity field (H_c =20 Oe at 300 K and H_c=15 Oe at 50 K) was determined, which indicates soft magnetic behavior of this compound.

Microscopic magnetic properties of $Ba_{0.6}Sr_{1.4}Zn_2Fe_{12}O_{22}$ hexaferrite were investigated by FMR spectroscopy. Magnetic anisotropy field was determined from angular dependence of FMR resonance field. Using novel and highly sensitive method of electrically modulated FMR it was shown that this Y-type hexaferrite has significant magnetoelectric coupling at room temperature. The magnitude of this coupling was determined quantitatively. Obtained results show that Y-type hexaferrite $Ba_{0.6}Sr_{1.4}Zn_2Fe_{12}O_{22}$ has a rare combination of magnetoelectric coupling and large magnetization at room temperature, which is important for applications in magnetoelectric devices. There is a potential to further increase

magnetoelectric coupling of these materials at room temperature by properly adjusting their chemical composition.

We studied chiral magnetic structure in single crystal of Y-type $Ba_{0.6}Sr_{1.4}Zn_2Fe_{12}O_{22}$ hexaferrite by using neutron diffraction with polarization analysis. A wide range of the temperature and magnetic field was explored, which includes intermediate-II and intermediate-III phases of $Ba_{0.6}Sr_{1.4}Zn_2Fe_{12}O_{22}$. Chiral magnetism was detected in both of these phases. This shows that in contrast to previous assumptions, intermediate-II phase also has transverse conical spin structure similar to the intermediate-III phase. This magnetic structure has chirality which is consistent with the inverse Dzyaloshinskii-Moriya mechanism of ferroelectricity and therefore magnetic field induced ferroelectricity is possible. Obtained results justify the presence of magnetoelectric coupling in intermediate-II phase of $Ba_{0.6}Sr_{1.4}Zn_2Fe_{12}O_{22}$ hexaferrite, which was discovered in our studies by using electrically modulated ferromagnetic resonance.

References

Agilent Technologies. (2014). SuperNova X-ray Diffractometer System: User Manual. Oxfordshire, UK: Author.

Aken, B. B. V., Palstra, T. T., Filippetti, A., & Spaldin, N. A. (2004). The origin of ferroelectricity in magnetoelectric $YMnO_3$. Nature Materials, 3(3), 164–170. doi: 10.1038/nmat1080

Astrov, D. (1960). The Magnetoelectric Effect in Antiferromagnetics. Journal of Experimental and Theoretical Physics, 11(3), 708-709

Bartkowska, J. (2015). The magnetoelectric coupling effect in multiferroic composites based on PZT–ferrite. Journal of Magnetism and Magnetic Materials, 374, 703–706. doi: 10.1016/j.jmmm.2014.09.022

Bragg's law. (2020). Retrieved 10 June 2020, from http://hyperphysics.phy-astr.gsu.edu/hbase/quantum/bragg.html

Brijesh, S. (2016). Applications of Hexagonal Ferrites in Ultra High Frequency Range Especially in GHz Range. International Journal of Computer Science And Technology, 7(1), 82–83.

Blume, M. (1963). Polarization Effects in the Magnetic Elastic Scattering of Slow Neutrons. Physical Review, 130(5), 1670–1676. doi: 10.1103/physrev.130.1670

Borisov, P., Hochstrat, A., Shvartsman, V. V., & Kleemann, W. (2007). Superconducting quantum interference device setup for magnetoelectric measurements. Review of Scientific Instruments, 78(10), 106105-106105-3. doi: 10.1063/1.2793500

Cheong, S.-W., & Mostovoy, M. (2007). Multiferroics: a magnetic twist for ferroelectricity. Nature Materials, 6(1), 13–20. doi: 10.1038/nmat1804

Choi, Y. J., Yi, H. T., Lee, S., Huang, Q., Kiryukhin, V., & Cheong, S.-W. (2008). Ferroelectricity in an Ising Chain Magnet. Physical Review Letters, 100(4), 047601-047601-4. doi: 10.1103/physrevlett.100.047601

Chun, S. H., Chai, Y. S., Oh, Y. S., Jaiswal-Nagar, D., Haam, S. Y., Kim, I., Kim, K. H. (2010). Publisher's Note: Realization of Giant Magnetoelectricity in Helimagnets [Phys. Rev. Lett.104, 037204 (2010)]. Physical Review Letters, 104(4), 037204–037208. doi: 10.1103/physrevlett.104.049901

Collomb, A., Muller, J., Guitel, J., & Desvignes, J. (1989). Crystal structure and zinc location in the $BaZnFe_6O_{11}$ Y-type hexagonal ferrite. Journal of Magnetism and Magnetic Materials, 78(1), 77–84. doi: 10.1016/0304-8853(89)90089-9

Collomb, A., Samaras, D., Hadjivasiliou, S., Achilleos, C., Tsoukalas, J., Pannetier, J., & Rodriguez, J. (1988). Easy-axis reorientation in the BaCo2-W hexagonal ferrite. Journal of Applied Physics, 64(10), 5983–5985. doi: 10.1063/1.342170

Cullity, B. D., & Graham, C. D. (2009). Introduction to magnetic materials. Hoboken, NJ: IEEE/Wiley.

Curie, P. (1894). Sur la symétrie dans les phénomènes physiques, symétrie d'un champ électrique et d'un champ magnétique. Journal de Physique Théorique et Appliquée, 3(1), 393 – 415. DOI: 10.1051/jphystap:018940030039300

Debye, P. (1926). Bemerkung zu einigen neuen Versuchen über einen magneto-elektrischen Richteffekt. Zeitschrift Für Physik, 36(4), 300–301. doi: 10.1007/bf01557844

Dorsey, P., Sun, K., Vittoria, C., Wittenauer, M. A., Friedlander, F. J., & Schindler, A. (1990). Ferrimagnetic resonance linewidth in single-crystal Mn-doped $Ba_2Zn_2Fe_{12}O_{22}$. Journal of Applied Physics, 67(9), 5524–5526. doi: 10.1063/1.345872

Džunuzović, A., Ilić, N., Petrović, M. V., Bobić, J., Stojadinović, B., Dohčević-Mitrović, Z., & Stojanović, B. (2015). Structure and properties of Ni–Zn ferrite obtained by auto-combustion method. Journal of Magnetism and Magnetic Materials, 374, 245–251. doi: 10.1016/j.jmmm.2014.08.047

Dzyaloshinskii I. E. (1960). On the magneto-electrical effect in antiferromagnets. Journal of Experimental and Theoretical Physics, 37(881), 628–629

Eaton, G. R., & Weber, R. T. (2014). Quantitative Epr. Wien: Springer.

Eckert, M. (2012). Max von Laue and the discovery of X-ray diffraction in 1912. Annalen Der Physik, 524(5), A83-A85. doi: 10.1002/andp.201200724

Eerenstein, W., Mathur, N. D., & Scott, J. F. (2006). Multiferroic and Magnetoelectric Materials. ChemInform, 37(44), 759-765. doi: 10.1002/chin.200644216

Elwell, D., & Scheel, H. J. (1975). Crystal growth from high-temperature solutions. London: Academic Press.

Fiebig, M. (2005). Revival of the magnetoelectric effect. Journal of Physics D: Applied Physics, 38(8), R123–R152 . doi: 10.1088/0022-3727/38/8/r01

Gorter, E. (1957). Saturation magnetization of some ferrimagnetic oxides with hexagonal crystal structures. Proceedings of the IEE - Part B: Radio and Electronic Engineering, 104(5S), 255–260. doi: 10.1049/pi-b-1.1957.0042

Kamba, S., & Goian, V. (2010). Dielectric, magnetic, and lattice dynamics properties of Y-type hexaferrite $Ba_{0.5}Sr_{1.5}Zn_2Fe_{12}O_{22}$: Comparison of ceramics and single crystals. Journal of Applied Physics, 107(10), 104109. doi: 10.1063/1.3402379

Kasap, S. O. (1997). Principles of Electrical Engineering Materials and Devices. New York: McGraw Hill.

Katsura, H., Nagaosa, N., & Balatsky, A. V. (2005). Spin Current and Magnetoelectric Effect in Noncollinear Magnets. Physical Review Letters, 95(5), 057205-1-1057205–5. doi: 10.1103/physrevlett.95.057205

Khazaradze, G., Thakuria, P., Daraselia, D., Japaridze, D., Angst, M., & Shengelaya, A. (2020). Magnetic and magnetoelectric properties of Y-type $Ba_{0.6}Sr_{1.4}Zn_2Fe_{12}O_{22}$ hexaferrite single crystal. Journal of Magnetism and Magnetic Materials, 498, 166177-166179. doi: 10.1016/j.jmmm.2019.166177

Khomskii, D. (2009). Classifying multiferroics: Mechanisms and effects. Physics, 2(20). doi: 10.1103/physics.2.20

Kimura, T. (2012). Magnetoelectric Hexaferrites. Annual Review of Condensed Matter Physics, 3(1), 93–110. doi: 10.1146/annurev-conmatphys-020911-125101

Kimura, T., Lawes, G., & Ramirez, A. P. (2005). Electric Polarization Rotation in a Hexaferrite with Long-Wavelength Magnetic Structures. Physical Review Letters, 94(13), 137201-1-137201-4. doi: 10.1103/physrevlett.94.137201

Kimura, T., Sekio, Y., Nakamura, H., Siegrist, T., & Ramirez, A. P. (2008). Cupric oxide as an induced-multiferroic with high-TC. Nature Materials, 7(4), 291–294. doi: 10.1038/nmat2125

Kitagawa, Y., Hiraoka, Y., Honda, T., Ishikura, T., Nakamura, H., & Kimura, T. (2010). Low-field magnetoelectric effect at room temperature. Nature Materials, 9(10), 797–802. doi: 10.1038/nmat2826

Kittel C. (1951). Ferromagnetic resonance. Le Journal De Physique Et Radium, 12 (3), 291-302.

Li, G., Bentoumi, G., Tun, Z., Li, L., & Sur, B. (2016). Thermal Neutron Scattering Cross-Section Measurements of Heavy Water. CNL Nuclear Review, 6(1), 47–53. doi: 10.12943/cnr.2016.00008

Maisuradze, A., Shengelaya, A., Berger, H., Djokić, D. M., & Keller, H. (2012). Magnetoelectric Coupling in Single Crystal Cu_2OSeO_3 Studied by a Novel Electron Spin Resonance Technique. Physical Review Letters, 108(24), 247211-247214. doi: 10.1103/physrevlett.108.247211

Maleyev, S. V. (1962). Polarization Results from Scattering of Neutrons byFerromagnetic Substances. Journal of Experimental and Theoretical Physics, 13(4), 860–862.

Momozawa, N. (1986). Magnetic structure change in $Ba_2Mn_2Fe_{12}O_{22}$. Journal of the Physical Society of Japan, 55(44), 1350–1358.

Momozawa, N., & Yamaguchi, Y. (1993). Field-Induced Commensurate Intermediate Phases in Helimagnet $(Ba_{1-x}Sr_x)_2Zn_2Fe_{12}O_{22}$(x=0.748). Journal of the Physical Society of Japan, 62(4), 1292–1304. doi: 10.1143/jpsj.62.1292

Momozawa, N., Yamaguchi, Y., Takei, H., & Mita, M. (1985). Modification of Helix in $(Ba_{1-x}Sr_x)_2Zn_2Fe_{12}O_{22}$ Due to Applied Magnetic Field. Journal of the Physical Society of Japan, 54(10), 3895-3903. doi:10.1143/jpsj.54.3895

Muller, J., Collomb, A., Fournier, T., Harrowfield, I., & Samaras, D. (1991). Composition and structure of some $[Ba_{1-p}Sr_p]ZnFe_6O_{11}$ Y-type hexagonal ferrites. Journal of Magnetism and Magnetic Materials, 102(3), 305–313. doi: 10.1016/0304-8853(91)90143-x

Muniraju, N. K. C. (2012). Crystal and spin structure and their relation to physical properties in some geometrical and spin spiral multiferroics. Jülich: Forschungszentrum Zentralbibliothek.

Okumura, K., Ishikura, T., Soda, M., Asaka, T., Nakamura, H., Wakabayashi, Y., & Kimura, T. (2011). Magnetism and magnetoelectricity of a U-type hexaferrite $Sr_4Co_2Fe_{36}O_{60}$. Applied Physics Letters, 98(21), 212504-1-212504-3. doi: 10.1063/1.3593371

Paoluzi, A., Licci, F., Moze, O., Turilli, G., Deriu, A., Albanese, G., & Calabrese, E. (1988). Magnetic, Mössbauer, and neutron diffraction investigations of W-type hexaferrite $BaZn_{2-x}Co_xFe_{16}O_{27}$single crystals. Journal of Applied Physics, 63(10), 5074–5080. doi: 10.1063/1.340405

Plakhty, V. P., Kulda, J., Visser, D., Moskvin, E. V., & Wosnitza, J. (2000). Chiral Critical Exponents of the Triangular-Lattice AntiferromagnetCsMnBr3as Determined by Polarized Neutron Scattering. Physical Review Letters, 85(18), 3942–3945. doi: 10.1103/physrevlett.85.3942

Petříček, V., Dušek, M., & Palatinus, L. (2014). Crystallographic Computing System JANA2006: General features. Zeitschrift Für Kristallographie - Crystalline Materials, 229(5), 345–352. doi: 10.1515/zkri-2014-1737

Pollert, E. (1985). Crystal chemistry of magnetic oxides part 2: Hexagonal ferrites. Progress in Crystal Growth and Characterization, 11(3), 155–205. doi: 10.1016/0146-3535(85)90033-4

Popova, E., Shengelaya, A., Daraselia, D., Japaridze, D., Cherifi-Hertel, S., Bocher, L., Keller, N. (2017). Bismuth iron garnet $Bi_3Fe_5O_{12}$: A room temperature magnetoelectric material. 2017 IEEE International Magnetics Conference (INTERMAG), (110), 142404. doi: 10.1109/intmag.2017.8008021

Pullar, R. C. (2012). Hexagonal ferrites: A review of the synthesis, properties and applications of hexaferrite ceramics. Progress in Materials Science, 57(7), 1191–1334. doi: 10.1016/j.pmatsci.2012.04.001

Purushotham, Y., & Reddy, P. V. (1996). Charge Transport And Conduction Mechanism Of Some Substituted Strontium W-Type Hexagonal Ferrites. International Journal of Modern Physics B, 10(03), 319–336. doi: 10.1142/s0217979296000131

Quantum Design. (2008). Physical Property Measurement System: PPMS VSM Option User's Manual. San Diego, USA: Author.

Röntgen, W. C. (1888). Ueber die durch Bewegung eines im homogenen electrischen Felde befindlichen Dielectricums hervorgerufene electrodynamische Kraft. Annalen Der Physik Und Chemie, 271(10), 264–270. doi: 10.1002/andp.18882711003

Ryan, P. J., Kim, J.-W., Birol, T., Thompson, P., Lee, J.-H., Ke, X., … Schlom, D. G. (2013). Reversible control of magnetic interactions by electric field in a single-phase material. Nature Communications, 4(1), 1334–1341. doi: 10.1038/ncomms2329

Sadiq, I., Ali, I., Rebrov, E., Naseem, S., Ashiq, M. N., & Rana, M. (2014). Nanosized Ce–Zn substituted microwave absorber material for X-band applications. Journal of Magnetism and Magnetic Materials, 370, 25–31. doi: 10.1016/j.jmmm.2014.06.045

Schmid, H. (1994). Multi-ferroic magnetoelectrics. Ferroelectrics, 162(1), 317–338. doi: 10.1080/00150199408245120

Schmid, I. (2006). The Role of Uncompensated Spins in Exchange Biased Systems. Doctoral Dissertation, Universität Basel, Basel, Switzerland. Retrieved from https:/ / www.dora. lib4ri.ch/ empa/ islandora/ object/ empa:2033

Smit, J., & Wijn, H. P. J. (1959). Ferrites: physical properties of ferrimagnetic oxides in relation to their technical applications. New York: Wiley.

Shen, S.-P., Liu, X.-Z., Chai, Y.-S., Studer, A., Rule, K., Zhai, K., Sun, Y. (2017). Hidden spin-order-induced room-temperature ferroelectricity in a peculiar conical magnetic structure. Physical Review B, 95(9), 094405 doi: 10.1103/physrevb.95.094405

Song, Y. Q., Fang, Y., Wang, L. Y., Zhou, W. P., Cao, Q. Q., Wang, D. H., & Du, Y. W. (2014). Spin reorientation transition and near room-temperature multiferroic properties in a W-type hexaferrite $SrZn_{1.15}Co_{0.85}Fe_{16}O_{27}$. Journal of Applied Physics, 115(9), 093905-1–093905-4. doi: 10.1063/1.4867370

Tokunaga, Y., Taguchi, Y., Arima, T.-H., & Tokura, Y. (2012). Electric-field-induced generation and reversal of ferromagnetic moment in ferrites. Nature Physics, 8(11), 838–844. doi: 10.1038/nphys2405

Tokura, Y., Seki, S., & Nagaosa, N. (2014). Multiferroics of spin origin. Reports on Progress in Physics, 77(7), 076501–076546. doi: 10.1088/0034-4885/77/7/076501

Toperverg, B. P., & Zabel, H. (2015). Neutron Scattering in Nanomagnetism. Experimental Methods in the Physical Sciences Neutron Scattering - Magnetic and Quantum Phenomena, 48(1), 339–434. doi: 10.1016/b978-0-12-802049-4.00006-3

Trevino S. F. (1992). The Triple Axis and SPINS Spectrometers. Journal of Research of the National Institute of Standards and Technology, 98 (1), 59-69 doi: 10.6028/jres.098.005

Utsumi, S., Yoshiba, D., & Momozawa, N. (2007). Superexchange Interactions of $(Ba_{1-x}Sr_x)_2Zn_2Fe_{12}O_{22}$ System Studied by Neutron Diffraction. Journal of the Physical Society of Japan, 76(3), 034704. doi: 10.1143/jpsj.76.034704

Vittoria, C. (2015). Ferrimagnetic resonance and magnetoelastic excitations in magnetoelectric hexaferrites. Physical Review B, 92(6), 064407. doi: 10.1103/physrevb.92.064407

Wang, J. (2003). Epitaxial $BiFeO_3$ Multiferroic Thin Film Heterostructures. Science, 299(5613), 1719–1722. doi: 10.1126/science.1080615

Wu, S. M., Cybart, S. A., Yu, P., Rossell, M. D., Zhang, J. X., Ramesh, R., & Dynes, R. C. (2010). Reversible electric control of exchange bias in a multiferroic field-effect device. Nature Materials, 9(9), 756–761. doi: 10.1038/nmat2803

Xu, W., Wang, Z., Yang, J., Bai, W., Zhang, Y., & Tang, X. (2014). Magnetic and Dielectric Properties in Multiferroic Y-type Hexaferrite. Molecular Crystals and Liquid Crystals, 603(1), 235–239. doi: 10.1080/15421406.2014.967614

Yamani, Z., Tun, Z., & Ryan, D. H. (2010). Neutron scattering study of the classical antiferromagnet MnF2: a perfect hands-on neutron scattering teaching courseSpecial issue on Neutron Scattering in Canada. Canadian Journal of Physics, 88(10), 771–797. doi: 10.1139/p10-081

Yamasaki, Y., Sagayama, H., Goto, T., Matsuura, M., Hirota, K., Arima, T., & Tokura, Y. (2007). Electric Control of Spin Helicity in a Magnetic Ferroelectric. Physical Review Letters, 98(14), 147204-1–147204-4. doi: 10.1103/physrevlett.98.147204

Zavoisky, E. (1945) Spin-magnetic resonance in paramagnetics. Fizicheskiĭ Zhurnal, 9, 211–245.

Zhang, M., Dai, J., Yin, L., Kong, X., Liu, Q., Zi, Z., & Sun, Y. (2016). Mg doping effect on the magnetic properties of Y-type hexaferrite $Ba_{0.5}Sr_{1.5}Zn_{2-x}Mg_xFe_{12}O_{22}$. Journal of Alloys and Compounds, 689, 75–80. doi: 10.1016/j.jallcom.2016.07.318

List of published papers:

1. **Khazaradze, G**., Thakuria, P., Daraselia, D., Japaridze, D., Angst, M., & Shengelaya, A. (2020). Magnetic and magnetoelectric properties of Y-type $Ba_{0.6}Sr_{1.4}Zn_2Fe_{12}O_{22}$ hexaferrite single crystal. Journal of Magnetism and Magnetic Materials, 498, 166177-166179. doi: 10.1016/j.jmmm.2019.166177

2. **Khazaradze, G**., Daraselia, D., Japaridze, D., & Shengelaya, A. (2019). Magnetoelectric coupling in Y-type hexaferrite studied by a novel magnetic resonance technique. Magnetic Resonance in Solids, 21(3), 1-7. doi:10.26907/mrsej-19307

3. **Khazaradze, G**., & Shengelaya A. (2020). Chiral magnetic structure of Y-type $Ba_{0.6}Sr_{1.4}Zn_2Fe_{12}O_{22}$ hexaferrite in intermediate phase. Nano studies, 20 (Accepted for publication).